Fakultät für Maschinenwesen

Lehrstuhl für Aerodynamik und Strömungsmechanik

Modeling and simulation of particle dispersions with smoothed dissipative particle dynamics

Xin Bian

Master of Science

Vollständiger Abdruck der von der Fakultät für Maschinenwesen der Technischen Universität München zur Erlangung des akademischen Grades eines

Doktor-Ingenieurs

genehmigten Dissertation.

Vorsitzender: Univ.-Prof. Dr.-Ing. Nikolaus A. Adams

Prüfer der Dissertation:

1. TUM Jun. Fellow Dr. rer. nat. Marco Ellero

2. Univ-Prof. Phaedon-Stelios Koutsourelakis, Ph.D.

Die Dissertation wurde am 26.11.2013 bei der Technischen Universität München eingereicht und durch die Fakultät für Maschinenwesen am 02.10.2014 angenommen.

Acknowledgments

First of all, I am deeply indebted to Dr. Marco Ellero, who initiated this project in the Emmy-Noether program. He introduced and taught me various subjects including particle-based numerical schemes, dynamics of complex fluids and non-Newtonian rheology. All of them are fascinating and keep me obsessed all the time. In addition, I am very grateful to the continuous guidance of him, who has been advising this work thoroughly, inspiring me with new ideas, and encouraging me with great visions.

I am also very grateful to Prof. Dr. Nikolaus A. Adams for having been my co-advisor, who listened to my subtle problems and provided fruitful hints and suggestions at weekly group meetings. As the institute director, he also made much efforts to provide me many facilities. Without him this work would have been difficult to complete.

Great gratitude is given to Prof. Dr. Norman J. Wagner, who I met in annual European rheology conferences, 2010 in Gothenburg, Sweden and 2011 in Suzdal, Russia. After good acquaintance with him, I was invited to visit his laboratory at University of Delaware, U.S., in November and December of 2011. During this time, I had chance of approaching experimental apparatus for the first time and enhancing my knowledge about colloidal dispersion, especially the intriguing shear thickening phenomenon.

I want to acknowledge Prof. Pep Español as my examiner, who is a leader in multiscale modeling of complex fluids and an expert on soft matter physics. His comments and judgment are an honor of me and an enlightenment for my future research. I owe a great gratitude to Prof. Sonja Berensmeier, who spent her precious time as the chair organizing the examination committee and witnessing the justice of thesis evaluation.

I am also grateful to Mr. Sergey Litvinov, who as a senior Ph.D. student is always available for both scientific and technical help. There were so many times I got novel ideas during discussions with him. Discussions with other colleagues: Dr. Adolfo Vázquez-Quesada, Dr. Xiangyu Hu, Mr. Stefan Adami, Mr. Yilei Shi, Mr. Rui Qian, and Mr. Babak Gholami are also acknowledged.

I would like to thank specially Ms. Hui Chen for her interest and patience of listening to my scientific anecdotes, and also for her love support, especially when I had overlong working hours and came home late.

In the end, a very special acknowledgment is given to my father Guihong Bian and my mother Baozhen Zhao. They have been always supportive and giving me encouragement whenever I decided to go after my dreams. I am deeply indebted to them, as I have been seldom around. Nevertheless, they never reduced a little how they love me.

Abstract

This thesis is devoted to the modeling and simulation of particle dispersions with smoothed dissipative particle dynamics (SDPD). SDPD is a multiscale framework linking macroscopic smoothed particle hydrodynamics (SPH) method to mesoscopic dissipative particle dynamics (DPD) method. We apply SDPD to model rigid structures of arbitrary shape embedded in a fluid and enforce exactly the no-slip boundary condition on the liquid-solid interface. Demonstrated by numerous benchmark problems, the correct scaling of the SDPD thermal fluctuations with the fluid-particle size allows to describe the dynamics of solid particles on spatial scales ranging continuously from the non-Brownian regime, characterizing macro-continuum flow conditions, down towards the diffusion-dominated regime, typical of sub-micron-sized objects. The correct coupling between a colloidal particle and external walls is also validated.

Simulating many nearly contacting solid particles in suspension is a challenging task due to the diverging behavior of short-range lubrication forces, which pose a serious time-step limitation for explicit integration schemes. We propose a splitting integration scheme, which separates the contributions of different forces acting on the solid particles. In particular, intermediate- and long-range multi-body hydrodynamic forces, which are computed from SPH method, are taken into account using an explicit integration; for short-range lubrication forces, velocities of pairwise interacting solid particles are updated implicitly by sweeping over all the neighboring pairs iteratively, until convergence in the solution is obtained. By using the splitting integration, simulations can be run stably and efficiently up to very large solid particle concentrations. Moreover, the proposed scheme is not limited to the SPH method presented, but it can be easily applied to other simulation techniques employed for particulate suspensions.

With the proposed model accelerated by the splitting integration scheme, we study the rheology of dense suspension of non-Brownian repulsive particles. The suspension of two-dimensional discoidal particles is confined by walls orthogonal to the shear gradient direction. According to previous literature, we observe continuous/hydrodynamic shear thickening and we find the strength to be determined by distribution of hydrodynamic clusters while confinement plays a geometrical role and indirectly affects viscosity. Under strong confinement the percolating network of clusters develop into a jamming structure at high shear rate and as a result, the viscosity increases substantially. Extrapolating the viscosity to the limit of very weak confinement shows that confinement is important for non-negligible hydrodynamic shear thickening. The shear thickening of hydrodynamically interacting particles being continuous also implies that discontinuous shear thickening observed experimentally requires additional inter-particle stresses, such as those resulted from frictional contact.

Zusammenfassung

Diese Dissertation ist anhänlich zur Modellierung und Simulationen von der Partikel Dispersion mit “smoothed dissipative particle dynamics (SDPD)”. SDPD ist ein Rahmen mit mehreren Skalen und eine Verbindung von der makroskopische “smoothed particle hydrodynamics (SPH)” Methoden zur mittelskopische “dissipative particle dyanmics (DPD)” Methoden. Wir wenden SDPD an, um die rigide Struktur mit arbitärem Form eingebaut im Fluid zu modellieren und die Haftbedingung der Grenzfläche durchzuführen. Die wärme Bewegung in der SDPD hängt von Fluid Parikel Größe ab. Diese korrekte Skalierung ermöglicht die Dynamik von rigid Partikel richtig zu berscheiben. Dies wurde bereits durch vielen Benchmark-Tests bewiesen, die die Bereichen von der deterministisch Strömungen bei Kontinuitätsgleichung bis zur Brownsche Bewegung umfasst. Außerdem ist die Kopplung zwischen ein Kolloid und dem außen Walls bestätigt.

Aufgrund der außerordentliche hydrodynamischer Schmierung sind die Simulationen für vielen nahezu rigide Partikels im Dispergiermittel anspruchsvoll. Wir schlagen eine aufgeteilte Integration-Maßnahme vor. Die hydrodynamische Beeinflussung der lange Entfernung werde von SPH versorgt und explizit integriert. Die Beeinflussung der Kurzstrecke werde von paarweise Schmeierung Kraft modellieret und bedingungslos berechnet. Mit dieser neuem Method laufen die Simulationen bis zur große Konzentration des Festköper effizienter und dauerhafter.

Mit dem vorgeschlagene Model und vorverlegter aufgeteilte Integration untersuchen wir die Rheologie des Partikel Suspensionen unter Beschränkung des Walls. Dichte Suspensionen zeigen unter Schere Bewegungen nichtnewtonschere Eigenschaften, nämlich bei hohen Scherkräften eine höhere Viskosität: Scherverzähung. Bei Simulationen entdecken wir dass begleitenden hydrodynamische Clusters in der Scherverzähung immer existieren. Die Beschränkung des Walls spielt nur eine geometrische Rolle, das bedeutet: die Formulierung der Clusters werde durch die Reduzierung des Raumes vereinfacht. Dennoch hängt die Stärke der Scherverzähung von der Wahrscheinlichkeitsverteilung des Cluster einzig ab. Trotzdem ist die Beschränkung des Walls für ungeringfügig Scherverzähung erforderlich.

Contents

1 Introduction

According to the terminology and nomenclature of polymers defined by International Union of Pure and Applied Chemistry (IUPAC) [1, 2, 3], a *dispersion* is a system in which particles are suspended in a continuous phase of a different composition or state. Depending on the size of the dispersed particles in relation to the size of molecules of the continuous phase, a dispersion may be classified into three types:

- *coarse dispersion or suspension*: it is a heterogeneous mixture containing internal phase dispersed throughout the external phase. The size of the suspended particles is typically well above $1\mu m$ ($10^{-6}m$) and visible under an optical microscope. If a density difference between the two phases is present, the particles will eventually sediment or float under gravity or centrifugal force.

- *colloidal dispersion or colloid* [4]: the size of the particle is well below $10\mu m$ and down to a few nm ($10^{-9}m$). Such particles are normally invisible under an optical microscope, as the wavelength of the visible light is around $500nm$, comparable to the size of the target object. Nevertheless, their presence can be confirmed with the use of an ultramicroscope or an electron microscope. The term colloid is derived from the Greek word "$\kappa o\lambda\lambda\alpha$" for "glue". It has been coined by a Scottish chemist, Thomas Graham (1805 – 1869), who actually introduced the field of study and defined colloids as substances that cannot pass through a membrane, such as in dialysis [5, 6].

- *solution*: it is a homogeneous mixture on molecular level, such as for example, a saline water solution, where a solute ($NaCl$) is dissolved in another substance (H_2O) known as solvent. In this case, the dispersed particles are with the size ($< 1nm$) of the host medium molecules and not considered in a separated internal phase or solid state.

In this work, we are only interested in the first two types of dispersion, which are characterized by discrete particles dispersed in a continuous medium and are considered as *multiphase dispersion*, in distinction to the solution dispersion. The boundary between particle sizes in two types of dispersion is not always clear and often depends on the application. Both dispersed phase and continuous phase may be gas, liquid, or solid. Different combinations of the two substances result in 9 types of binary dispersions: gas in gas is gas mixture (e.g., air); liquid in gas is known as aerosol (e.g., fog and mist); solid in gas is known as solid aerosol (e.g., dust and smoke); gas in liquid is known as foam; liquid in liquid is known as emulsion; solid in liquid is known as suspension or sol; gas in solid is known as solid foam; liquid in solid is known as gel; solid in solid

is known as solid gel. We focus particularly on dispersions of solid particles dispersed in a liquid medium, where a dispersion with coarse (big) particles is named suspension while a dispersion with colloidal (small) particles is named sol. Sol is a particular type of colloid, therefore terms of sol and colloid may be used interchangeably. To alleviate the load of many nomenclatures in this thesis, we simply term them **colloidal** dispersion with small particles and **non-colloidal** dispersion with coarse particles respectively.

Non-colloidal and colloidal dispersions are ubiquitous. Blood, pharmaceuticals, cosmetics, mud, cement, paint, ink, slurries and cornstarch in water are some common examples [5, 6]. Understanding the dynamics, transport phenomena and rheology of such dispersions is of industrial interest, medical relevance and scientific importance [7, 8, 9, 10].

1.1 Physical model

To study multiphase dispersions — non-colloidal and colloidal dispersions — it is reasonable to assume that the fluid phase is continuous and can be described by the hydrodynamic equations.

1.1.1 Fluid phase: hydrodynamics

An isothermal, Newtonian fluid can be described by the continuity equation and momentum equations of *Navier-Stokes* [11, 12, 13, 14]. By considering the fluid in Lagrangian framework, they can be written as

$$\frac{d\rho}{dt} = -\rho \nabla \cdot \mathbf{v}, \tag{1.1}$$

and

$$\frac{d\mathbf{v}}{dt} = -\frac{\nabla p}{\rho} + \mathbf{F} + \mathbf{g}, \tag{1.2}$$

where ρ, $\mathbf{v}$, p, $\mathbf{F}$, and $\mathbf{g}$ are material density (kg/m^3), fluid velocity (m/s), pressure (Pa), viscous force, and body force per unit mass (N/kg or m/s^2) respectively. For certain applications, it is convenient to write and solve Eq. (1.2) in an Eulerian framework as

$$\frac{\partial \mathbf{v}}{\partial t} + \mathbf{v} \cdot \nabla \mathbf{v} = -\frac{\nabla p}{\rho} + \mathbf{F} + \mathbf{g}. \tag{1.3}$$

Note that the convective acceleration $\mathbf{v} \cdot \nabla \mathbf{v}$ of the flow is present, which is an additional source of numerical errors in an Eulerian discretization scheme. As we use a Lagrangian particle method to discretize the continuum equations in this work, we consider only the Lagrangian form of hydrodynamics presented in Eqs. (1.1) and (1.2).

Assuming a Newtonian constitutive equation for the fluid stress, the viscous force $\mathbf{F}$ simplifies to

$$\mathbf{F} = \nu \nabla^2 \mathbf{v}, \tag{1.4}$$

where ν is the kinematic viscosity (m^2/s) related to dynamic viscosity ($Pa{\cdot}s$ or $kg/(s{\cdot}m)$) by $\nu = \eta/\rho$.

In our particular case of particle dispersion, the fluid medium is a liquid, such as water, and is weakly compressible. The speed of sound c_s within the liquid is generally much higher than the maximal speed v of the bulk flow. Under these conditions, relative fluctuations in the fluid density $\Delta\rho/\rho$ are proportional to M_a^2, where $M_a = v/c_s$ is the Mach number, and are therefore extremely small [15]. It is customary to approximate the real fluid by an artificial fluid which is exactly incompressible [16, 17, 18], namely, $d\rho/dt = 0 \Rightarrow \nabla \cdot \mathbf{v} = 0$. We take a different approach following Monaghan 1994 [15], where the real fluid is approximated by an artificial one being more compressible than the real one. The sound speed c_s of the artificial fluid must be chosen still much larger than the speed v of bulk flow, in order to have very small density variations. Under these conditions, sound waves propagate very quickly, namely the typical time $\tau_{c_s} = a/c_s$ required by the sound wave to travel over a characteristic length 'a' (m) of the problem is very small. Nevertheless, c_s should not be unnecessarily large, which would limit severely the simulation time step Δt according to the *Courant-Friedrichs-Lewy condition* [19, 20].

To model a weakly compressible fluid, an equation of state taken from Batchelor 1967 [11, 15] relating pressure to density reads

$$p = p_0 \left[\left(\frac{\rho}{\rho_r} \right)^{\gamma} - 1 \right], \tag{1.5}$$

where p_0 (related to sound speed c_s), $\gamma = 7$ and ρ_r are parameters chosen based on a scale analysis [15, 21] such that pressure field reacts strongly to small deviations in mass density and quasi-incompressibility is enforced [11, 15, 22].

In fluid dynamics, a very important dimensionless number that indicates the relative importance of *inertial force* and *viscous force* for given flow conditions is the *Reynolds number* defined as

$$Re = \frac{inertial\ force}{viscous\ force}. \tag{1.6}$$

For many applications, such as shear flow, it is convenient to define an equivalent expression as follows

$$Re = \frac{\rho v a}{\eta} = \frac{v a}{\nu} = \frac{\dot{\gamma} a^2}{\nu}, \tag{1.7}$$

where v, a, and $\dot{\gamma}$ are the characteristic velocity, length scale, and shear rate ($1/s$) of the problem. The turbulent flow, for example, often starts with $Re > O(10^3)$ [23].

Within the majority of applications in particle dispersions, the inertia in the system is so small that $Re \ll 1$. In practice, $Re = 0$ is often used to simplify the problem, assuming vorticity propagation from viscous force infinitely fast. Under this assumption, the inertia in the momentum equations can be completely neglected and the Navier-Stokes equations are simplified to the *steady Stokes equations* [12, 14, 8],

$$0 = -\frac{\nabla p}{\rho} + \nu \nabla^2 \mathbf{v} + \mathbf{g}, \tag{1.8}$$

or the *unsteady Stokes equations* [12, 14, 8],

$$\frac{\partial \mathbf{v}}{\partial t} = -\frac{\nabla p}{\rho} + \nu \nabla^2 \mathbf{v} + \mathbf{g}. \tag{1.9}$$

It should be remarked, however, that if one is interested in the transient behavior of a particle in a viscous flow, where time scale of vorticity propagation can not be neglected, namely, $\tau_v = a^2/\nu > 0$, the full Navier-Stokes equations should be solved.

1.1.2 Solid phase: dispersed (or suspended) particles

In various applications of multiphase dispersions, the discrete particles may be very different. In some cases they are treated as soft deformable bodies, such as for example, red blood cells in blood flow through the circulatory systems, where appropriate internal stress-strain relation for the solid phase must be used [24]. For most industrial applications, the discrete particles are often hard and considered as rigid body. As there is no internal relative motion between each portion of the particle, it is relative easy to model such particles. Only *rigid particles* are considered in this thesis.

Moreover, we focus also on spherical particles, although the description of the model will not be restricted to spherical shapes. As it will be demonstrated, it is straightforward for particle methods described in this work to model arbitrary shape objects.

1.1.3 Fluid-solid interaction

A dispersion system is just a particular case of studies on fluid-structure interaction (FSI). In order to describe the interaction between the two phases, a boundary condition at the interface must be specified.

interface between fluid phase and solid phase

Usually sticky or *no-slip boundary condition* [25] is observed empirically, which means that a very thin layer of fluid adjacent to the solid phase has the same velocity as the solid. Because the solution is prescribed at the interface, the no-slip condition is an example of *Dirichlet boundary condition* in mathematics.

The no-slip condition allows to compute the flow solution in a domain defined by any arbitrary (moving) boundaries. In the specific case of a dispersed solid particle, its dynamics induced by the surrounding flow can be described by evaluating the total fluid force exerted on the solid structure (fluid-structure coupled problem). For example, the Stokes's drag of a sphere moving in a fluid is calculated by integrating the total friction on the sphere surface — resistance problem [12]; Similarly the terminal velocity of a sphere under a constant force (gravity) can also be calculated — mobility problem [12].

An external solid boundary, such as a plane wall, is just a simplified case of a solid particle with arbitrary shapes and predefined velocity (one way structure-fluid coupling).

A variety of boundary conditions at the interface, such as, slip or slip-sticky hybrid boundary condition [26] can be found in the literature and depend on the specific problem under study. More models concerning slip flow near boundaries are referred to

Karniadkais et al. 2005 [8]. We focus primarily on the no-slip boundary condition in this work.

Brownian versus non-Brownian particle

To differentiate between multiphase dispersions of non-colloidal and colloidal particles, a remarkable phenomenon named *Brownian motion* of the dispersed particle may be used.

This transport phenomenon was first discovered by a Scottish botanist, Robert Brown (1773 – 1858), who noted the random motion of pollen grains in water by looking through a microscope. Albert Einstein published a paper in 1905 [27], and independently von Smoluchowski in 1906 [28], that explained in precise detail how the Brownian motion of the dispersed particle results from the agitation of the fast-moving molecules of the fluid. The explanation served as a definitive confirmation that molecules actually exist. The corresponding calculation of the diffusion coefficient (D) via mean squared displacement (MSD) [27, 28, 29] provided a novel way to measure the size of a microscopic particle. It is explained as follows: if a series of positions $\mathbf{R}_C(t)$ of a spherical particle is recorded for each t, the MSD can be calculated as

$$MSD(\tau) = \left\langle \mathbf{R}_C^2(t+\tau) - \mathbf{R}_C^2(t) \right\rangle, \tag{1.10}$$

where $<>$ is the ensemble average taken over at time t with a time interval τ. According to the *Einstein-Smoluchowski relation*, diffusion coefficient D of the spherical particle is related to the MSD as

$$D = \frac{1}{6} \lim_{\tau \to \infty} \frac{d}{d\tau}(MSD). \tag{1.11}$$

According to the *Stokes' law* of creeping fluid motion around a sphere, the frictional/drag force exerted on a sphere of radius a, moving with a velocity v in a fluid with viscosity η is

$$F_d = 6\pi\eta a v, \tag{1.12}$$

thus mobility μ can be defined as the inverse of drag coefficient λ

$$\mu = \frac{1}{\lambda} = \frac{1}{6\pi\eta a}. \tag{1.13}$$

Further application of the *linear response theory* [27, 30] for an isolated sphere in viscous fluid leads to

$$D_0 = \mu k_B T = \frac{k_B T}{6\pi\eta a}, \tag{1.14}$$

where k_B is Boltzmann's constant ($1.381 \times 10^{-21} JK^{-1}$), T is the absolute fluid temperature (K). Eq. (1.14) is called *Stokes-Einstein relation*. The radius a of the particle can be deduced by equalizing the right hand side of Eq. (1.11) and Eq. (1.14).

A French physicist, Jean Perrin, validated experimentally [31] the prediction of Einstein and von Smoluchowski by recording series of positions for colloidal particles, as shown in Fig. 1.1. With these data, the diffusion coefficient was calculated, and therefore the radius of the colloidal particle. He further applied the work of Einstein and von

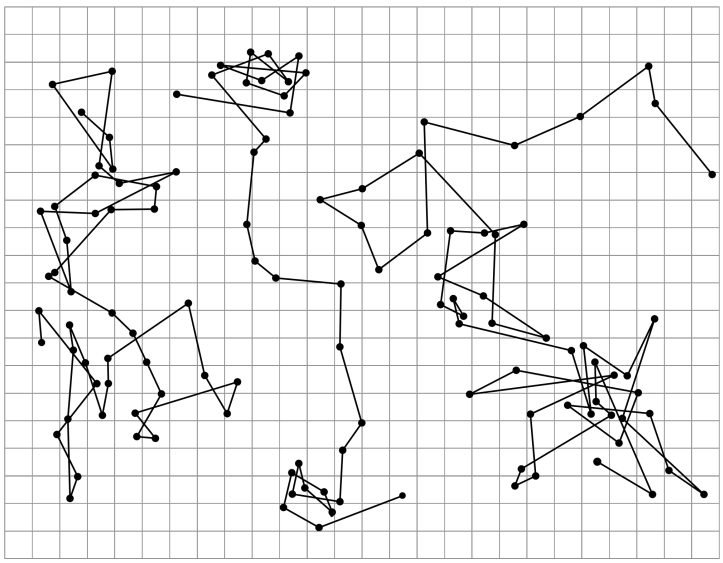

Figure 1.1: Locations and trajectories of colloidal particles released at $t = 0$ and measured for $t = [0, \tau]$: useful for calculation of mean squared displacement and thereafter diffusion coefficient of the particle.

Smoluchowski and back-calculated the Avogadro's number, the number of atoms in one mole, which earned him 1926 Nobel prize for physics.

Theoretically, a particle in both types of dispersion undergoes Brownian motion: the diffusion for a big particle in coarse dispersion is however very small, as D_0 is inversely proportional to a (see Eq. (1.14)). This also implies that a big particle does not feel much the agitation of the fast movements of surrounding fluid molecules. The time scale of diffusion can be estimated as

$$\tau_D = a^2/D_0 = 6\pi\eta a^3/k_B T, \tag{1.15}$$

which defines the time required by an isolated particle to diffuse over a length of its own size. For example, for a colloid with $1\mu m$ diameter in water at room temperature $(298K)$ $\tau_D \approx 1s$. In a coarser dispersion, diffusion might be hardly observed due to the fact that $\tau_D \propto a^3$, e.g., $2a = 100\mu m \rightarrow \tau_D \approx 10^6 s$.

There is no clear distinction between the sizes of particles in a non-colloidal dispersion and colloidal dispersion. Therefore, within a time scale of practical interest, whether particles in a dispersion are Brownian or non-Brownian effectively defines whether the dispersion is **colloidal** or **non-colloidal**. Vice versa, particles in colloidal dispersion are considered Brownian while particles in non-colloidal dispersion are considered non-Brownian. The differentiation between Brownian and non-Brownian particles is also extremely important in distinguishing the capabilities between numerical modeling schemes, as will be discussed in Section 1.2.

If a colloidal dispersion undergoes a shear flow characterized by a shear rate $\dot{\gamma}$, the *Péclet number* Pe is an important dimensionless quantity characterizing the ratio of

advective and *diffusive rate*,

$$Pe = \frac{advection}{diffusion} = \frac{va}{D_0} = \frac{\dot{\gamma}a^2}{D_0} = \frac{6\pi\eta\dot{\gamma}a^3}{k_BT}. \tag{1.16}$$

Péclet number also determines the degree to which the hydrodynamic force competes with the Brownian force, and this, as will be shown in Sec. 5, is important for determining the microstructure of a Brownian dispersion. For a very high Péclet number, e.g., $O(10^3)$, the diffusion rate is negligible compared to the advection due to the shear, therefore the Brownian motion can be neglected.

A remark is here in order: in a real dispersion of particles, the following hierarchy must hold, $\tau_{c_s} \ll \tau_v \ll \tau_D$, namely the time scales of different physical processes are widely separated, e.g., for a colloid with $1\mu m$ diameter in water at room temperature, $\tau_D = 10^9\tau_{c_s}$. Actually, the ratio between τ_D and τ_v results in the so called *Schmidt number*,

$$S_c = \frac{\nu}{D_0} = \frac{6\pi\nu^2\rho a}{k_BT}, \tag{1.17}$$

which characterizes the ratio of *momentum diffusivity* (viscosity) and *mass diffusivity*. For example, in a simple liquid like water, taking a as the molecule size, S_c is in the order of $O(10^3)$; taking a as the size ($e.g., 1\mu m$) of a colloidal particle in water, S_c is in the order of $O(10^7)$. This huge separation of time scales, often termed as Schmidt number problem, limits severely modeling and simulation schemes [32, 33].

Nevertheless, it is proved that the ratio of different time scales does not need to be realistic in simulations, as long as different physics processes are clearly identified or separated [34]. In a colloidal dispersion, this means that if $Ma \ll 1$, $Re \ll 1$, and $S_c \gg 1$ are specified, e.g., by choosing $\tau_\nu/\tau_{c_s} \sim O(10)$ and $\tau_D/\tau_\nu \sim O(10)$, the correct physics is qualitatively captured [34].

1.1.4 Solid-solid interaction: inter-particle forces

Due to the presence of a particle in a suspending medium, the disturbance induced in the fluid flow will cause hydrodynamic interactions (HIs) mediated by the medium with other particles. Due to the fact the HIs decay slowly in space, all particles may interact with all others, therefore the problem is intrinsically many-body. The HIs are source of the **major force** considered in this thesis.

By assuming that two spherical particles move towards each other with opposite constant velocities, the *normal* hydrodynamic forces experienced by them are repulsive and diverge as the gap between the two solid surfaces s vanishes, as shown in Fig. 1.2. The other two components of the HIs for two particles, namely *shear force and torque*, in close proximity are also singular, but their divergence is much smoother than for the normal force as $s \to 0$. The pairwise hydrodynamic forces between near-by particles are termed *lubrication forces* [12, 4, 14, 6], and have an extremely important role in determining the particle dynamics in a dispersion. For example, in a dispersion of two non-Brownian particles under shear, depending on their initial relative positions, a

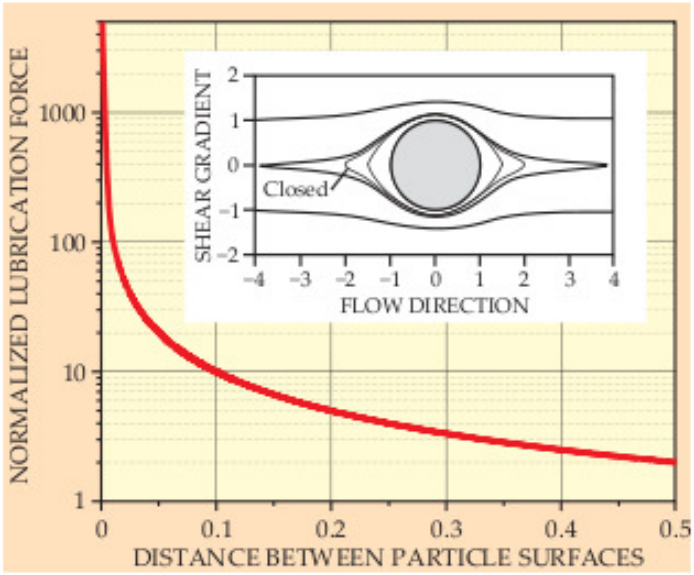

Figure 1.2: Lubrication force between two approaching particles and trajectories of two particles under shear flow, taken from Ref. [35].

closed or open relative trajectory can be formed [36, 37, 38, 39], as shown in the inset of Fig. 1.2. The two-particles' dynamics can be further extended and extrapolated to understand microstructure, and its link to the rheology of a dispersion with multiple particles [40, 41, 42, 43].

Although the hydrodynamic forces between particles are the same for non-colloidal and colloidal dispersions, the non-hydrodynamic inter-particle forces at short range are fundamentally different in the two cases, and need to be considered with caution in both analytical and numerical modeling.

In a colloidal dispersion, there are at least **three** possible types of inter-particle forces: *dispersion forces* arise from the quantum mechanical effects caused by fluctuations in the electron clouds surrounding atoms, which constitute the colloidal particles [4, 6]. The dispersion force is known as the *London-van der Waals force* between particles, and is the net effect of the polarizations on the atoms of one colloid caused by fluctuating electron cloud of atoms on another colloid. The dispersion force, under most circumstances, is an *attractive force* over a relatively long separation range r and can be calculated as the derivative of the interaction potential $\Phi^d(r)$ (see Refs. [44, 4, 45, 46, 6] for different potentials). In the absence of a stabilizing force, the particles will simply aggregate and settle out (for denser particles) or cream out (for lighter particles). Therefore, to impart stability, colloid must have some explicit means, to counteract this attraction, such as, surface force.

Surface forces arise from the proximity of colloidal surfaces, which can be either charged, or covered with ions, nanoparticles, surfactants, or surface-grafted polymers [4, 6]. For example, if the surface of a colloid is negatively charged via certain chemi-

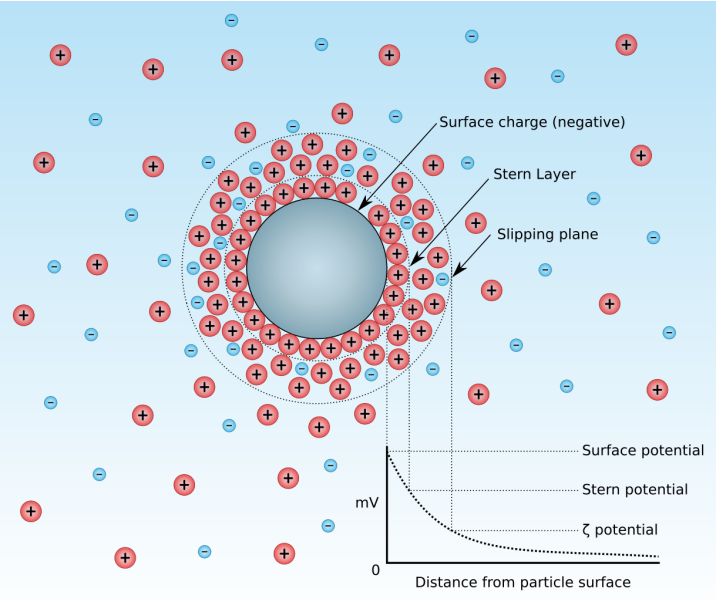

Figure 1.3: electrical double layer of ions and potential $\Phi^{el}(r)$ as a function of distance from the surface of a colloidal particle: the particle is negatively charged and dispersed in an electrolyte medium [44].

cal interactions (such as dissociated acid groups), a layer of cations (positively charged ions) from the dispersion medium is absorbed onto the surface. Another layer of anions (negatively charged ions) are attracted to the first layer due to the Coulomb's force, electrically screening the first layer [4, 6], as shown in Fig. 1.3. This structure is called *electrical double layer* or simply *double layer* in colloid science. The first layer, also named as *Stern layer*, of ions is considered immobile and this region acts as a capacitor over which the potential $\Phi^{el}(r)$ decays linearly, as first demonstrated by Hermann von Helmhotlz in 1850s [47]. The second layer of ions has both electric attraction and thermal motion rather than being firmly anchored. This region can be described by a diffuse model, as first proposed by Louis Georges Gouy [48] and David Chapman [49] independently, where the potential $\Phi^{el}(r)$ taken as zeta (ζ) potential decays rapidly with a decay constant know as *Debye length*, κ^{-1}. Two colloidal particles interact when they approach each other closely enough that their electrostatic potential $\Phi^{el}(r)$ overlap, that is, when their surfaces are within a few multiples of κ^{-1} [6]. When multiple particles are within the range of electrostatic interaction of each other, the repulsions are sophisticated *many-body interactions*.

For particles larger than a micron ($10^{-6}m$) in size, the double layers are usually small compared with the particle radius and the repulsive electrostatic force can be calculated in a pairwise manner as [50, 51, 52, 53]

$$\mathbf{F}^{rep}_{\alpha\beta}(s) = F_0 \frac{\tau e^{-\tau s}}{1 - e^{-\tau s}} \mathbf{e}_{\alpha\beta}, \tag{1.18}$$

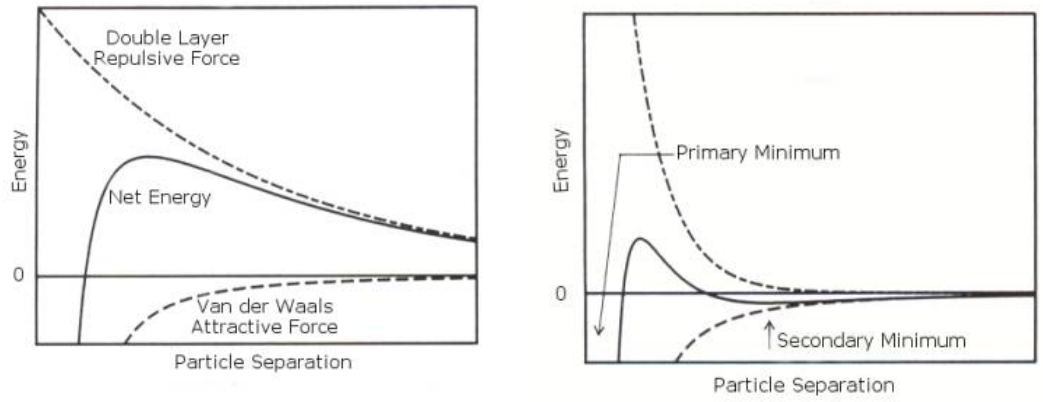

Figure 1.4: Energy of Derjaguin-Landau-Verwey-Overbeek potential: addition of London-van der Waals attraction and electrostatic repulsion [44]. Left: net potential being long-range repulsive; Right: net potential being long-range attractive.

to describe the force on particle α due to particle β by assuming constant surface charge of particles. s is the separation between particle surfaces; $\tau = \kappa a$, where a is particle radius and κ^{-1} is the Debye length; F_0 sets the magnitude and is given by

$$F_0 = 2\pi\epsilon\psi^2, \tag{1.19}$$

where ϵ is the electrical permittivity of the fluid and ψ is the surface potential when $s \to \infty$; τ^{-1} sets the active range and $|\mathbf{F}^{rep}_{\alpha\beta}|$ decays below $O(10^{-2}F_0\tau)$ when $s > 5.0\tau^{-1}$. This is a popular type of short-range repulsive force used for numerical modeling of colloidal and non-colloidal dispersions, and will also be considered in this thesis. A repulsive force is also extremely important to achieve practically an asymptotic state for an ideal non-Brownian suspension under shear flow [54, 55, 53].

Derjaguin and Landau, independently, Verwey and Overbeek proposed that the London-van der Waals attractive potential and electrostatic repulsive potential can be linearly added up, namely, $\Phi^{DLVO} = \Phi^d + \Phi^{el}$, which is denoted as Derjaguin-Landau-Verwey-Overbeek (DLVO) theory or potential [56], as shown in Fig. 1.4. Whether the net potential is repulsive or attractive in long range, how deep is the primary and secondary minimum, and how high is the electrostatic barrier are all crucial aspects to consider for the phase behavior of a colloidal dispersion [44, 4, 45, 46, 6]. A detailed discussion is beyond the scope of this thesis.

Besides the *electrostatically stabilization*, polymer brushes may be grafted on the surface of a colloidal particle to provide another type of surface force. With sufficient graft density and molecular weight, the *steric repulsion* between polymers on different particles can also prevent aggregation of particles. This is called *sterically stabilization* [4, 6]. The absorbed polymers may be replaced by nanoparticles or surfactants to provide the similar functionality.

Unlike the graft polymer used for stabilization, dissolved polymer can induce an attraction between particles. This is the third type of force, termed as *depletion force*. The attractive force between particles arises from the relative lower *osmotic pressure* in the inter-particle region, where polymers are excluded [4, 6].

In contrast to a colloidal dispersion, where non-hydrodynamic forces between particles are considered microscopically based on atomic level, non-hydrodynamic forces between particles in a coarse dispersion or non-colloidal dispersion are taken into account in a macroscopic manner. Repulsive force $\mathbf{F}_{\alpha\beta}^{rep}$ of solid contact is generally present in the normal direction between particles. In addition, frictional tangential force $\mathbf{F}_{\alpha\beta}^{fr}$ and torque $\mathbf{T}_{\alpha\beta}^{fr}$ co-exist, both of which are proportional to the tangential spring $\xi_{\alpha\beta}$ [57, 58, 59, 60]. As $\mathbf{F}_{\alpha\beta}^{fr}$ and $\mathbf{T}_{\alpha\beta}^{fr}$ are subject to Coulomb's law, they are limited by $\mu^{fr}\mathbf{F}_{\alpha\beta}^{rep}$ being μ^{fr} the static friction coefficient, which means the dynamic friction is not bigger than the static one. Since we do not intend to model frictional spheres in this thesis, details are omitted and can be found in the references given above.

1.1.5 Summary

Under the conditions and assumptions mentioned in the previous sections, namely, for the suspending fluid continuous hydrodynamic equations, no-slip boundary condition at fluid-solid particle interface, time scales separation ($\tau_{c_s} \ll \tau_v \ll \tau_D$), and inter-particle forces, a proper model of a particle dispersion can be established.

It is since the work of Einstein and von Smoluchowski [27, 29, 28], more than a century ago, that the dynamics of a *single* Brownian particle is understood. However, it was not until 1970s that a series theoretical work of Batchelor [40, 41, 61, 42, 43] established a full micromechanical framework for the dynamics, microstructure, diffusion and rheology of dispersions of *multiple* particles, by combining statistical mechanics and hydrodynamics concepts. The theoretical work is not only important for our fundamental understanding of dispersions in simple scenarios, but also paved ways of applying computer programming to model and simulate more complex applications. A remarkable numerical scheme termed Stokesian dynamics [62] is built upon such micromechanical framework and will be explained in Sec. 1.2.

As the spectrum of applications for dispersions is extremely wide, we focus here on the aspects of hydrodynamics, diffusion, microstructure and rheology. We arm ourselves with numerical modeling and simulation as tools to study those targets. The modeling and simulation are not only topics which are still subject of intense research [10], but also become an indispensable tool to target and optimize specific functionality of novel devices operating under microfluidics conditions [8, 63]. Manipulation, sorting and mixing of micro/nano-size objects are becoming the central focus of nanoparticle technology as well as, in the biomedical field, of novel platforms for hand-held diagnostics [64]. It is therefore extremely important to develop simultaneously theoretical and numerical models to fill the gap with rapidly evolving industrial applications. In **Section 1.2**, we review a large, but not exhaustive, list of existing numerical schemes used for modeling multiphase dispersion. More attention is paid to the schemes, which are widely used,

such as, Stokesian dynamics; only key concepts are explained, if the schemes are only used within few groups. Advantages and disadvantages are pointed out for all numerical schemes. Details of the numerical scheme used in this work, namely, **smoothed dissipative particle dynamics (SDPD)**, with all its unique features, will be explained in a separate **Chapter 2**.

1.2 Review on numerical modeling schemes

There are several review articles on the topic of particle dispersion, and probably even more review articles on the subject of numerical discretization schemes. However, there are only few articles reviewing numerical modeling in the context of particle dispersion. For example, an early review of Brady & Bossis in 1988 [62] discusses exclusively applications of Stokesian dynamics in (non)colloidal dispersion; Whittle & Dickinson 2001 [65] pointed out some issues and complications at the initial development of dissipative particle dynamics method on simulating colloids; Koumoutsakos 2005 [66] gives a review of particle methods used for general multiscale flows; van der Sman 2009 [67] favors lattice Boltzmann method by comparing with other methods to simulate confined suspension flow at multiple length scales; Fujita & Yamaguchi 2010 [68] reviews briefly some recent contributions to different representative methods used for mesoscopic modeling of colloidal dispersions.

Here we intend to provide an extensive, but not exhaustive, review of numerical schemes developed for modeling colloidal and noncolloidal dispersions. Some methods are explained clearly, as they have great influence; others are only presented with key concepts without going into technical details. The key issue of all numerical schemes is on the modeling of hydrodynamic interactions (HIs) among the particles, where Navier-Stokes (or Stokes) equations are solved. In particular, for a colloidal dispersion of Brownian particles the fluctuation-dissipation theorem (FDT) has to be satisfied [13, 69] to form the so-called fluctuating hydrodynamic equations (FHE). If the fluid flows described by Navier-Stokes equations or FHE are solved *explicitly* by a numerical scheme and no additional model is assumed, it is called a *direct numerical simulation (DNS)*. Some other simulations apply certain model, to avoid a thorough computation. An example is Stokesian dynamics method, which applies analytical or semi-analytical solutions of Stokes flow on multiple spheres. In this way, the fluid flows are *implicitly* or *partially-implicitly* modeled, it does not need to be solved numerically over the entire domain and the computational cost is significantly reduced. General advantages and disadvantages of various schemes for the solutions of deterministic HIs or FHE in different applications will be pointed out and compared.

Another crucial aspect of these schemes is how solid particles are coupled with fluid flow, the so-called fluid-structure interaction (FSI) problem. The treatment of particles is mostly done in *Lagrangian* framework so they can translate and rotate freely. Depending on how fluid flow are modeled, we classify existing numerical schemes into *Eulerian-mesh-based* and *Lagrangian-mesh-free* methods. Therefore, a resultant model for dispersion is either Eulerian-Lagrangian coupling or Lagrangian-Lagrangian coupling.

1.2.1 Mesh-based methods

The majority of numerical schemes are mesh-based methods, such as *finite difference (FDM)/finite volume (FVM)/finite element method (FEM)* [70, 71], *spectral/hp element* (high order FEM) [72], and *boundary element* [73], which are all widely used in *computational fluid dynamics* for general purpose.

The major applications of these methods are concerning macroscopic flows including aerodynamics, free surface flow, turbulence, and so on. The application of these methods in multiphase flows is also quite active. Since the discretizations using these methods are based on Eulerian meshes, the interfaces among different fluid phases or between fluid phase and solid phase must be identified dynamically using an advanced technique during a simulation.

Interface tracking techniques

In combination with a mesh-based discretization, different techniques for tracking interfaces may be used, such as, *immersed boundary method* [74, 75, 76], *volume of fluid* [77], *front tracking method* [78, 79], and *level set method* [80]. These techniques are usually either good at maintaining a sharp interface or for conserving mass, and are active research areas under continuous improvement. They are used for general multiphase flows, including different fluids mixing, fluid-solid coupling, and fluid-structure interaction.

For the particular simulation of a fluid-solid two phase dispersion, there are also other simpler techniques with relative short history: by considering a non-zero thickness at fluid-solid interface, Yamamoto and co-workers have developed a technique describing the interface by a smooth function, and termed the technique as *smoothed profile method (SPM)* [81, 82, 83, 84]; Glowinski and colleagues proposed *distributed Lagrange multiplier (DLM)* to constrain the motion of rigid particles in a *fictitious domain (FD)* [85, 86]; Tanaka and collaborators have proposed *fluid particle dynamics (FPD)* [87, 88] by assuming the solid phase being a fluid with viscosity η_s much larger than the fluid viscosity η. If the ratio $\eta_s/\eta \to \infty$, rigid motions of particles are achieved. In practice, however, the ratio is kept finite leading to particles with certain internal elasticity. These techniques are designed specifically for fluid-solid two phase dispersion, and can be often considered as subset of those techniques (immersed boundary method, level set method, etc) developed for general multiphase flow. They are computationally effective, but not very versatile. Coupled with these techniques, the host fluid flows must be solved explicitly by a DNS method, such as FDM/FVM/FEM.

It is interesting to note another promising method termed *force coupling method (FCM)*, which has been developed by Maxey and his students. FCM solves Navier-Stokes flow around particles by a finite-valued force multipole expansion, where the force distribution of any spherical particle acting on the fluid is coupled by a Gaussian envelope function [89]. This envelop function plays a similar role as the smooth function in SPM, to locate fluid-solid interface. The slip or no-slip boundary condition on a particle's surface is only approximately satisfied, which alleviates the severe numerical stiffness of the problem associated with exact boundary condition enforcement.

Lubrication force between particle and particle or particle and wall is also incorporated into an improved version of FCM [90, 91, 92, 93], which is then used to study the dynamics, microstructure and rheology of non-Brownian suspensions under Couette flow [94, 95, 96, 97]. FCM is also extended to model non-spherical particles, such as ellipsoids [98]. The host fluid flows must be solved explicitly by a DNS method, such as, spectral/hp element method.

All the discretization methods in this class rely on the deterministic Navier-Stokes equations for macroscopic flows. Therefore, on the one hand, they are promising for considering also the inertial effects, in contrast to the Stokesian dynamics (explained later); on the other hand, without further extensions, they can only simulate coarse noncolloidal dispersions, namely, non-Brownian particles in suspension.

Fluctuating hydrodynamics

For modeling a colloidal dispersion, *thermal fluctuations* need to be incorporated into the Navier-Stokes equations, meanwhile satisfying the fluctuation-dissipation theorem (FDT) [13]. The resulted form is the so-called fluctuating hydrodynamic equations (FHE) [13] and it corresponds to a set of stochastic partial differential equations. It must be noted that even if the continuum differential equations satisfy the FDT, it does not automatically imply that the corresponding discrete equations, (e.g., central difference scheme in FDM) will necessarily satisfy the FDT too [99, 100]. Thermodynamic consistency of the discrete equations can be ensured if the discretizations are derived within the GENERIC (general equation for the nonequilibrium reversible-irreversible coupling) framework proposed by Grmela & Öttinger 1997 [101, 102]. Obeying the GENERIC structure, Español and co-workers discretized the FHE for a pure fluid with thermodynamic consistency by using FVM on Voronoi tessellations [99, 103]. Following the same methodology, Pantankar and collaborators cast a Brownian particle together with fluid in the GENERIC structure [100, 104]. Their discretization is FVM performed on cubic grids meanwhile DLM/FD technique is used to incorporate the motion of rigid particles [85, 86, 100, 104].

Solutions of the Boltzmann equation

There are also numerical methods, which do not rely directly on the Navier-Stokes equations. For example, the direct simulation Monte Carlo (DSMC) method proposed by Bird uses a probabilistic simulation to solve Boltzmann equation [105, 106, 107]. It is a powerful approach, and in fact the only possible numerical method for simulating high *Knudsen number* (Kn) rarefied flows in complex geometries, where $Kn = \lambda/a$ being λ the molecule mean free path and a characteristic geometric length. Although DSMC is extended to solve low Kn number continuum flows, it is neither efficient nor accurate as a continuum approach solving Naiver-Stokes equations.

A recently modified version of DSMC receives great attention, which has been derived by Malevanets & Kapral 1999 [108]. The novel version is named multiple particle collision dynamics (MPCD) and sometimes termed stochastic rotation dynamics (SRD) [109, 110,

111, 34]. In MPCD/SRD, the system is *coarse-grained* into cells of regular lattice and the fluid is represented by particles. Positions and velocities of the particles are treated as continuous variables, which are advanced with a streaming step. As a second step, within each cell particles exchange momentum through a multiple collision and rotate velocities relatively to the velocity of the cell-mass-center. The dynamics satisfies the conservation of mass, momentum and energy and thermal fluctuations are naturally present during the collision step. Couplings of mesoscopic MPCD/SRD solvent with solute [112] or polymer chain [113] using molecular dynamics (MD) is straightforward. The HIs between the solvent and solid inclusions or walls are also validated [114]. Ihle & Kroll 2001 [109] realized that the lattice needs to be shifted carefully to satisfy the *Galilean-invariance*, a feature that lattice gas automata [115] does not have for free either.

It is also worth to mention the lattice Boltzmann method (LBM) [116, 117, 118, 119, 120, 121, 122], which solves the discrete linearized and pre-averaged Boltzmann equation on a lattice and can be used for gas or liquid flows as well as for particulate microflows. The solutions are provided by a streaming process to advance position and a collision process to exchange momentum using Bhatnagar-Gross-Krook operator [123]. The macroscopic hydrodynamics can be recovered correctly by the LBM [119]. To have a thermal LBM, fluctuations can be introduced using different approaches, such as, multi-speed approach [124], passive scale approach [125], and thermal energy distribution approach [126]. A notable problem occurring in the LBM simulations of particle dispersion is, however, related to the unclear solid particle size, which is not known a priori. This deficiency is in part related to the representation of particle using finite number of grid points and the bounce-back rules for ensuring no-slip boundary condition. One needs, therefore, to calibrate the simulations with a so-called hydrodynamic radius [127], which can be a complex function of the lattice size [128], as well as the solvent kinematic viscosity [129]. Recently, some of these deficiencies have been significantly reduced by employing multiple relaxation time approaches [129] or higher-order boundary conditions [130].

1.2.2 Mesh-free methods

To model a multiphase dispersion, one could follow Newton's equation of motion for solvent molecules and perform *molecular dynamics (MD)* [131, 132], which would need to take into account each microscopic detail. Although the modern computing power is very large, the MD simulations are still restricted to a very small length or time scale. The longest MD simulation achieved so far is in the order of $1ms$ $(10^{-3}s)$ [133, 134], which is still far from the typical diffusion time $\sim 1s$ of a colloid. In addition, there is also a huge spatial gap between molecules ($\sim 0.1nm$) and colloidal particles ($\sim 1\mu m$). MD is more often used for simulations of the third type of dispersion, namely, solution, but rarely for multiphase dispersion.

Brownian dynamics (BD) method [135] was invented to describe the motion of macromolecules or colloids at the simplest level of *overdamped limit*. In this limit, the kinematic viscosity ($\nu = \eta/\rho$) is so high that momentum of a colloid already relaxes in a time scale,

in which its position barely moves. Therefore, BD method can be derived by neglecting the inertial term in *Langevin dynamics*. The latter accounts for the omitted degrees of freedom by stochastic differential equations and assumes the collisions with solvent molecules introducing a random displacement of the colloid [136]. BD has often been amended with simple analytical representations of HIs, such as the Oseen tensor [137], but still lack for the accurate description of HIs, especially in simulating dispersion of multiple particles.

BD is considered as a subset of *Stokesian dynamics (SD)* [62], which takes into account proper HIs between multiple particles [52]. The Brownian motion of particles can also be incorporated in SD, just as it is done in BD, satisfying the FDT [138]. SD is very efficient for computing HIs between spherical particles within Stokes flow and has been dominating the simulation work on multiphase dispersions almost two decades and therefore, deserves detailed explanations.

SD was first invented by Bossis and Brady in 1984 [52]. In this original article, the authors simulated dynamics of a monolayer of spherical particles under linear shear flow with shear rate $\dot{\gamma}$, where particles interact through both hydrodynamic forces and Derjaguin-Landau-Verwey-Overbeck type colloidal forces [56]. In the application considered, particle Reynolds number or Bagnold number [139] $Re = va/\nu = \dot{\gamma}a^2/\nu \approx 10^{-5}$ is neglectable; Péclet number $Pe = 6\pi\mu a\dot{\gamma}/k_BT$ is $O(10^2)$ such that Brownian motion is not important and also neglected. Due to the difficulty of modeling many-body HIs between particles, HIs are assumed to be pairwise-additive, which was motivated by MD simulations. However, pairwise additivity provided two options for the authors. Pairwise additivity in the mobility matrix $\mathbf{R}^{-1}$ corresponds to a superposition of velocities (referred to as superposition), while in the resistance matrix $\mathbf{R}$ it is a superposition of forces (referred to as inversion, since $\mathbf{R}$ needed to be inverted to calculate velocities). The former one proves to be unrealistic, since relative velocity between two particles is not guaranteed to vanish as their separation becomes small, i.e., as surface gap $s \to 0$, but it should disappear according to lubrication theory [39]. In contrast, pairwise additivity in $\mathbf{R}$ is quite different. Rather than considering pairs of particles alone in the fluid, when matrix $\mathbf{R}$ is inverted to calculate velocities, all particles are considered simultaneously to have zero total force, which may be considered as *semi-many-body* interactions in some sense. Moreover, lubrication forces are preserved for the methodology of inversion, which is very important for small separations between particles, especially in a concentrated dispersion.

There is no closed-analytical-solution for all relative separations between pairs of spheres: at large surface-surface separations, far-field analytical expressions are available by the method of reflection [12]; at smaller distance compared to the radius ($s = 0{-}0.2a$), analytical results are used from lubrication theory [14, 140]; tabulated numerical results are used for intermediate separations ($s = 0.2a - 3, 4a$). These results are pieced together to construct the final resistance matrix $\mathbf{R}$ in SD. At the time of their original article [52], the complete compilation for all separations by Jeffrey and Onishi [140] was not available yet, they had to use certain approximations.

A series theoretical work of Batchelor, combining hydrodynamics with statistical mechanics, established a full micromechanical framework for suspensions of *multiple* parti-

cles [40, 41, 61, 42, 43]. Based on this framework, dynamics, microstructure, diffusion and rheology can all be calculated in SD simulations of suspensions [141, 142, 143, 144, 145, 146, 147, 148, 149]. However, the SD simulations had been limited to a small number of particles until an accelerated version was proposed [150, 151], which enabled simulation of a total number of particles in the order of $O(10^3)$. To calculate the many-body long-range HIs, the accelerated Stokesian dynamics (ASD) uses an Ewald-summation technique transformed in Fourier space, leading the algorithm scaling as $O(NlnN)$ being N the total number of particles [150, 151].

Despite of the important contributions of SD to our understanding of dynamics, diffusion, microstructure and rheology of particle dispersions, there are at least three obvious limitations of the method:

1. SD assumes that the fluid is perfectly incompressible and infinitely viscous ($Re = 0$), which are strong approximations under specific conditions. In addition, the time scales between motions of fluid and those associated with particles are completely separated in SD, which excludes the short-time motion of Brownian particles over kinematic time scale. Transitional behavior with small inertia is not considered, although inertia is ineluctable and sometimes crucial [152, 153, 154];

2. Modeling arbitrarily shaped objects is not an easy task in SD and requires essential modification of the standard framework [155]. Generalization of SD to model nonspherical particles has been recently proposed in Ref. [156]. In this approach arbitrarily shaped rigid particles are modeled as clusters of several spheres which still interact via the usual SD forces, therefore extending its range of applicability while increasing significantly the computational cost of the method;

3. External/complex boundary geometries, such as confining walls, are difficult to model within the SD framework. One way is to fix a plane layer of spheres to represent a wall, and allow wall spheres to interact with dispersed spheres using the SD algorithm [157, 158]. Thereafter, stress on the wall is obtained by collecting forces on the wall spheres. However, this approach does not give satisfactory results in many applications, especially it is difficult to model an arbitrary boundary surface. In low-Reynolds-number hydrodynamics, mobility and resistance tensors for particles must be symmetric, positive definite, even with external wall boundaries. This constrain was not always guaranteed in previous published work, until an improved version of SD by Swan & Brady 2007 [155], where extra care was taken to ensure the genuine properties of mobility and resistance tensors. However, this work was restricted to particles near a *single* wall. Swan & Brady 2010 [159] further investigated hydrodynamics between *two* walls, but this time the total number of particles was only *one*. Finally, in the work of Swan & Brady 2011 [160], HIs of multiple particles between two parallel plane walls can be computed completely and accurately. As in the work of Sierou & Brady 2001 [150], Swan & Brady 2011 [160] also considered Ewald-like summation to accelerate the algorithm with $O(NlnN)$ scaling. Nevertheless, all SD simulations involving particles coupled with external wall(s) require massive knowledge and implementation

of algebra, which is far from making the method eligible for practical problems in micro-channel. Based on the complex work for planar walls, the extension to arbitrary boundaries in SD is imagined to be very difficult, if possible at all.

SD is based on the solutions around spheres in Stokes flow, therefore, solvent is modeled *implicitly* already and computations of dynamics are significantly simplified. However, this simplification also represents its weakness. Another approach based on the Stokes equations but allowing for arbitrarily shaped particles uses *boundary integral analysis* [161]. Here, particle surfaces are discretized and a set of boundary integral equations based on the expansion of the Stokes equations must be solved for each surface element.

A promising group of mesh-free methods, namely, *smoothed particle hydrodynamics (SPH)* [162, 163], *dissipative particle dynamics (DPD)* [164, 165], *and smoothed dissipative particle dynamics (SDPD)* [166], emerge in the comparison due to their flexibility and efficiency. In particular, they do not need to assume Stokes regime and can be considered to solve many of the limitations residing in other methods mentioned above, for example, no need of interface tracking. In fact, SPH used as a macroscopic solver for the Navier-Stokes equations is a DNS resolving fluid flow explicitly, while DPD and SDPD can be considered as mesoscopic solutions of the fluctuating hydrodynamic equations. SPH/DPD/SDPD methods are selected and investigated in this thesis, therefore they will be explained separately in details in Chapter 2.

A similar method to SPH was invented separately by Koshizuka and colleagues in 1990s [167, 168] and termed *moving particle semi-implicit method (MPS)*. MPS is fundamentally not much different from SPH, except that the solutions are obtained using a semi-implicit prediction-correction process rather than a fully explicit one as used in SPH method. Formally, the Navier-Stokes equations can be transformed into *vorticity equations* by taking the *curl* of the velocity vector in the former and then be solved numerically by *vortex method (VM)* [169, 66], which has similar approximation techniques as those used in SPH. However, no effort has been shown to incorporate fluctuations into MPS or VM method and are therefore limited approaches to simulations of colloidal dispersions.

1.2.3 Summary

All the DNS methods mentioned above suffer of a common inaccuracy in the case of a dense dispersion, where particles are in close proximity and occupy the major volume of the dispersion. This deficiency is generally a difficult task to solve, as the numerical resolution needs to be sufficiently high to model accurately the flows of extremely thin film, namely, *lubrication forces*, between the particles. Some groups target this problem with multi-resolutions, e.g. Hulsen and co-workers adapted the mesh resolutions near the surface of spherical particles in an extended FEM [170, 171, 172, 173]. Nevertheless, only solutions with few particles are possible, due to the extremely expensive computational cost. A common strategy circumventing this difficulty is by incorporating in addition to the long- and intermediate-range HIs resolved by a DNS method, a *pairwise lubrication model* [118, 120, 122] at short distances between particles, just as it is done in SD method.

Although HIs are truly multi-body, the (pairwise) incorporation of lubrication force can be justified by the following fact: lubrication force takes place at very short range between particles and therefore the many-body HIs of lubrication forces among multiple near-by particles are hindered and screened by the presence of the other particles. This is the approach considered also in this work.

Besides the advantages and disadvantages pointed out above, we provide below a general comparison between various schemes in different aspects.

- **interface tracking**: due to the physical nature of multiphase dispersion, interface between fluid phase and solid phase must be identified with care in any scheme. The mesh-based methods coupled with particles, or Eulerian-Lagrangian coupling methods, always have to use advanced techniques to track such interface, which is tedious and computationally expensive. Moreover, the interface tracking techniques often need to be adjusted according to different scenarios. Mesh-free schemes have clearly advantage in this aspect, where both fluid and particles move in a Lagrangian framework and interface is therefore automatically captured. Nevertheless, boundary condition at the interface must be implemented with a small extra effort in the mesh-free schemes.

- **computational cost**: whereas BD/SD methods model the solvent *implicitly* using analytical solutions, other methods (either mesh-based or mesh-free) have to model the solvent *explicitly*. It is apparent that the implicit-solvent modeling, although less flexible, is computationally more efficient.

  For more realistic and complex problems, such as *moving multiple-particles with possibly arbitrary shapes*, mesh-based methods are more flexible but require frequent remeshing of the fluid domain and exhausting tracking of interfaces. In contrast, mesh-free methods need only a small extra effort for this problem.

- **error analysis**: mesh-based methods have clear advantages over mesh-free methods in the aspect of error analysis. For the former using regular meshes, numerical errors are obtained analytically, for example, by using a Taylor expansion; for the latter using Lagrangian elements or numerical particles, error analysis can be much more difficult. To get an estimated error, the analysis of a mesh-free particle method often assumes the numerical elements on a regular lattice [174], which does not take place under real flow conditions, where random configurations usually occur. Due to the disorder of particle configurations in a mesh-free method, the numerical error is difficult to control and often relatively larger than in a mesh-based method. This deficiency, however, may be reduced via *remeshing* procedures [175].

Regardless of the discretization adopted is mesh-based or mesh-free, the incorporation of thermal fluctuations into the model can also determine the potential applications:

- **fluctuations on particle**: if thermal fluctuations are introduced directly on the colloid level (BD/SD and similar methods), the shape of the colloid is restricted

to be spherical, since the agitations of fluid molecules on the colloid are assumed to be symmetric on the surface.

- **fluctuating stress in hydrodynamic equations**: if thermal fluctuations are introduced on the fluid element level, Brownian motion of a colloid results from the coupling at the fluid-solid interface and there is no need to add extra fluctuations on the colloid level. Therefore, in principle any shape of a colloid can be modeled (DPD/SDPD, LBM, and DLM/FD methods).

1.3 Outline

In **Chapter 2**, we present different fundamental formulations of the particle methods used in this work, namely SPH, DPD, and SDPD and also give general remarks on their applications.

In **Chapter 3**, we give a summary of our paper published in the international peer-reviewed journal *Physics of Fluids*. This paper proposes a multiscale modeling of particle dispersions with SDPD method. It validates the non-Brownian dynamics of a single particle with fluid interactions and hydrodynamic interactions between two particles. It also examines the dynamics of a single Brownian particle, especially its coupling with an external wall boundary.

In **Chapter 4**, we give a summary of our paper published in the international peer-reviewed journal *Computer Physics Communications*. This paper points out the difficulty of integrating the dynamics of multiple particles, due to the diverging lubrication force at short inter-particle range. It provides a novel integration scheme by splitting the force contributions on particles, which allows to simulate highly concentrated suspensions.

In **Chapter 5**, a special application is considered, namely, the *shear thickening* of concentrated particle dispersions, which has been attracting significant attention in the last decades. This is selected as an application area of our numerical model using SDPD. The topic is still under intense debates in the community, for which we shall give a review in the beginning of the chapter. In the second part of the same chapter, we give a summary of our paper submitted to the international peer-reviewed journal *Physical Review E*. This paper contains a simulation work of concentrated suspension under confined Couette flow. The hydrodynamic/continuous shear thickening rheological behavior is observed and confinement effects are examined in details. From our knowledge, it is the first work done on hydrodynamic shear thickening of concentrated suspension under confinement. The work has been conducted at the TUM and Xin Bian has initiated the collaboration with Prof. Norman J. Wagner at University of Delaware, U.S., who has prominent experience and reputation on shear thickening of colloidal dispersions.

2 Smoothed dissipative particle dynamics

2.1 Smoothed particle hydrodynamics

Smoothed particle hydrodynamics (SPH) method was invented in 1970s in the astrophysics community [162, 163], where the *inviscid* hydrodynamics described by *Euler equations* needed to be solved. Problems involved in astrophysics are often too complex to handle by a mesh-based method, as open-boundaries are often encountered. The Lagrangian and meshless feature of SPH received attention very soon and attained great popularity [176, 177, 178].

The essence of SPH is an interpolation process allowing any function defined on a given domain to be expressed in terms of values at a discrete set of N disordered points — the particles [177]. The algorithm may be interpreted as two steps of approximation:

Kernel approximation

This first step is the so called *integral representation* or *kernel approximation*, of a given field function. The concept of integral representation of a function $f(\mathbf{r})$ starts from the following identity:

$$f_I(\mathbf{r}) = \int_\Omega f(\mathbf{r}')\delta(\mathbf{r}-\mathbf{r}')d\mathbf{r}', \tag{2.1}$$

where $f(\mathbf{r})$ is a function of a two or three-dimensional position vector $\mathbf{r}$, $f_I(\mathbf{r})$ is the integral representation, Ω is the area or volume of the domain, and $\delta(\mathbf{r}-\mathbf{r}')$ is the *Dirac delta function* defined as

$$\delta(\mathbf{r}-\mathbf{r}') = \begin{cases} \infty & \mathbf{r}=\mathbf{r}'; \\ 0 & \mathbf{r}\neq\mathbf{r}'. \end{cases} \tag{2.2}$$

As long as $f(\mathbf{r})$ is continuous in Ω, $f_I(\mathbf{r}) = f(\mathbf{r})$ is exactly satisfied. If $\delta(\mathbf{r}-\mathbf{r}')$ is replaced by a bell-shaped smoothing function $W(\mathbf{r}-\mathbf{r}', h)$, the integral representation of $f(\mathbf{r})$ becomes

$$f_I(\mathbf{r}) = \int_\Omega f(\mathbf{r}')W(\mathbf{r}-\mathbf{r}', h)d\mathbf{r}', \tag{2.3}$$

where W is termed *smoothing kernel*, h is the smoothing length defining the influence area or volume of W. In addition, to be consistent W must satisfy the *delta function*

property and *normalization condition*

$$\lim_{h\to 0} W(\mathbf{r}-\mathbf{r}',h) = \delta(\mathbf{r}-\mathbf{r}'), \quad \int_{\Omega} W(\mathbf{r}-\mathbf{r}',h)d\mathbf{r}' = 1. \tag{2.4}$$

In practice, W usually has a compact support such that

$$W(\mathbf{r}-\mathbf{r}',h) = 0, \quad for \quad |\mathbf{r}-\mathbf{r}'| > \kappa h, \tag{2.5}$$

where κ is a constant defining the effective (non-zero) area or volume of W. The compact area or volume is called support domain of the smoothing kernel W with a spherical cut off radius $r_c = \kappa h$.

As long as $h > 0$, $W(\mathbf{r}-\mathbf{r}',h)$ is not exactly equal to $\delta(\mathbf{r}-\mathbf{r}')$, therefore $f_I(\mathbf{r})$ only approximates $f(\mathbf{r})$. It can be shown that

$$f(\mathbf{r}) = f_I(\mathbf{r}) + e_1(h^2), \tag{2.6}$$

where we ensure W to be an even function and the integral representation is second order accurate with a residual error $e_1(h^2)$ [179].

In this work we use a quintic spline kernel [21]

$$W(s) = c_D \begin{cases} (3-s)^5 - 6(2-s)^5 + 15(1-s)^5, & 0 \le s < 1; \\ (3-s)^5 - 6(2-s)^5, & 1 \le s < 2; \\ (3-s)^5, & 2 \le s < 3; \\ 0, & s \ge 3, \end{cases} \tag{2.7}$$

where $W(s)$ is symmetric and the scalar $s = |\mathbf{r}-\mathbf{r}'|/h$; the cut off radius of compact support is $r_c = 3h$ and normalization coefficient $c_2 = 63/(478\pi {r_c}^2)$ and $c_3 = 81/(359\pi {r_c}^3)$ in two and three dimensions respectively [21, 179].

The integral representation of the derivatives of function f can be deduced similarly, as shown in Refs. [177, 179, 180, 181, 166].

Particle approximation

For sake of numerical computation, the continuous integral representation $f_I(\mathbf{r})$ must be converted to a summation over a finite number of discrete points (discrete representation), as shown in Fig. 2.1. The disordered points in Fig. 2.1 are termed particles in SPH and the discretization process is carried out as follows.

The infinitesimal area or volume $d\mathbf{r}'$ in Eq. (2.3) at location of particle j can be replaced by the finite area or volume $\mathcal{V}_j$, which is related to the mass of the particle m_j by

$$m_j = \mathcal{V}_j \rho_j. \tag{2.8}$$

ρ_j is the density of particle j, $\forall j = 1, 2, ..., N$, and N is the total number of particles. Therefore, the continuous integral representation for f in Eq. (2.3) at position $\mathbf{r}$ can be

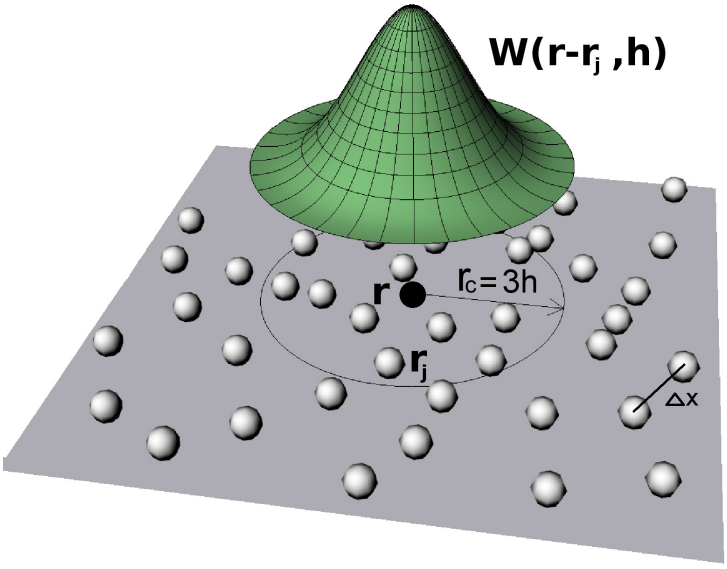

Figure 2.1: compact support of particle approximation using finite number of particles: $r_c = 3h$ for a quintic spline

written in discrete form as follows,

$$f_P(\mathbf{r}) = \sum_{j=1}^{N} f(\mathbf{r}_j) W(\mathbf{r} - \mathbf{r}_j, h) \mathcal{V}_j \tag{2.9}$$

$$= \sum_{j=1}^{N} \frac{m_j}{\rho_j} f(\mathbf{r}_j) W(\mathbf{r} - \mathbf{r}_j, h) \tag{2.10}$$

$$= \sum_{j=1}^{N} \frac{1}{d_j} f(\mathbf{r}_j) W(\mathbf{r} - \mathbf{r}_j, h), \tag{2.11}$$

where $d_j = m_j/\rho_j = 1/\mathcal{V}_j$ is the number density of particle j. The continuous integral can be represented by the discrete form as

$$f_I(\mathbf{r}) = f_P(\mathbf{r}) + e_2(\Delta x/h), \tag{2.12}$$

where Δx is the mean neighboring particle distance and $e_2(\Delta x/h)$ is the residual error. Since N is finite, $f_P(\mathbf{r})$ is an approximation of $f_I(\mathbf{r})$ and $e_2(\Delta x/h) > 0$, this process is termed *particle approximation*.

To summarize, the approximations performed involve two steps:

$$f(\mathbf{r}) = f_I(\mathbf{r}) + e_1(h^2) = f_P(\mathbf{r}) + e_1(h^2) + e_2(\Delta x/h). \tag{2.13}$$

Therefore, it is crucial to manipulate both the kernel smoothing length ($e_1(h^2)$) and number of neighboring particles ($e_2(\Delta x/h)$) to control the overall numerical error of a SPH simulation.

Discrete form of deterministic hydrodynamics

We apply the two-step approximations of SPH to discretize the hydrodynamic equations, Eqs. (1.1) and (1.2) in space. The continuity, Eq. (1.1), is automatically satisfied if particle density is evaluated as [166]

$$d_i = \frac{1}{\mathcal{V}_i} = \frac{\rho_i}{m_i} = \sum_j W_{ij}, \quad \dot{\mathbf{r}}_i = \mathbf{v}_i, \tag{2.14}$$

where d_i, $\mathcal{V}_i$, m_i, ρ_i, $\mathbf{r}_i$ and $\mathbf{v}_i$ are number density, volume, mass, mass density, position, and velocity of particle i, respectively; each particle has a constant mass m_0; $W_{ij} = W(r_{ij})$ is the bell shaped quintic spline defined in Eq. (2.7), which depends on the inter-particle distance r_{ij} and vanishes beyond a cutoff radius r_c, that is, $W_{ij} = 0$ for $r_{ij} > r_c$. Provided that the total number of SPH particles remains constant, total mass is exactly conserved and Eq. (2.14) provides an operative way to calculate the density.

Application of the SPH approximations to Eq. (1.2) produces the following equations for the particle momenta in the Lagrangian formulation [166, 182]

$$\begin{aligned} m_i \dot{\mathbf{v}}_i &= \sum_j \mathbf{F}^C_{ij} + \sum_j \mathbf{F}^D_{ij} + \mathbf{g}_i \\ &= -\sum_j \left(\frac{p_i}{d_i^2} + \frac{p_j}{d_j^2} \right) \frac{\partial W}{\partial r_{ij}} \mathbf{e}_{ij} + \sum_j \eta \left(\frac{1}{d_i^2} + \frac{1}{d_j^2} \right) \frac{\partial W}{\partial r_{ij}} \frac{\mathbf{v}_{ij}}{r_{ij}} + \mathbf{g}_i. \end{aligned} \tag{2.15}$$

$\mathbf{F}^C_{ij}$ results from pressure gradient and represents a conservative repulsive force acting along the unit vector $\mathbf{e}_{ij} = \mathbf{r}_{ij}/r_{ij} = (\mathbf{r}_i - \mathbf{r}_j)/\left|\mathbf{r}_{ij}\right|$ joining particles j to i. Pressure p of a particle is related to the density ρ of the particle according to the state equation, Eq. (1.5). Since it is a central force and symmetric by interchanging particle indices, total linear and angular momenta are exactly conserved.

$\mathbf{F}^D_{ij}$ comes from the fluid viscosity and represents an irreversible dissipative force, which reduces velocity differences between pair of particles. This force is symmetric by interchanging particle indices therefore it conserves linear momentum strictly. However it is non-central and acting alone the vector $\mathbf{v}_{ij} = \mathbf{v}_i - \mathbf{v}_j$, providing only approximate conservation of angular momentum [166]. If the conservation of angular momentum is crucial for certain applications, such as a rotating solid particle [183], another viscous formulation may be used

$$\mathbf{F}^D_{ij} = \xi\eta \left(\frac{1}{d_i^2} + \frac{1}{d_j^2} \right) \frac{\partial W}{\partial r_{ij}} \frac{\mathbf{e}_{ij} \cdot \mathbf{v}_{ij}}{r_{ij}} \mathbf{e}_{ij}, \tag{2.16}$$

where ξ is a calibrating parameter [182]. If the compact support $r_c/\Delta x$ is chosen sufficiently large, $\xi = D + 2$, where D is the dimension of the problem [182].

The third term describes an external body force $\mathbf{g}_i$, as for example the gravity.

Eqs. (2.15) and (2.16) represent a discretization of the deterministic hydrodynamic interactions of Newtonian fluid performed on Lagrangian elements.

2.2 Dissipative particle dynamics

Dissipative particle dynamics (DPD) method was invented two decades ago [164], to simulate hydrodynamic phenomena at mesoscale. DPD combines features from both molecular dynamics (MD) and lattice-gas automata (LGA), yet is faster than MD and more flexible than LGA. In a DPD method, the momentum equations are as follows

$$\dot{\mathbf{r}}_i = \mathbf{v}_i, \quad m_i\dot{\mathbf{v}}_i = \sum_j \mathbf{F}_{ij}^C + \sum_j \mathbf{F}_{ij}^D + \sum_j \mathbf{F}_{ij}^R, \tag{2.17}$$

where $\mathbf{F}_{ij}^C$ is referred as a conservative force from a described potential between particles i and j, and it is repulsive causing particles to be evenly distributed in space; $\mathbf{F}_{ij}^D$ is dissipative and depends linearly on the velocity difference and $\mathbf{F}_{ij}^R$ is a random force, which injects energy into the system and is independent of the momentum. The last two forces implement effectively a thermostat so that thermal equilibrium is achieved. The interactions of particles are within a finite compact support with cut off radius r_c. The typical forms of the three forces are given as follows [165, 184]

$$\mathbf{F}_{ij}^C = \alpha_{ij} W^C(r_{ij})\mathbf{e}_{ij}, \tag{2.18}$$
$$\mathbf{F}_{ij}^D = -\gamma W^D(r_{ij})(\mathbf{e}_{ij}\cdot\mathbf{v}_{ij})\mathbf{e}_{ij}, \tag{2.19}$$
$$\mathbf{F}_{ij}^R = \sigma W^R(r_{ij})\theta_{ij}\mathbf{e}_{ij}, \tag{2.20}$$

where α, γ, and σ reflect the strength of each force respectively; W^C, W^D, and W^R are weight functions of relative distance r_{ij}; θ is a *Gaussian white noise* ($\theta_{ij} = \theta_{ji}$) with

$$< \theta_{ij}(t) > = 0, \tag{2.21}$$
$$< \theta_{ij}(t)\theta_{kl}(t') > = (\delta_{ik}\delta_{jl} + \delta_{il}\delta_{jk})\,\delta(t-t'). \tag{2.22}$$

All three forces act along the line of centers $\mathbf{e}_{ij}$ and are symmetric by interchanging particle indices, therefore linear and angular momenta are strictly conserved.

The typical weighting function W^C for a soft repulsion is given by

$$W^C(r_{ij}) = \begin{cases} 1 - r_{ij}/r_c, & r_{ij} < r_c, \\ 0, & r_{ij} > r_c. \end{cases} \tag{2.23}$$

To satisfy the fluctuation-dissipation theorem (FDT) [13] in a DPD method, two conditions must be further enforced as follows [165]

$$W^D(r_{ij}) = \left[W^R(r_{ij})\right]^2, \tag{2.24}$$
$$2k_BT\gamma = \sigma^2, \tag{2.25}$$

where k_B is Boltzmann's constant and T is the absolute temperature. Therefore the weighting functions for dissipative and random forces are as follows

$$W^D(r_{ij}) = \left[W^R(r_{ij})\right]^2 = \begin{cases} (1 - r_{ij}/r_c)^2, & r_{ij} < r_c, \\ 0, & r_{ij} > r_c. \end{cases} \tag{2.26}$$

Extra care is taken into account for the random force, which becomes

$$\mathbf{F}_{ij}^{R} = \sigma W^{R}(r_{ij})\theta_{ij}\Delta t^{-1/2}\mathbf{e}_{ij}, \tag{2.27}$$

where θ_{ij} is a random number with zero mean and unit variance, chosen independently for each pair of interacting particles at each time step Δt; The appearance of $\Delta t^{-1/2}$ is derived by the integration of the underlying stochastic differential equations and interpreting $\mathbf{F}_{ij}^{R}$ as a *Wiener process* [184]. To integrate the dynamics of a DPD simulation, different integration schemes may be selected from Refs. [184, 185]. We prefer the simple Euler and velocity Verlet explicit schemes.

The link between the DPD equations with both the microscopic equations of the solvent molecules and the continuum hydrodynamic equations has been established. From one hand, Flekkøy and collaborators showed that by performing a systematic coarse-graining procedure starting from molecular dynamics, the set of equations for DPD on a Voronoi lattice [186, 187] can be obtained (*microscopic* $\rightarrow$ *mesoscopic*); on the other hand, with a standard technique of project operators, starting from the stochastic differential equations corresponding to the updating algorithm of DPD, Español has derived the continuum hydrodynamic equations [188] (*mesoscopic* $\rightarrow$ *macroscopic*).

The hydrodynamic interactions between fluid and solid structures can also be quantitatively captured within DPD simulations [189, 190, 191, 192]. Numerous works have been conducted on improving the boundary conditions in DPD methods [193, 194, 195, 32, 32, 196]. Some general criticism has been made on the computational cost of modeling colloidal particles, because each colloid is bigger than the fluid particle and needs hundreds of boundary particles to represent its geometry. To resolve this deficiency, efforts have been made by different research groups: one possibility is to represent each colloid with a single DPD particle, such as, Pryamitsyn and collaborators [197, 198], Karniadakis and co-workers [192, 199, 192], Whittle & Travis and their followers [200, 201]. However, a single-DPD-particle representation of a colloid restricts the shape of colloid to be spherical.

Despite the good performance of DPD in simulating complex systems, the method still suffers of some conceptual shortcomings. The price for the simplicity of DPD is related to the lack of direct connection between the model parameters and the physical parameters of the system one tries to simulate [202]. Usually, to specify the fluid transport coefficients of the corresponding coarse-grained hydrodynamic model, one needs to rely on kinetic theory [203] or map and calibrate the parameters in ways that are not always systematic [204, 205]. Perhaps, the most serious problem is the specification of the volume of a DPD particle and spatial scale at which a DPD simulation operates, posing some difficulties on the separate identification of resolution and finite-size effects in the output results [206, 207, 208, 209]. In particular, the latter problem is related to the non-unique definition of the hydrodynamic fluctuations acting on the fluid elements [202, 183].

2.3 Smoothed dissipative particle dynamics

It was soon after the invention of DPD that the similarity of DPD algorithms described in Eq. (2.17) to the SPH algorithms presented in Eq. (2.15) was already recognized by Español and collaborators [210, 211]. Yet one major difference relies on the thermal fluctuations being present only in the former method. By taking advantage of the similarity between SPH and DPD methods, Español and Revenga cast the SPH method in the GENERIC (general equation for the nonequilibrium reversible-irreversible coupling) framework [101, 102], and consistently introduced thermal fluctuations, to derive a new particle method. Similarly to SPH, the new method still allows for a direct specification of the transport coefficients, e.g., viscosity, compressibility, as input parameters, and further solves many previous drawbacks of DPD. Therefore it is named smoothed dissipative particle dynamics (SDPD) method [166].

The deterministic forces of SDPD, i.e., $\mathbf{F}_{ij}^C$ and $\mathbf{F}_{ij}^D$, are the same as in the SPH method. However, for each particular viscous force $\mathbf{F}_{ij}^D$, there exists an additional unique counterpart of random force $\mathbf{F}_{ij}^R$, causing thermal fluctuations of the momenta of particles i and j. For the specific from of $\mathbf{F}_{ij}^D$ defined in Eq. (2.15), $\mathbf{F}_{ij}^R$ reads

$$\mathbf{F}_{ij}^R = \left[-4k_B T\eta\left(\frac{1}{d_i^2}+\frac{1}{d_j^2}\right)\frac{1}{r_{ij}}\frac{\partial W}{\partial r_{ij}}\right]^{1/2} d\overline{\overline{\mathbf{W}}}_{ij}\cdot\mathbf{e}_{ij}, \tag{2.28}$$

where k_B is the Boltzmann constant and T is the absolute temperature; $d\overline{\overline{\mathbf{W}}}_{ij}$ is the traceless symmetric part of a matrix of independent increments of a Wiener process $d\mathbf{W}_{ij} = d\mathbf{W}_{ji}$, i.e., $d\overline{\overline{\mathbf{W}}}_{ij} = \left(d\mathbf{W}_{ij} + d\mathbf{W}_{ij}^T\right)/2 - tr[d\mathbf{W}_{ij}]\mathbf{I}/D$, where D is the spatial dimension [166, 182]. An intuitive view of the new method is as a consistent particle discretization of the continuum fluctuating hydrodynamic equations of Landau and Lifshitz [13].

One very interesting property of SDPD is related to the scaling of the thermal fluctuations with the fluid particle size [202]. It has been shown that the magnitude of $\mathbf{F}_{ij}^R$ increases as the inverse of the square root of the fluid particle volume, in agreement with classical results in statistical mechanics, namely, particle-velocity statistics satisfy the *Maxwell-Boltzmann distribution*, and their variance is given by

$$\left\langle v^2\right\rangle = D\frac{k_B T}{\rho_0 \mathcal{V}_i}, \tag{2.29}$$

where ρ_0 is the input equilibrium fluid density [202]. Thus, velocity fluctuations emerge naturally when the fluid description needs to be miniaturized, e.g., in microflow conditions, and increase in magnitude following the correct scaling as the spatial scales of the problem, i.e., the particle volumes $\mathcal{V}_i$, become smaller. This property is naturally embedded in the method and allows to prescribe the magnitude of fluctuations directly from physical inputs, without any fine-tuning.

The introduction of the term in Eq. (2.28) into the particle momentum equations allows for extending the applicability of the SPH method to micro/nano scales. Unlike

other mesoscopic methods, such as DPD, where finite-size/resolution effects are difficult to control [207, 208], the strict connection with SPH enables SDPD to perform numerical convergence studies in a Brownian environment by using established SPH error analysis[174, 22]. Furthermore, whenever the physical scale of the problem ranges in the macroscopic scale, it reduces to a version of SPH.

It is remarkable that the application of GENERIC together with a form of the dissipative terms taken from SPH allows for defining uniquely a size-dependent thermal noise, which satisfies the FDT [13]. Obeying FDT on the discrete level is not a trivial task, as shown in Ref. [99] for example, a simple central finite difference scheme for fluctuating hydrodynamics may introduce additional thermodynamic inconsistency.

The SDPD method has been recently applied to simulations of polymer molecules in suspension [212, 33], multiphase-fluid flows [182], particle dispersions [183], viscoelastic liquids [213], and passive microrheology [214]. Some group makes an effort of applying SDPD in a multiscale/multiresolution scenario [215].

In the following chapters, numerical modeling and simulations of SDPD in the area of colloidal and noncolloidal dispersions will be briefly described. Details in referred published work are included in the appendix.

3 Multiscale modeling of particle dispersions

This paper is published in the international peer-reviewed journal *Physics of Fluids* [183] with DOI: `http://dx.doi.org/10.1063/1.3676244`. The candidate writing this thesis is the first author.

Motivation: smoothed dissipative particle dynamics (SDPD) has been invented only recently [166] and it has not yet been applied to model complex fluids. In this paper, for the first time we apply SDPD to model and simulate within a simple framework the multiscale phenomena of colloidal and non-colloidal dispersions.

Algorithm: rigid structures of arbitrary shape embedded in the fluid are modeled by using frozen boundary particles on which artificial velocities are assigned to satisfy exactly the no-slip boundary condition on the solid-liquid interface. This boundary condition was originally proposed for a fixed set of two dimensional periodic solid cylinders [21] and I have extended it for solid walls and solid particles, which may be arbitrarily-shaped and can translate and rotate in both two and three dimensions. The dynamics of the suspended rigid structures is decoupled from the solvent by solving extra equations for the rigid body translation/rotation velocities derived from the total drag/torque exerted by the surrounding liquid. A crucial requirement highlighted in this paper is the need to use an angular-momentum-conservative formulation for the viscous force to model a rotating solid particle correctly. The rigid body motion needs to be calculated using a rotation matrix instead of integrating individual boundary particles, as the finite time step in simulations leads to artificial effects, such as non-preserving structure volume.

Software: by using a parallel particle-mesh library (PPM) [216], I have developed a software package using Fortran 90/95 [217] and named it as multiscale complex fluids simulation (MCF), in which I have implemented and verified all the algorithms proposed. Besides the general communications implemented in PPM, MCF also extends many other parallel functionalities, such as, calculation of forces, torques, and statistics for solid particles, solid wall boundaries, using message passing interface (MPI). MCF is stable and able to run up to $O(10^7)$ SDPD particles with a good scalability on $O(10^3)$ cores of the super computer (SuperMUC) located at the Leibniz-Rechenzentrum: `www.lrz.de`.

Simulation: **A)** The problem of fluid flowing through a fixed set of spherical solid particles in two and three dimensions was conducted first (steady flow through porous media). By changing the areas/volumes ratio of solid particles and fluid, I have evaluated the drag coefficients for different solid concentrations and results have been compared against the theory. **B)** Thereafter, the transient behavior of an impulsively started solid particle has been verified. **C)** The dynamics of a rotating solid particle has been correctly simulated by using a specific angular-momentum-conservative formulation. **D)** Using

finite resolutions, I have examined the limit, in which the hydrodynamic interactions between two solid particles are correctly captured. The result suggests that at very small inter-particle distance discretization of the continuum hydrodynamics fails and a pairwise lubrication correction force between solid particle needs to be introduced. **E)** Resolution effects for the translational and rotational diffusion of a Brownian spherical particle have been studied. Diffusion coefficients have shown numerical convergences: this is a remarkable result, as there has been so far no proper numerical convergence study done in a Brownian environment. **F)** Finally, a colloidal particle coupled with an external solid wall was studied and the anisotropic diffusion coefficients measured, both parallel and perpendicular to the wall. Results have been compared with analytical solutions [12] and experimental results [218], showing excellent agreement.

I have performed all the post-processing of data generated by **A)**—**E)** and co-advised a student, Rui Qian, who has used MCF for his master project on problem **F)**.

4 A splitting integration scheme

This paper is published in the international peer-reviewed journal *Computer Physics Communications* [219] with DOI: `http://dx.doi.org/10.1016/j.cpc.2013.08.015`. The candidate writing this thesis is the first author.

Motivation: the simulation of nearly contacting solid particles in suspension is a challenging task due to the diverging behavior of short-range lubrication forces, which pose a serious time-step limitation for explicit integration schemes. This general difficulty limits severely the total duration of simulations of concentrated suspension and needs to be solved in order to study the rheology of dense suspensions.

Algorithm: we propose a splitting integration scheme for the direct simulation of solid particles suspended in a Newtonian liquid. The scheme separates the contributions of different forces acting on the solid particles. In particular, intermediate- and long-range multi-body hydrodynamic forces, which are computed from the discretization of the Navier-Stokes equations using the smoothed particle hydrodynamics (SPH) method, and short-range repulsive forces are taken into account using an explicit integration; for short-range lubrication forces, velocities of pairwise interacting solid particles are updated implicitly by sweeping over all the neighboring pairs iteratively, until convergence in the solution is obtained. The criterion of choosing the number of sweeps N_{sweep} is dynamic by comparing results from a) 2^m and b) 2^{m+1} sweeps: N_{sweep} is halved or doubled, depending on whether the dimensionless L_2 norm of the difference between solutions a) and b) is smaller or bigger than a pre-defined tolerance ϵ. Conceptually the proposed scheme is not limited to the SPH method presented here, but can be easily applied to other simulation techniques employed for particulate suspensions.

Software: I have used a free algebra software named *Maxima* to obtain the analytical solution of the implicit equations derived from pairwise lubrication force (`http://maxima.sourceforge.net`). The resulted expressions together with other parts of the splitting schemes have been implemented using Fortran 90/95 [217] in the multiscale complex fluids (MCF) simulation software package.

Simulation: By using the splitting integration, we start with a problem of two solid particles approaching each other under a linear shear flow. Analytical solutions are available for this problem. Our simulation can capture correctly both open and closed trajectories of the two particles. Afterward, we simulate multiple particles in suspension and demonstrate the relation between N_{sweep} and ϵ. By comparing the overall suspension viscosity using different ϵ, we find the optimal criterion ($\epsilon = 10^{-3}$) for obtaining converged results at reasonable computational costs. Simulation results with the splitting integration scheme for solid concentrations of $\phi = 0$ — 58.9% agree very well with results obtained by using purely explicit integration. Concentration $\phi = 68.7\%$ can not be simulated using an explicit integration with a reasonable cost, whereas the splitting

integration runs efficiently and stably. All the results of viscosity are compared against empirical formula from literature. Besides the suspension viscosity, we also compare the microstructure of solid particles from our simulations, including radial distribution function and solid concentration profiles near the wall, with cited references with very good agreement whereas preserving the accuracy, the benefit of the new method can be quantified as a speedup of up to 10 over standard explicit integrations.

5 Hydrodynamic shear thickening under confinement

This paper is accepted to the international peer-reviewed *Journal of Non-Newtonian Fluid Mechanics* [220]. The candidate writing this thesis is the first author.

Motivation: the property of shear thickening of concentrated particle dispersions, i.e., a monotonic increase of viscosity at elevated shear rates, is ubiquitous [6]. For one hand, it is a challenging problem for pumping, coating and spraying operations [6], and on the other hand, it opens up a series of new applications, such as, energy absorber [221] and universal robotic gripper [222]. However, the physical mechanism for shear thickening is still under debate. Effects of hydrodynamic clusters (hydroclusters) and confinements are two popular hypotheses, but their interplay is poorly understood. As one particular application of our numerical modeling proposed in previous two papers, we study the two effects together in this work.

Algorithm: the suspension of two-dimensional discoidal particles is confined by walls orthogonal to the shear gradient direction and undergoes a Couette flow. The many-body hydrodynamic interactions (HIs) are modeled by the smoothed particle hydrodynamics (SPH) method. To recover the HIs accurately at short distances, a pairwise lubrication force is introduced between solid particles. To model surface roughness and exclude volume effects, a very stiff pairwise repulsive force is considered between solid particles at short ranges.

Software: the SPH modeling of non-Brownian solid particles and walls, and the short range forces have been implemented in the MCF software package by the author.

Simulation: all simulations run on both a 8-core workstation (Intel Xeon CPU E5410@2.33 GHz) and a super computer located within Leibniz-Rechenzentrum (`www.lrz.de`). A large set of relevant parameters has been studied, which includes solid concentration $\phi \in [0, 58.9\%]$; nine orders of magnitude for the non-dimensional shear rate/stress; channel height to particle radius ratio from 8 to 256.

With assistance of Mr. Sergey Litvinov, we perform post-processing of a large set of generated data. After analyzing the results, we find that (i) hydrodynamic shear thickening exists for all the dense suspensions studied, i.e., $\phi \in [39.3\%, 58.9\%]$. Accompanying the shear thickening, there are always hydroclusters, defined as density fluctuations of solid particles. The shear thickening observed is continuous and reversible upon flow cessation. (ii) Confinement plays a geometrical role by reducing the maximum packing fraction and enhancing HIs, therefore, it increases viscosities at both Newtonian and shear-thickened states. (iii) Nevertheless, if we measure relative excessive viscosity compared to the Newtonian value, the strength of shear thickening is uniquely determined by the probability distribution of hydroclusters. (iv) Under strong confinement the perco-

lating network of hydroclusters develops into a jamming structure at high shear rate and as a result, the viscosity increases substantially. (v) Extrapolating the viscosity to the limit of very weak confinement shows that confinement is important for non-negligible hydrodynamic shear thickening.

Further implication of the paper is that continuous shear thickening (CST) and discontinuous shear thickening (DST) [223, 224, 225, 226] should be clearly distinguished. The former is associated with hydroclusters and observed in our simulations, while the latter is not seen. It is very likely that additional frictional forces play an important role for DST. Facilitated by the strong HIs and frictional forces, wall confined dense suspension may lead to DST [60].

Bibliography

[1] R. G. Jones, E. S. Wilks, W. V. Metanomski, J. Kahovec, M. Hess, R. Stepto, and T. Kitayama, editors. *Compendium of polymer terminology and nomenclature*. RSC Publishing, Cambridge, 2009.

[2] R. G. Gilbert, M. Hess, A. D. Jenkins, R. B. Jones, P. Kratochvíl, and R. F. T. Stepto. Dispersity in polymer science. *Pure Appl. Chem.*, 81(2):351–353, 2009.

[3] S. Slomkowski, J. V. Alemán, R. G. Gilbert, M. Hess, K. Horie, R. B. Jones, P. Kubisa, I. Meisel, W. Mormann, S. Penczek, and R. F. T. Stepto. Terminology of polymer and polymerization processes in dispersed systems. *Pure Appl. Chem.*, 83(12):2229–2259, 2011.

[4] W. B. Russel, D. A. Saville, and W. R. Schowalter. *Colloidal dispersions*. Cambridge monographs on mechanics. Cambridge University Press, Cambridge, 1989.

[5] R. G. Larson. *The structure and rheology of complex fluids*. Oxford University Press, New York, 1999.

[6] J. Mewis and N. J. Wagner. *Colloidal suspension rheology*. Cambridge University Press, Cambridge, 2012.

[7] T. W. F. Russel, A. S. Robinson, and N. J. Wagner. *Mass and heat transfer: analysis of mass contactors and heat exchangers*. Cambridge University Press, New York, 2008.

[8] G. E. Karniadakis, A. Beskok, and N. Aluru. *Microflows and nanoflows: fundamentals and simulation*. Springer, New York, 2005.

[9] D. A. Fedosov, W. Pan, G. Gompper, and G. E. Karniadakis. Predicting human blood viscosity in silico. *Proc. Natl. Acad. Sci. USA*, 108:11772–11777, 2011.

[10] J. Mewis and N. J. Wagner. Current trends in suspension rheology. *J. Non-Newton. Fluid*, 157:147–150, 2009.

[11] G. K. Batchelor. *An introduction to fluid dynamics*. Cambridge University Press, Cambridge, 1967.

[12] J. Happel and H. Brenner. *Low Reynolds number hydrodynamics: with special applications to particulate media*. Martinus Nijhoff Publishers, The Hague, 1983.

[13] L. D. Landau and E. M. Lifshitz. *Fluid mechanics*. Volume 6 of course of theoretical physics. Pergamon Press, Oxford, second edition, 1987.

[14] S. Kim and S. J. Karrila. *Microhydrodynamics: principles and selected applications*. Butterworth-Heinemann, Boston, 1991.

[15] J. J. Monaghan. Simulating free surface flows with SPH. *J. Comput. Phys.*, 110:399–406, 1994.

[16] M. Ellero, M. Serrano, and P. Español. Incompressible smoothed particle hydrodynamics. *J. Comput. Phys.*, 226:1731–1752, 2007.

[17] X. Y. Hu and N. A. Adams. A incompressible multi-phase SPH method. *J. Comput. Phys.*, 227:264–278, 2007.

[18] X. Y. Hu and N. A. Adams. A constant-density approach for incompressible multiphase SPH. *J. Comput. Phys.*, 228:2082–2091, 2009.

[19] R. Courant, K. Friedrichs, and H. Lewy. Über did partiellen Differenzengleichungen der mathematicshcen Physik. *Math. Ann.*, 100:32–74, 1928.

[20] R. Courant, K. Friedrichs, and H. Lewy. On the partial difference equations of mathematical physics. *IBM J.*, pages 215–234, 1967.

[21] J. P. Morris, P. J. Fox, and Y. Zhu. Modeling low Reynolds number incompressible flows using SPH. *J. Comput. Phys.*, 136(1):214 – 226, 1997.

[22] M. Ellero and N. .A. Adams. SPH simulations of flow around a periodic array of cylinders confined in a channel. *Int. J. Numer. Meth. Eng.*, 86(8):1027–1040, 2011.

[23] F. M. White. *Fluid mechanics*. McGraw-Hill, New York, 2001.

[24] D. A. Fedosov, H. Lei, B. Caswell, S. Suresh, and G. E. Karniadakis. Multiscale modeling of red blood cell mechanics and blood fluid in malaria. *PLoS Comput. Biol.*, 7:e1002270, 2011.

[25] M. A. Day. The no-slip conditions of fluid mechanics. *Erkenntnis*, 33:285–296, 1990.

[26] J. W. Swan and A. S. Khair. On the hydrodynamics of 'slip-stick' spheres. *J. Fluid Mech.*, 606:115–132, 2008.

[27] A. Einstein. Über die von der molekularkinetischen Theorie der Wärme geforderte Bewegung von in ruhenden Flüssigkeiten suspendierten Teilchen. *Annalen der Physik*, 322(8):549–560, 1905.

[28] M. von Smoluchowski. Zur kinetischen Theorie der Brownschen Molekularbewegung und der Suspensionen. *Annalen der Physik*, 21(14):756–780, 1906.

[29] A. Einstein. Eine neue bestimmung der molekueldimensionen. *Annalen der Physik*, pages 289–306, 1906.

[30] W. Sutherland. A dynamic theory of diffusion for non-electrolytes and the molecular mass of albumin. *Phil. Mag. 6*, 9(54):781–785, 1905.

[31] J. Perrin. Mouvement brownien et réalité moléculaire. *Ann. Chim. Phys.*, 18:1–144, 1909.

[32] I. V. Pivkin and G. E. Karniadakis. Controlling density fluctuations in wall-bounded dissipative particle dynamics systems. *Phys. Rev. Lett.*, 96:206001, 2006.

[33] S. Litvinov, M. Ellero, X. Y. Hu, and N. A. Adams. A splitting scheme for highly dissipative smoothed particle dynamics. *J. Comput. Phys.*, 229(15):5457–5464, AUG 1 2010.

[34] J. T. Padding and A. A. Louis. Hydrodynamic interactions and Brownian forces in colloidal suspensions: Coarse-graining over time and length scales. *Phy. Rev. E*, 74(3):031402, September 2006.

[35] N. J. Wagner and J. F. Brady. Shear thickening in colloidal dispersions. *Phys. Today*, 62(10):27–32, Oct. 2009.

[36] C. L. Darabaner, J. K. Raasch, and S. G. Mason. Particle motions in sheard suspensions xx: circular cylinders. *Can. J. Chem. Eng.*, 45:3–12, 1967.

[37] C. L. Darabaner, J. K. Raasch, and S. G. Mason. Particle motions in sheared suspensions xx: Circular cylinders (errata). *Can. J. Chem. Eng.*, 45:120, 1967.

[38] S. Wakiya, C. L. Darabaner, and S. G. Mason. Particle motions in sheared suspensions xxi: Interactions of rigid spheres (theoretical). *Rheo. Acta.*, 6:264–273, 1967.

[39] G. I. Batchelor and J. T. Green. The hydrodynamic interaction of two small freely-moving spheres in a linear flow field. *J. Fluid Mech.*, 56:375–400, 1972.

[40] G. K. Batchelor. The stress system in a suspension of force-free particles. *J. Fluid Mech.*, 41:545–570, 1970.

[41] G. K. Batchelor. Sedimentation in a dilute dispersion of spheres. *J. Fluid Mech.*, 52:245–268, 1972.

[42] G. K. Batchelor. Brownian diffusion of particles with hydrodynamic interaction. *J. Fluid Mech.*, 74:1–29, 1976.

[43] G. K. Batchelor. The effect of brownian motion on the bulk stress in a suspension of spherical particles. *J. Fluid Mech.*, 83:97–117, 1977.

[44] R. J. Hunter. *Zeta potential in colloid science*. Academic Press Inc., London, 1981.

[45] J. K. G. Dhont. *An introduction to dynamics of colloids*. Studies in interface science. Elsevier, Amsterdam, 1996.

[46] P. C. Hiemenz and R. Rajagopalan. *Principles of colloid and surface chemistry*. Marcel Dekker Inc., New York, 3rd edition, 1997.

[47] H. Helmholtz. Über einige Gesetze der Vertheilung electrischer Ströme in Körperlichen Leitern mit Anwendung auf die thierischelektrischen-Versuche. *Pogg. Ann.*, LXXXIX:211, 1853.

[48] G. Gouy. Sur la constitution de la charge électrique ã la surface d'un électrolyte. *J. Phys. Radium*, 9:457–468, 1910.

[49] D. L. Chapman. A contribution to the theory of electroencapillarity. *Phil. Mag.*, 25(6):475–481, 1913.

[50] K. Takamura, H. L. Goldsmith, and S. G Mason. The microrheology of colloidal dispersions xii. trajectories of orthokinetic pair-collisions of latex spheres in a simple electrolyte. *J. Colloid Interface Sci.*, 82(1):175–189, 1981.

[51] K. Takamura, H. L. Goldsmith, and S. G Mason. The microrheology of colloidal dispersions xiii. trajectories of orthokinetic pair-collisions of latex spheres in a cationic polyelectrolyte. *J. Colloid Interface Sci.*, 82(1):190–202, 1981.

[52] G. Bossis and J. F. Brady. Dynamic simulation of sheared suspensions. i. general method. *J. Chem. Phys.*, 80(10):5141–5154, May 1984.

[53] D. I. Dratler and W. R. Schowalter. Dynamic simulation of suspensions of non-Brownian hard spheres. *J. Fluid Mech.*, 325:53–77, 1996.

[54] R. C. Ball and J. R. Melrose. Lubrication breakdown in hydrodynamic simulations of concentrated colloids. *Adv. Colloid Interface Sci.*, 59:19–30, 1995.

[55] J. R. Melrose and R. C. Ball. The pathological behavior of sheared hard spheres with hydrodynamic interactions. *Europhys. Lett.*, 32(6):535–540, 1995.

[56] E. G. Verwey and J. T. G. Overbeek. *Theory of the stability of lyophobic colloids*. Elsevier, Amsterdam, 1948.

[57] R. H. Davis. Effects of surface roughess on a sphere sedimenting through a dilute suspension of neutrally buoyant spheres. *Phys. Fluids A*, 4:2607–2619, 1992.

[58] H. J. Wilson and R. H. Davis. The viscosity of a dilute suspension of rough spheres. *J. Fluid. Mech.*, 421:339–367, 2000.

[59] S. Luding. Cohesive, friction powders: contact model for tension. *Granular Matter*, 10:235–246, 2008.

[60] Ryohei Seto, Romain Mari, Jeffrey F. Morris, and Morton M. Denn. Discontinuous shear thickening of frictional hard-sphere suspensions. *Phys. Rev. Lett.*, 111:218301, Nov 2013.

[61] G. K. Batchelor and J. T. Green. The determination of the bulk stress in a suspension of spherical particles to order c^2. *J. Fluid Mech.*, 56:401–427, 1972.

[62] J. F. Brady and G. Bossis. Stokesian dynamics. *Ann. Rev. Fluid Mech.*, 20:111–157, 1988.

[63] P. Tabeling. *Introduction to microfluidics*. Oxford University Press, Oxford, 2nd edition, 2005.

[64] M. J. Pugia, G Blankenstein, R. P. Peters, J. A. Profitt, K. Kadel, T. Willms, R. Sommer, H. H. Kuo, and L. S. Schulman. Microfluidic tool box as technology platform for hand-held diagnostics. *Clin. Chem.*, 51:1923–1932, 2005.

[65] M. Whittle and E. Dickinson. Note on simulating colloids by disspative particle dynamics: issues and complications. *J. Colloid Interface Sci.*, 242:106–109, 2001.

[66] P. Koumoutsakos. Multiscale flow simulations using particles. *Annu. Rev. Fluid Mech.*, 37:457–487, 2005.

[67] R. G. M. van der Sman. Simulations of confined suspension flow at multiple length scales. *Soft Matter*, 5:4376–4387, 2009.

[68] M. Fujita and Y. Yamaguchi. Mesoscale modeling for self-organization of colloidal systems. *Curr. Opin. Colloid Interface Sci.*, 15(1), 2010.

[69] P. Español, M Serrano, and H. C. Öttinger. Thermodynamically admissible form for discrete hydrodynamics. *Phys. Rev. Lett.*, 83(22):4542–4545, 1999.

[70] M. Griebel, T. Dornseifer, and T. Neunhoeffer. *Numerical simulation in fluid dynamics: A practical introduction*. SIAM, 1998.

[71] J. D. Anderson, J. Degroote, G. Degrez, E. Dick, R. Grundmann, and J. Vierendeels. *Computational fluid dynamics: an introduction*. Springer-Verlag, Berlin, 3rd edition, 2008.

[72] G. E. Karniadakis and S. J. Sherwin. *Sepctral/hp element methods for computational fluid dynamics*. Numerical mathematics and scientific computation. Oxford University Press, New York, 2nd edition, 2005.

[73] J. T. Katsikadelis. *Boundary element: theory and applications*. Elsevier, London, 2002.

[74] C. S. Peskin. Numerical analysis fo blood flows in the heart. *J. Comput. Phys.*, 25:220–252, 1977.

[75] C. S. Peskin. The immersed boundary method. *Acta Numer.*, pages 479–517, 2002.

[76] R. Mittal and G. Iaccarino. Immersed boundary methods. *Annu. Rev. Fluid Mech.*, 37:239–261, 2005.

[77] C. W. Hirt and B. D. Nichols. Volume of fluid (VOF) method for the dynamics of free boundaries. *J. Comput. Phys.*, 39(1):201–225, 1981.

[78] S. O. Unverdi and G. Tryggvason. A front-tracking method for viscous, incompressible, multi-fluid flows. *J. Comput. Phys.*, 100(1):25–37, 1992.

[79] G. Tryggvason, R. Bunner, A. Esmaeeli, D. Juric, N. Al-Rawahi, W. Tauber, J. Han, S. Nas, and Y.-J. Jan. A front-tracking method for the computation of multiphase flow. *J. Comput. Phys.*, 169(2):708–759, 2001.

[80] S. Osher and J. A. Sethian. Fronts propagating with curvature-dependent speed: algorithms based on Hamilton-Jacobi formulations. *J. Comput. Phys.*, 79(1):12–49, 1988.

[81] R. Yamamoto, Y. Nakayama, and K. Kim. A smooth interface method for simulating liquid crystal colloid dispersions. *J. Phys.: Condes. Matter*, 16:S9145–S1955, 2004.

[82] Y. Nakayama and R. Yamamoto. Simulation method to resolve hydrodynamic interactions in colloidal dispersions. *Phys. Rev. E*, 71:036707, 2005.

[83] Y. Nakayama, K. Kim, and R. Yamamoto. Simulating (electro)hydrodynamic effects in colloidal dispersions: smoothed profile method. *Eur. Phys. J. E*, 26:361–368, 2008.

[84] X. Luo, M. Maxey, and G. E. Karniadakis. Smoothed profile method for particulate flows: error analysis and simulations. *J. Comput. Phys.*, 228:1750–1769, 2009.

[85] R. Glowinski, T.-W. Pan, T. I. Hesla, and D. D. Joseph. A distributed Lagrange multiplier fictitious domain method for particulate flows. *Int. J. Multiphase Flow*, 25(5):755–794, Aug. 1999.

[86] N. A. Patankar, Singh. P., D. D. Joseph, R. Glowinski, and T.-W. Pan. A new formulation for the distributed Lagrange multiplier/fictious domain method for particulate flows. *Int. J. Multiphase Flow*, 26:1509–1524, 2000.

[87] H. Tanaka and T. Araki. Simulation method of colloidal suspensions with hydrodynamic interactions: fluid particle dynamics. *Phys. Rev. Lett.*, 85:1338–41, 2000.

[88] A. Furukawa and H. Tanaka. Key role of hydrodynamic interactions in colloidal gelation. *Phy. Rev. Lett.*, 104:245702, 2010.

[89] M. R. Maxey and B. K. Patel. Local force representation for particles sedimenting in Stokes flow. *Int. J. Multiphase Flow*, 27:1603–1626, 2001.

[90] S. L. Dance and M. R. Maxey. Incorporation of lubrication effects into the force-coupling method for particulate two-phase flow. *J. Comput. Phys.*, 189:212–238, 2003.

[91] S. L. Dance and M. R. Maxey. Particle density stratification in transit sedimentation. *Phy. Rev. E*, 68:031403, 2003.

[92] S. Lomholt and M. R. Maxey. Force-coupling method for particulate two-phase flow: Stokes flow. *J. Comput. Phys.*, 184:381–405, 2003.

[93] K. Yeo and M. R. Maxey. Simulation of concentrated suspensions using the force-coupling method. *J. Comput. Phys.*, 229:2401–2421, 2010.

[94] K. Yeo and M. R. Maxey. Dynamics of concentrated suspensions of non-colloidal particles in Couette flow. *J. Fluid Mech.*, 649:205–231, 2010.

[95] K. Yeo and M. R. Maxey. Ordering transition of non-Brownian suspensions in confined steady shear flow. *Phys. Rev. E*, 81:051502, 2010.

[96] K. Yeo and M. R. Maxey. Rheology and ordering transitions of non-brownian suspensions in a confined shear flow: Effects of external torques. *Phy. Rev. E*, 81:062501, 2010.

[97] K. Yeo and M. R. Maxey. Anomalous diffusion of wall-bounded non-colloidal suspensions in a steady shear flow. *Europhys. Lett.*, 92(2), OCT 2010.

[98] D. Liu, E. Keaveny, M. R. Maxey, and G. E. Karniadakis. Force-coupling method for flows with ellipsoidal particles. *J. Comput. Phys.*, 228:3559–3581, 2009.

[99] M. Serrano and P. Español. Thermodynamically consistent mescopic fluid particle model. *Phy. Rev. E*, 64:046115, 2001.

[100] N. Sharma and N. A. Patankar. Direct numerical simulation of the Brownian motion of particles by using fluctuating hydrodynamic equations. *J. Comput. Phys.*, 201:466–486, 2004.

[101] M. Grmela and H. C. Öttinger. Dynamics and thermodynamics of complex fluids. i. development of a general formalism. *Phys. Rev. E*, 56:6620–6632, 1997.

[102] H. C. Öttinger and M. Grmela. Dynamics and thermodynamics of complex fluids. II. illustrations of a general formalism. *Phy. Rev. E*, 56:6633–6655, 1997.

[103] M. Serrano, G. D. Fabritiis, P. Español, E. G. Flekkøy, and P. Coveney. Mesoscopic dynamics of Voronoi fluid particles. *J. Phys. A: Math. Gen.*, 35:1605–1625, 2002.

[104] N. Sharma and N. A. Patankar. A fast compuationa technique for the direct numerical simulation of rigid particulate flows. *J. Comput. Phys.*, 205:439–457, 2005.

[105] G. A. Bird. Approach to translational equilibrium in a rigid sphere gas. *Phys. Fluids*, 6:1518, 1963.

[106] G. A. Bird. Monte carlo simultion of gas flows. *Annu. Rev. Fluid Mech.*, 10:11–31, 1978.

[107] G. A. Bird. *Molecular gas dynamics and the direct simulation of gas flows*. Clarendon Press, Oxford, 1994.

[108] A. Malevanets and R. Kapral. Mesoscopic model for solvent dynamics. *J. Chem. Phys.*, 110(17):8605–8613, 1999.

[109] T. Ihle and D. M. Kroll. Stochastic rotation dynamics: A Galilean-invariant mesoscopic model for fluid flow. *Phys. Rev. E.*, 63:020201, 2001.

[110] T. Ihle and D. M. Kroll. Stochastic rotation dynamics. i. formulism, Galilean invariance, and Green-Kubo relations. *Phy. Rev. E*, 67:066705, 2003.

[111] T. Ihle and D. M. Kroll. Stochastic rotation dynamics. ii. transport coefficients, numerics, and long-time tails. *Phy. Rev. E*, 67:066706, 2003.

[112] A. Malevanets and R. Kapral. Solute molecular dynamics in a mesoscale solvent. *J. Chem. Phys.*, 112:7260–7269, 2000.

[113] A. Malevanets and J. M. Yeomans. Dynamics of short polymer chains in solution. *Europhys. Lett.*, 52:231–237, 2000.

[114] A. Lamura, G. Gompper, T. Ihle, and D. M. Kroll. Multi-particle collision dynamics: flow around a circular and a square cylinder. *Europhys. Lett.*, 56(3):319–325, 2001.

[115] U. Frisch, B. Hasslacher, and Y. Pomeau. Lattice-gas automata for the Navier-Stokes equation. *Phy. Rev. Lett.*, 56(14):1505–1508, 1986.

[116] A. J. C. Ladd. Short-time motion of colloidal particles: numerical simulation via a fluctuating lattice-Boltzmann equation. *Phy. Rev. Lett.*, 70(9):1139–1142, 1993.

[117] A. J. C. Ladd. Numerical simulations of particulate suspensions via a discretized Boltzmann equation. part 1. theoretical foundation. *J. Fluid Mech.*, 271:285–309, 1994.

[118] A. J. C. Ladd. Numerical simulations of particulate suspensions via a discretized Boltzmann equation. part 2. numerical results. *J. Fluid Mech.*, 271:311–339, 1994.

[119] S. Chen and G. D. Doolen. Lattice Boltzmann method for fluid flows. *Ann. Rev. Fluid Mech.*, 30:329–364, 1998.

[120] A. J. C. Ladd and R. Verberg. Lattice-Boltzmann simulations of particle-fluid suspensions. *J. Stat. Phys.*, 104(5-6):1191–1251, 2001.

[121] S. Succi. *The lattice Boltzmann equation: for fluid dynamics and beyond*. Numerical mathematics and scientific computations. Oxford University Press, Oxford, 2001.

[122] N. Q. Nguyen and A. J. C. Ladd. Lubrication corrections for lattice-Boltzmann simulations of particle suspensions. *Phys. Rev. E*, 66(046708), 2002.

[123] P. L. Bhatnagar, E. P. Gross, and M. Krook. A model for collision processes in gases. i. small amplitude processes in charged and neutral one-component systems. *Phy. Rev.*, 94:511–525, 1954.

[124] G. McNamara, A. L. Garcia, and B. J. Alder. A hydrodynamically correct thermal lattice Boltzmann model. *J. Stat. Phys.*, 87:1111–1121, 1997.

[125] X. Shan. Simulation of Reylaigh-Bénard convection using lattice Boltzmann method. *Phy. Rev. E*, 55(3):2780–2788, 1997.

[126] X. He, S. Chen, and G. D. Doolen. A novel thermal model for the lattice Boltzmann method in incompressible limit. *J. Comput. Phys.*, 146:282–300, 1998.

[127] D. L. Koch and A. J. C. Ladd. Moderate Reynolds number flows through periodic and random arrays of alingned cylinders. *J. Fluid Mech.*, 349:31–66, 1997.

[128] M. A. Van Der Hoef, R. Beetstra, and J. A. M. Kuipers. Lattice-Boltzmann simulations of low-Reynolds-number flow past mono-and bidisperse arrays of spheres: results for the permeability and drag force. *J. Fluid Mech.*, 528:233–254, 2005.

[129] C. Pan, L. Luo, and C. T. Miller. An evaluation of lattice Boltzmann sscheme for porous medium flow simulation. *Comput. Fluids*, 35:898–909, 2006.

[130] R. S. Maier and R. S. Bernard. Lattice-Boltzmann accuracy in pore-scale flow simulation. *J. Comput. Phys.*, 229:233–255, 2010.

[131] B. J. Alder and T. E. Wainwright. Studies in molecular dynamics. i. general method. *The Journal of Chemical Physics*, 31(2):459–466, 1959.

[132] M. P. Allen and D. J. Tildesley. *Computer simulation of liquids*. Clarendon Press, Oxford, Oct. 1989.

[133] D. E. Shaw, M. M. Deneroff, R. O Dror, J. S. Kuskin, R. H. Larson, J. K. Salmon, C. Young, B. Batson, K. J. Bowers, J. C.. Chao, M.l P. Eastwood,

J. Gagliardo, J. P. G., C. R. Ho, D. J. Ierardi, I. Kolossvary, J. L.. Klepeis, T. Layman, C. Mcleavey, M. A. Moraes, R. Mueller, E. C. Priest, Y. Shan, J. Spengler, M. Theobald, B. Towles, and S. C. Wang. Anton, a special-purpose machine for molecular dynamics simulation. *Commun. of the ACM*, 51(7):91–97, 2008.

[134] K. Lindorff-Larsen, S. Piana, R. O. Dror, and D. E. Shaw. How fast-folding proteins fold. *Science*, 334:517–520, 2011.

[135] D. L. Ermak. A computer simulation of charged particles in solution. i. technique and equilibrium properties. *J. Chem. Phys.*, 62:4189–4196, 1975.

[136] T. Schlick. *Molecular modeling and simulation: an interdisciplinary guide*. Interdisciplinary applied mathematics. Springer-Verlag, New York, 2002.

[137] D. L. Ermak and J. A. McCammon. Brownian dynamics with hydrodynamic interactions. *J. Chem. Phys.*, 69:1352–1360, 1978.

[138] G. Bossis and J. F. Brady. Self-diffusion of Brownian particles in concentrated suspensions under shear. *J. Chem. Phys.*, 87(9):5437–5448, 1987.

[139] R. A. Bagnold. Experiments on a gravity-free dispersion of large solid spheres in a Newtonian fluid under shear. *Proc. R. Soc. A*, 225(1160):49–63, 1954.

[140] D. J. Jeffrey and Y. Onishi. Calculation of the resistance and mobility functions for two unequal rigid spheres in low-reynolds-number flow. *J. Fluid Mech.*, 139:261–290, 1984.

[141] J. F. Brady and G. Bossis. The rheology of concentrated suspensions of spheres in simple shear flow by numerical simulation. *J. Fluid Mech.*, 155:105–129, 1985.

[142] G. Bossis and J. F. Brady. The rheology of Brownian suspension. *J. Chem. Phys.*, 91(3):1866–1874, 1989.

[143] L. J. Durlofsky and J. F. Brady. Dynamic simulation of bounded suspensions of hydrodynamically interacting particles. *J. Fluid Mech.*, 200:39–67, 1989.

[144] J. F. Morris and J. F. Brady. Self-diffusion in sheared suspensions. *J. Fluid Mech.*, 312:223–252, 1996.

[145] T. N. Phung, J. F. Brady, and G. Bossis. Stokesian dynamics simulation of Brownian suspensions. *J. Fluid Mech.*, 313:181–207, 1996.

[146] J. F. Brady and J. F. Morris. Microstructure of strongly sheared suspensions and its impact on rheology and diffusion. *J. Fluid Mech.*, 348:103–139, 1997.

[147] D. R. Foss and J. F. Brady. Structure, diffusion and rheology of Brownian suspensions by Stokesian dynamics simulation. *J. Fluid Mech.*, 407:167–2000, 2000.

[148] A. Sierou and J. F. Brady. Rheology and microstructure in concentrated noncolloidal suspensions. *J. Rheol.*, 46(5):1031–1056, 2002.

[149] A. Sierou and J. F. Brady. Shear-induced self-diffusion in non-colloidal suspensions. *J. Fluid Mech.*, 506:285–314, 2004.

[150] A. Sierou and J. F. Brady. Accelerated Stokesian dynamics simulations. *J. Fluid Mech.*, 448:115–146, 2001.

[151] A. J. Banchio and J. F. Brady. Accelerated Stokesian dynamics: Brownian motion. *J. Chem. Phys.*, 118(22):10323–10332, 2003.

[152] P. M. Kulkarni and J. F. Morris. Suspension properties at finite Reynolds number from simulated shear flow. *Phys. Fluids*, 20:040602, 2008.

[153] F. B. Usabiaga, J. B. Bell, R. Delgado-Buscalioni, A. Donev, T. G. Fai, B. E. Griffith, and C. S. Peskin. Staggered schemes for fluctuating hydrodynamics. *Multiscale Model. Simul.*, 10:1369–1408, 2012.

[154] F. B. Usabiaga, I. Pagonabarraga, and R. Delgado-Buscalioni. Inertial coupling for point particle hydrodynamics. *J. Comput. Phys.*, 235:701–722, 2013.

[155] J. W. Swan and J. F. Brady. Simulation of hydrodynamically interacting particles near a no-slip boundary. *Phys. Fluids*, 19:113306, Nov. 2007.

[156] R. Kutteh. Rigid body dynamics approach to Stokesian dynamics simulations of nonspherical particels. *J. Chem. Phys.*, 132:174107, 2010.

[157] P. R. Nott and J. F. Brady. Pressure-driven flow of suspensions: simulation and theorey. *J. Fluid Mech.*, 275:157–199, 1994.

[158] A. Singh and P. Nott. Normal stresses and microstructure in bonded sheared suspensions via Stokesian dynamics simulations. *J. Fluid. Mech.*, 412:279–301, 2000.

[159] J. W. Swan and J. F. Brady. Particle motion between parallel walls: hydrodynamics and simulation. *Phys. Fluids*, 22:103301, Oct. 2010.

[160] J. W. Swan and J. F. Brady. Hydrodynamics of confined dispersions. *J. Fluid Mech.*, 687:254–299, 2011.

[161] S. Weinbaum and P. Ganatos. Numerical multipole and boundary integral equation technique in Stokes flow. *Ann. Rev. Fluid Mech.*, 22:275–316, 1990.

[162] R. A. Gingold and J. J. Monaghan. Smoothed particle hydrodynamics: theory and application to non-spherical stars. *Mon. Not. R. Astron. Soc.*, 181:375–389, 1977.

[163] L. B. Lucy. A numerical approach to the testing of the fission hypothesis. *Astron. J.*, 82:1013–1024, 1977.

[164] P. J. Hoogerbrugge and J. M. V. A. Koelman. Simulating microsopic hydrodynamics phenomena with dissipative particle dynamics. *Europhys. Lett.*, 19(3):155–160, 1992.

[165] P. Español and P. Warren. Statistical mechanics of dissipative particle dynamics. *Europhys. Lett.*, 30(4):191–196, May 1995.

[166] P. Español and M. Revenga. Smoothed dissipative particle dynamics. *Phys. Rev. E*, 67(2):026705, 2003.

[167] S. Koshizuka and Y Oka. Moving particle semi-implicit method for fragmentation of incompressible fluid. *Nuclear Sci. Eng.*, 123, 1996.

[168] S. Koshizuka, A. Nobe, and Y. Oka. Numerical analysis of breaking waves using the moving particle semi-implicit method. *Int. J. Numer. Meth. Fluids*, 26, 1998.

[169] G.-H. Cottet and P. D. Koumoutsakos. *Vortex methods: theory and practice.* Cambridge University Press, Cambridge, 2000.

[170] W. R. Hwang, M. A. Hulsen, and H. E. H. Meijer. Direct simulation of particle suspensions in sliding bi-periodic frames. *J. Comput. Phys.*, 194:742–772, 2004.

[171] W. R. Hwang, M. A. Hulsen, and H. E. H. Meijer. Direct simulation of particle suspensions in a viscoelastic fluid in sliding bi-periodic frames. *J. Non-Newton. Fluid*, 121:15–33, 2004.

[172] Y. J. Choi, M. A. Hulsen, and H. E. H. Meijer. An extended finite element method for the simulation of particulate viscoelastic flows. *J. Non-Newnon Fluid*, 165:607–624, 2010.

[173] Y. J. Choi, M. A. Hulsen, and H. E. H. Meijer. Simulation of the flow of a viscoelastic fluid around a stationary cylinder using an extended finite element method. *Comput. Fluids*, 57:183–194, 2012.

[174] N. J. Quinlan, M. Basa, and M. Lastiwka. Truncation error in mesh-free particle methods. *Int. J. Numer. Meth. Eng.*, 66:2064–2085, 2006.

[175] A. K. Chaniotis, D. Poulikakos, and P. Koumoutsakos. Remeshed smoothed particle hydrodynamics for the simulation of viscous and heat conducting flows. *J. Comput. Phys.*, 182:67–90, 2002.

[176] W. Benz. Applications of smoothed particle hydrodynamics (SPH) to astrophysical problems. *Comput. Phys. Commun.*, 48:97–105, 1988.

[177] J. J. Monaghan. Smoothed particle hydrodynamics. *Annu. Rev. Astron. Astrophys.*, 30(1):543–574, 1992.

[178] V. Springel. Smoothed particle hydrodynamics in astrophysics. *Annu. Rev. Astron. Astrophys.*, 48:391–430, 2010.

[179] G. R. Liu and M. B. Liu. *Smoothed particle hydrodynamics a meshfree particle method*. World Scientific Publishing Co. Pte. Ltd, Singapore, 2003.

[180] J. J. Monaghan. Smoothed particle hydrodynamics. *Rep. Prog. Phys.*, 68(8):1703 – 1759, 2005.

[181] J. J. Monaghan. Smoothed particle hydrodynamics and its diverse applications. *Annu. Rev. Fluid. Mech.*, 44:323–346, 2012.

[182] X. Y. Hu and N. A. Adams. Angular-momentum conservative smoothed particle hydrodynamics for incompressible viscous flows. *Phys. Fluids*, 18:101702, Dec. 2006.

[183] Xin Bian, Sergey Litvinov, Rui Qian, Marco Ellero, and Nikolaus A. Adams. Multiscale modeling of particle in suspension with smoothed dissipative particle dynamics. *Phys. Fluids (1994-present)*, 24(1), 2012.

[184] R. D. Groot and P. B. Warren. Dissipative particle dynamics: Bridging the gap between atomistic and mesoscopic simulation. *J. Chem. Phys.*, 107(11):4423–4435, 1997.

[185] V. Symeonidis and G. E. Karniadakis. A family of time-staggered schemes for integrating hybrid DPD models for ppolymer: algorithms and applications. *J. Comput. Phys.*, 218:82–101, 2006.

[186] E. G. Flekkøy and P. V. Coveney. From molecular dynamics to dissipative particle dynamics. *Phys. Rev. Lett.*, 83(9):1775–1778, 1999.

[187] E. G. Flekkøy, P. V. Coveney, and G. De Fabritiis. Foundations of dissipative particle dynamics. *Phys. Rev. E*, 62(2):2140–2157, 2000.

[188] P. Español. Hydrodynamics from dissipative particle dynamics. *Phys. Rev. E*, 52(2):1734–1742, 1995.

[189] J. M. V. A. Koelman and P. J. Hoogerbrugge. Dynamic simulations of hard-sphere suspensions under steady shear. *Europhys. Lett.*, 21:363–368, 1993.

[190] N. S. Martys. Study of a dissipative particle dynamics based approach for modeling suspensions. *J. Rheol.*, 49(2):401–424, 2005.

[191] S. Chen, N. Phan-Thien, B. C. Khoo, and X. J. Fan. Flow around spheres by dissipative particle dynamics. *Phys. Fluids*, 18:103605, 2006.

[192] W. Pan, B. Caswell, and G. E. Karniadakis. Rheology, microstructure and migration in Brownian colloidal suspensions. *Langmuir*, 26(1):133–142, 2009.

[193] M. Revenga, I. Zúñiga, P. Español, and I. Pagonabarraga. Boundary modesl in DPD. *Int. J. Mod. Phys. C*, 09:1319–1328, 1998.

[194] M. Revenga, I. Zúñiga, and P. Español. Boundary conditions in dissipative particle dynamics. *Comput. Phys. Commun.*, 121-122:309–311, 1999.

[195] I. V. Pivkin and G. E. Karniadakis. A new method to impose no-slip boundary conditions in disspative particle dynamcis. *J. Comput. Phys.*, 207:114–128, 2005.

[196] S. Litvinov, M. Ellero, X. Y. Hu, and N. A. Adams. Particle-layering effect in wall-bounded dissipative particle dynamics. *Phys. Rev. E*, 82(066704):066704, 2010.

[197] V. Pryamitsyn and V. Ganesan. A coarse-grained explicit solvent simulation of rheology of colloidal suspensions. *J. Chem. Phys.*, 122:104906, 2005.

[198] V. Pryamitsyn and V. Ganesan. Screening of hydrodynamic interactions in Brownian rod suspensions. *J. Chem. Phys.*, 128:134901, 2008.

[199] W. Pan, D. A. Fedosov, G. E. Karniadakis, and B. Caswell. Hydrodynamic interactions for single dissipative-particle-dynamics particles and their clusters and filaments. *Phys. Rev. E*, 78:046706, 2008.

[200] M. Whittle and K. P. Travis. Dynamic simulations of colloids by core-modified dissipative particle dynamics. *J. Chem. Phys.*, 132:124906, 2010.

[201] S. Jamali, M. Yamanoi, and J. Maia. Bridging the gap between microstructure and macroscopic behavior of mododisperse and bimodal colloidal suspensions. *Soft Matter*, 9:1506–1515, 2013.

[202] A. Vázquez-Quesada, M. Ellero, and P. Español. Consistent scaling of thermal fluctuations in smoothed dissipative particle dynamics. *J. Chem. Phys.*, 130(3):034901, 2009.

[203] C. A. Marsh, G. Backx, and M. H. Ernst. Fokker-Planck-Boltzmann equation for dissipative particle dynamics. *Europhys. Lett.*, 38(6):411–415, 1997.

[204] J. A. Backer, C. P. Lowe, H. C. J. Hoefsloot, and P. D. Iedema. Poiseuille flow to measure the viscosity of particle model fluids. *J. Chem. Phys.*, 122:154503, 2005.

[205] R. Qiao and P. He. Mapping of dissipative particle dynamics in fluctuating hydrodynamics simulations. *J. Chem. Phys.*, 128:126101, 2008.

[206] E. S. Boek, P. V. Coveney, and H. N. W. Lekkerkerker. Computer simulation of rheological phennomena in dense colloidal suspensions with dissipative particle dynamics. *J. Phys.: Condens. Matter*, 8:9509–9512, 1996.

[207] E. S. Boek, P. V. Coveney, H. N. W. Lekkerkerker, and P. van der Schoot. Simulating the rheology of dense colloidal suspensions using dissipative particle dynamics. *Phys. Rev. E*, 55(3):3124–3133, 1997.

[208] E. S. Boek and P. van der Schoot. Resolution effects in dissipative particle dynamics simulations. *Int. J. Mod. Phys. C*, 9(8):1307–1318, 1998.

[209] F. M. van der Kooij, E. S. Boek, and A. P. Philipse. Rheology of dilute suspensions of hard platelike colloids. *J. Colloid Interface Sci.*, 234:344–349, 2001.

[210] P. Español. Fluid particle dynamics: a synthesis of dissipative particle dynamics and smoothed particle dynamics. *Europhys. Lett.*, 39(6):605–610, 1997.

[211] P. Español. Dissipative particle dynamics with energy conservation. *Europhys. Lett.*, 40:631–636, 1997.

[212] S. Litvinov, M. Ellero, X. Y. Hu, and N. A. Adams. Smoothed dissipative particle dynamics model for polymer molecules in suspension. *Phys. Rev. E*, 77(6):066703, 2008.

[213] A. Vázquez-Quesada, M. Ellero, and P. Español. Smoothed particle hydrodynamic model for viscoelastic fluids with thermal fluctuations. *Phys. Rev. E*, 79(5):056707, May 2009.

[214] A. Vázquez-Quesada and M. Ellero. SPH simulations of a viscoelastic flow around a periodic array of cylinders confined in a channel. *J. Non-Newnon Fluid*, 167-168(5):1–8, 2012.

[215] P. M. Kulkarni, C.-C. Fu, M. S. Shell, and L. G. Leal. Multiscale modeling with smoothed dissipative particle dynamics. *J. Chem. Phys.*, 138:234105, 2013.

[216] I. F. Sbalzarini, J. H. Walther, M. Bergdorf, S. E. Hieber, E. M. Kotsalis, and P. Koumoutsakos. PPM - a highly efficient parallel particle-mesh library for the simulation of continuum systems. *J. Comput. Phys.*, 215:566–588, 2006.

[217] M. Metcalf and J. Reid. *Fortran 90/95 explained*. Oxford University Press, 2002.

[218] M. D. Carbajal-Tinoco, R. Lopez-Fernandez, and J. L. Arauz-Lara. Asymmetry in colloidal diffusion near a rigid wall. *Phy. Rev. Lett.*, 99:138303, 2007.

[219] Xin Bian and Marco Ellero. A splitting integration scheme for the {SPH} simulation of concentrated particle suspensions. *Comput. Phys. Commun.*, 185(1):53 – 62, 2014.

[220] Xin Bian, Sergey Litvinov, Marco Ellero, and Norman J. Wagner. Hydrodynamic shear thickening of particulate suspension under confinement. *J. Non-Newton Fluid Mech.*, 213:39 – 49, 2014.

[221] YS Lee, ED Wetzel, and NJ Wagner. The ballistic impact characteristics of kevlar woven fabrics impregnated with a colloidal shear thickening fluid. *J. Mater. Sci.*, 38(13):2825–2833, 2003.

[222] E. Brown, N. Rodenberg, J. Amend, A. Mozeika, E. Steltz, M. R. Zakin, H. Lipson, and H. M. Jaeger. Universal robotic gripper based on the jamming of granular material. *Proc. Natl. Acad. Sci. USA*, 107(44):18809–18814, 2010.

[223] A. Fall, N. Huang, F. Bertrand, G. Ovarlez, and D. Bonn. Shear thickening of cornstarch suspensions as a reentrant jamming transition. *Phys. Rev. Lett.*, 100:018301, 2008.

[224] A. Fall, F. Bertrand, G. Ovarlez, and D. Bonn. Shear thickening of cornstarch suspensions. *J. Rheol.*, 56(3):575–591, 2012.

[225] E. Brown, H. Zhang, N. A. Forman, B. W. Maynor, D. E. Betts, J. M. DeSimone, and H. M. Jaeger. Shear thickening in densely packed suspensions of spheres and rods confined to few layers. *J. Rheol.*, 54(5):1023–1046, 2010.

[226] E. Brown and H. M. Jaeger. The role of dilation and confining stresses in shear thickening of dense suspensions. *J. Rheol.*, 56:875–923, 2012.

6 Appendix: original journal papers

AIP | Physics of Fluids

Multiscale modeling of particle in suspension with smoothed dissipative particle dynamics

Xin Bian, Sergey Litvinov, Rui Qian, Marco Ellero, and Nikolaus A. Adams

Citation: Phys. Fluids **24**, 012002 (2012); doi: 10.1063/1.3676244
View online: http://dx.doi.org/10.1063/1.3676244
View Table of Contents: http://pof.aip.org/resource/1/PHFLE6/v24/i1
Published by the American Institute of Physics.

Multiscale modeling of particle in suspension with smoothed dissipative particle dynamics

Xin Bian,[a] Sergey Litvinov, Rui Qian, Marco Ellero, and Nikolaus A. Adams
Lehrstuhl für Aerodynamik und Strömungsmechanik, Technische Universität München, Boltzmannstr. 15, D-85748 Garching bei München, Germany

(Received 18 April 2011; accepted 30 November 2011; published online 19 January 2012)

We apply smoothed dissipative particle dynamics (SDPD) [Español and Revenga, Phys. Rev. E **67**, 026705 (2003)] to model solid particles in suspension. SDPD is a thermodynamically consistent version of smoothed particle hydrodynamics (SPH) and can be interpreted as a multiscale particle framework linking the macroscopic SPH to the mesoscopic dissipative particle dynamics (DPD) method. Rigid structures of arbitrary shape embedded in the fluid are modeled by frozen particles on which artificial velocities are assigned in order to satisfy exactly the no-slip boundary condition on the solid-liquid interface. The dynamics of the rigid structures is decoupled from the solvent by solving extra equations for the rigid body translational/angular velocities derived from the total drag/torque exerted by the surrounding liquid. The correct scaling of the SDPD thermal fluctuations with the fluid-particle size allows us to describe the behavior of the particle suspension on spatial scales ranging continuously from the diffusion-dominated regime typical of sub-micron-sized objects towards the non-Brownian regime characterizing macro-continuum flow conditions. Extensive tests of the method are performed for the case of two/three dimensional bulk particle-system both in Brownian/non-Brownian environment showing numerical convergence and excellent agreement with analytical theories. Finally, to illustrate the ability of the model to couple with external boundary geometries, the effect of confinement on the diffusional properties of a single sphere within a micro-channel is considered, and the dependence of the diffusion coefficient on the wall-separation distance is evaluated and compared with available analytical results. © *2012 American Institute of Physics*. [doi:10.1063/1.3676244]

I. INTRODUCTION

Particles suspended in a solvent matrix represent a common scenario embracing physical processes that occur at different spatial scales, ranging from macroscopic scale (on the order of millimeters and larger) typically found in processing engineering down to the sub-micron scale characterizing micro/nano-fluidics.

The modeling of particle suspensions is not only important to improve our understanding of the bulk rheological properties of complex particulate materials, a topic which is still subject of intense research[1] and industrial interest,[2] but also becoming an indispensable tool to target/optimize specific functionalities of novel devices operating under microfluidics conditions.[3,4] Manipulation/sorting/mixing of micro/nano-size objects is becoming the central focus of nanoparticle technology as well as, in the biomedical field, of novel platforms for hand-held diagnostics.[5] It is, therefore, extremely important to develop simultaneously theoretical and numerical models to fill the gap with rapidly evolving industrial applications.

Modeling of particle suspensions based on non-Brownian continuum approaches has often been proposed in the past using several grid-based techniques, such as finite elements methods,[6] distributed Lagrange-multiplier-based fictitious-domain methods (DLM)[7,8] and smoothed profile methods (SPM),[9,10] to mention but a few. These approaches are very useful but they rely on a

[a]Electronic mail: xin.bian@aer.mw.tum.de.

deterministic discretization of the hydrodynamic equations and are, therefore, limited to large Péclet number (defined as ratio of shear rate and mass diffusion) flow of supra-micron-sized particle suspensions. In several microflow conditions, the thermal noise, which manifests itself as the diffusional motion of the suspended objects, plays a key role in the dynamics. For example, an accurate description and measurement of the diffusion motion of a colloidal particle may be used as a highly sensitive probe for structure properties, both in distance and orientation, in the presence of complex boundaries.[11,12] Therefore, it is crucial to incorporate it into the adopted formalism.

Conventional schemes for the simulation of Brownian suspensions include a stochastic thermal force explicitly applied on the suspended bead while the effect of the hydrodynamic interactions (HIs) among them is implicitly taken into account via Oseen tensor-based models or higher-order expansions of the incompressible Stokes equations. Afterwards, a resulting set of algebraical equations need to be inverted. These approaches include, for example, Brownian dynamics (BD)[13] and Stokesian dynamics (SD).[14,15] Their main advantage is related to the good scalability of the number of equations with the number of suspended particles, allowing for the simulation of very large systems.[16] On the other hand, SD assumes that the time scales between the motions of fluid and those associated with particles are completely separated, which excludes the short-time motion of Brownian particles over kinematic time scale. Moreover, modeling arbitrarily shaped objects and complex boundary geometries is not an easy task and requires essential modification of the standard framework.[17] Generalization of SD to model nonspherical particles has been recently proposed in Ref. 18. In this approach, arbitrarily shaped rigid particles are modeled as clusters of several spheres which still interact via the usual SD forces, therefore, extending its range of applicability while increasing computational cost. Another approach which allows the simulations of arbitrarily shaped particles is based on boundary integral analysis.[19] Here, particle surfaces are discretized and a set of boundary integral equations based on the expansion of the Stokes equations must be solved for each surface element.

The direct numerical simulation (DNS) methods mentioned at the beginning of this section do not require any explicit model of the hydrodynamic interactions among particles being the solvent dynamics fully discretized. In order to be applied to microflow conditions, they need to be generalized. In Ref. 20, thermal fluctuations have been incorporated in an Eulerian finite volume scheme by including them in the discretized momentum equations by a random stress term equivalent to the fluctuating hydrodynamic equations of Landau and Lifshitz.[21] In this approach, the Brownian motion of a suspended object is implicitly induced by the thermal agitation of the solvent fluid and does not need to be modeled. A similar approach was previously applied also to lattice-Boltzmann (LB) simulation by Ladd and his coworker,[22,23] where a random stress term was introduced in the LB equation. A problem occurring in the LB simulations of suspended particles is, however, related to their unclear size which is not known *a priori*. One needs, therefore, to calibrate the simulations with a so-called hydrodynamic radius,[24] which can, however, be a complex function of the lattice size,[25] as well as the solvent kinematic viscosity.[26] Recently, some of these deficiencies have been significantly reduced by employing multiple relaxation time (MRT) approaches[26] or higher-order boundary conditions.[27] Similar to SD method, thermal fluctuations have been directly introduced on particles instead of fluid for SPM method, which was used to study diffusive behavior of Brownian spherical particles.[28,29] This poses again a potential difficulty for the simulation of nonspherical Brownian particles.

Another popular method which incorporates thermal noise is dissipative particle dynamics (DPD).[30] This represents a grid-off method in which the elements of fluid are modeled by particles interacting via soft conservative, frictional, and stochastic forces, the latter ones being related to the dissipative via the fluctuation-dissipation theorem (FDT).[31] The method is flexible, allowing for modeling arbitrarily shaped rigid structures by simply freezing DPD particles located inside the solid domain and letting them interact with the fluid particles.[30,32] It has been used to investigate the rheology of colloidal suspension under semi-dilute/concentrated flow conditions in Refs. 33 and 34. Recently, good results have been also obtained by simulating colloidal particles as single DPD particles interacting with the solvent ones via the ordinary DPD forces and among them with extra colloid-colloid interactions.[35,36] Although the results are qualitative and restricted to spherical particles only, the authors were able to simulate large concentrated systems and obtain the typical shear-thinning behavior observed experimentally.

Despite the good performance of DPD in simulating complex systems, the method still suffers of some shortcomings. The price for the simplicity of DPD is related to the lack of direct connection between the model parameters and the physical parameters of the system one tries to simulate. Usually, to specify the fluid transport coefficient, one needs to rely on kinetic theory[37] or map and calibrate the parameters in ways that are not always systematic.[38,39] Perhaps, the most serious problem is the specification of the spatial scale at which a DPD simulation operates, posing some difficulties on the separate identification of resolution and finite-size effects in the output results.[33,40] In particular, there is no unique definition of the hydrodynamic fluctuations acting on the fluid elements. The previous drawbacks have been addressed and solved in a modification of DPD (Ref. 41) denoted as smoothed dissipative particle dynamics (SDPD). The new particle model is entirely embedded in the GENERIC framework;[42,43] therefore, it maintains the thermodynamic consistency of the original DPD method, but in addition allows for a direct specification of the transport coefficient, i.e., viscosity, as input parameter. In fact, it has been shown that SDPD represents a generalization of the well-known smoothed particle hydrodynamics (SPH) which is a Lagrangian meshless Navier-Stokes solver proposed by Monaghan,[44,45] albeit with consistent introduction of thermal fluctuations.[46]

A remark on the amount of thermal fluctuations introduced in SDPD is in order. The scaling of SDPD thermal fluctuations with the fluid particle size has been investigated in Ref. 47 where it has been shown that their magnitude increases as the inverse of the square root of the fluid particle volume, in agreement with classical results in statistical mechanics. Therefore, whenever the fluid particle size is large enough, no thermal noise will be present in the hydrodynamic variables, whereas it will show up when the fluid description needs to be miniaturized, e.g., in microflow conditions. It is remarkable that the application of GENERIC together with a form of the dissipative terms taken from SPH allows for defining uniquely a size-dependent thermal noise which satisfies the FDT. The method has been recently applied to simulations of polymer molecules in suspension,[48,49] multiphase flows,[50] and viscoelastic liquids.[51]

In this paper, we present a multiscale model of arbitrarily shaped particle suspension based on SDPD which is able to operate on different flow conditions ranging continuously from the diffusion-dominated regime typical of micro/nano-sized objects to the non-Brownian regime typical of supra-micron-size particles. Moving rigid structures are modeled by freezing SDPD particles within the solid domain and letting them interact with the fluid particles. Artificial boundary velocities are assigned to the frozen solid boundary particles during the interaction with the fluid particles following Ref. 52, which allows for enforcing exactly the no-slip boundary condition on the solid-liquid interface.

The strict connection of the SDPD method to SPH enables us to investigate resolution effects in the Brownian regime by applying standard continuum convergence analysis to the results. The resolution studies and exact quantitative comparison in a Brownian environment are crucial, for example, to investigate the effect of particle-shape on microrheology which is based on many-points particle correlation measurements[53] and which represents our long-term research goal.[51]

The paper is organized as follows: Sec. II describes the deterministic and stochastic SDPD model of the solvent as well as the specific model of the rigid suspended structures and their interaction with the fluid. Numerical results of the particle-suspension model based on a strict convergence analysis under both non-Brownian and Brownian conditions are presented in Sec. III. Finally, conclusions and further developments are discussed in Sec. IV.

II. THE PARTICLE MODEL

A. Lagrangian hydrodynamic equations

Let us consider the isothermal Navier-Stokes equations in a Lagrangian framework,

$$\frac{d\rho}{dt} = -\rho \nabla \cdot \mathbf{v}, \tag{1}$$

$$\frac{d\mathbf{v}}{dt} = -\frac{\nabla p}{\rho} + \mathbf{F} + \mathbf{g}, \tag{2}$$

where ρ, $\mathbf{v}$, p, $\mathbf{F}$, and $\mathbf{g}$ are material density, velocity, pressure, viscous force, and body force, respectively. Following earlier studies of quasi-incompressible flow modeling,[54–56] an equation of state relating pressure to density can be written as

$$p = p_0\left[\left(\frac{\rho}{\rho_r}\right)^{\gamma} - 1\right], \tag{3}$$

where p_0 (related to sound speed c_s), $\gamma = 7$, and ρ_r are parameters chosen based on a scale analysis[52,55] such that pressure field reacts strongly to small derivations in mass density and quasi-incompressibility is enforced. Assuming Newtonian flow, the viscous force $\mathbf{F}$ simplifies to

$$\mathbf{F} = \nu\nabla^2\mathbf{v}, \tag{4}$$

where ν is the kinematic viscosity related to dynamic viscosity by $\nu = \eta/\rho$.

B. Deterministic solvent modeling

Equations (1) and (2) can be discretized in space by using the SPH method. The essence of SPH is an interpolation process allowing any function defined on a given domain to be expressed in terms of values at a discrete set of N disordered points—the particles.[44] Equation (1), the conservation of mass, is automatically satisfied if particle density is evaluated as[41]

$$d_i = \sum_j W_{ij}, \tag{5}$$

where $d_i = 1/\mathcal{V}_i$ is the number density associated to particle i, and $\mathcal{V}_i$ the corresponding volume. Accordingly, the mass density is evaluated as $\rho_i = m_i d_i$, where m_i is the mass of particle i; $W_{ij} = W(r_{ij}, h)$ is an even, bell shaped weighting function with smoothing length h, where $r_{ij} = |\mathbf{r}_i - \mathbf{r}_j|$ is the distance between particle i and j. For this work, we use a quintic spline[52] kernel characterized by a compact support with cutoff radius $r_c = 3h$.

Application of the SPH approximation to Eq. (2) produces the following equations for the particle positions and momenta:[41,50]

$$\dot{\mathbf{r}}_i = \mathbf{v}_i, \tag{6}$$

$$m_i\dot{\mathbf{v}}_i = -\sum_j\left(\frac{p_i}{d_i^2} + \frac{p_j}{d_j^2}\right)\frac{\partial W}{\partial r_{ij}}\mathbf{e}_{ij} + \sum_j \eta\left(\frac{1}{d_i^2} + \frac{1}{d_j^2}\right)\frac{\partial W}{\partial r_{ij}}\frac{\mathbf{v}_{ij}}{r_{ij}} + \mathbf{g}_i. \tag{7}$$

In the following, we will consider constant particle masses $m_i = m_0$ ($\forall i = 1, \ldots, N$). The first part on the rhs of the momentum equation represents a pressure force acting along the unit vector $\mathbf{e}_{ij} = \mathbf{r}_{ij}/r_{ij} = (\mathbf{r}_i - \mathbf{r}_j)/|\mathbf{r}_{ij}|$ joining particles i and j. Since it is a central force and symmetric by interchanging particle indices, total linear and angular momenta are exactly conserved. The irreversible viscous force is calculated in the second term of the rhs in Eq. (7) to reduce velocity differences between pair of particles. This force is symmetric by interchanging particle indices; therefore, it conserves linear momentum strictly. However, it is non-central, providing only approximate conservation of angular momentum.[41] The third term describes an external body force $\mathbf{g}_i$ as, for example, the gravity.

The SPH equations represent a discretization of the deterministic Newtonian hydrodynamics performed on Lagrangian elements of fluid.

C. Stochastic solvent modeling: Thermal fluctuations

Micro/nano-scopic flow problems are characterized by the presence of thermal fluctuations in the hydrodynamic variables. It was shown[41] that the GENERIC framework[42,43] allows for incorporating particle-fluctuations into Eq. (7) in a thermodynamically consistent way. In particular, the fluctuations of the momentum of particle i caused by thermal noise for an isothermal incompressible fluid are simply

$$d\widetilde{\mathbf{P}}_i = \sum_j \left[-4k_B T\eta \left(\frac{1}{d_i^2} + \frac{1}{d_j^2} \right) \frac{1}{r_{ij}} \frac{\partial W}{\partial r_{ij}} \right]^{1/2} d\overline{\overline{\mathbf{W}}}_{ij} \cdot \mathbf{e}_{ij}, \tag{8}$$

where k_B is the Boltzmann constant and T is the temperature; $d\overline{\overline{\mathbf{W}}}_{ij}$ is the traceless symmetric part of a matrix of independent increments of a Wiener process $d\mathbf{W}_{ij} = d\mathbf{W}_{ji}$, i.e., $d\overline{\overline{\mathbf{W}}}_{ij} = \left(d\mathbf{W}_{ij} + d\mathbf{W}_{ij}^T \right)/2 - tr[d\mathbf{W}_{ij}]\mathbf{I}/d$, where d is the spatial dimension.[41,50] Particle-velocity statistics satisfy the Maxwell-Boltzmann distribution, and their variance is given by[47]

$$\langle v^2 \rangle = d \frac{k_B T}{\rho_0 \mathcal{V}_i}, \tag{9}$$

where ρ_0 is the equilibrium fluid density. Thus, velocity fluctuations emerge naturally and increase in magnitude following the correct scaling as the spatial scales of the problem, i.e., the particle volumes $\mathcal{V}_i$, become smaller.[47]

The introduction of the term in Eq. (8) into the particle momentum equation corresponds to the so-called smoothed dissipative particle dynamics method. SDPD allows for extending the applicability of the SPH method to micro/nano scales. Unlike standard mesoscopic methods where finite-size/resolution effects are difficult to control,[33,40] the strict connection with SPH enables SDPD to perform numerical convergence studies in a Brownian environment by using established SPH error analysis,[56,57]; on the other hand, whenever the physical scale of the problem ranges in the macroscopic scale, it reduces to a version of SPH by setting $T = 0$.

D. Modeling of a suspended solid particle

To model moving solid objects suspended in the fluid domain, one must be able to enforce the no-slip velocity boundary condition on any, possibly arbitrary, solid-liquid interface. This can be achieved by using the following strategy: initially, all SDPD particles are placed on regular lattice with distance $dx = dy(= dz)$ throughout the entire computational domain (solid and liquid). Once a given object geometry is prescribed, we can detect all the SDPD particles lying inside the solid domain B and identify them as *solid boundary particles*; the remaining ones are identified as *fluid particles*, and their evolution of hydrodynamic properties is determined from Eqs. (6)–(8). Solid boundary particles interact with fluid particles by the same Eqs. (7) and (8). However, unlike the fluid particles, their properties are not prescribed in terms of an evolution equation but must be assigned to enforce the correct conditions on the interface.

In the pioneering works on DPD modeling of colloidal suspensions,[32,33] particles inside a solid domain are "frozen" and their velocities are assigned to be equal to the rigid body motion of the modeled structure. However, this choice introduces a zero-order no-slip boundary condition and leads to an ill-defined effective structure surface at moderate resolution. To guarantee better no-slip condition at the surface of the solid object, we extend the work of Morris *et al.*[52] to describe translation, rotation, and more general shapes of solid particles.

In the following, a solid particle is considered neutrally buoyant with density equal to the equilibrium solvent density ρ_0. During the simulation, its density is kept constant, and so is its mass ($M_C = \rho_0 \mathcal{V}_C$), while density of solvent may slightly fluctuate. Let us assume that the solid particle with center location $\mathbf{R}_C$ is translating with velocity $\mathbf{V}_C$ and rotating with angular velocity Ω_C. Before the velocity-dependent viscous force calculation between a solvent particle f and a boundary particle b, an artificial velocity must be assigned to b which will result in an effective no-slip condition on the surface. The artificial velocity is calculated as follows (schematic illustration in Fig. 1): the normal distance d_f from f to the surface point s is calculated, from which the tangent plane (a line in two dimensions) $\mathbf{l}_s$ is defined. Afterwards the normal distance d_b from b to $\mathbf{l}_s$ is calculated. An artificial velocity on particle b is extrapolated from the known velocity of particle f assuming zero relative velocity on the tangent plane, that is,

$$\mathbf{v}_b = -(d_b/d_f)\left(\mathbf{v}_f - \mathbf{v}_s\right) + \mathbf{v}_s, \tag{10}$$

where $\mathbf{v}_s = \mathbf{V}_C + \Omega_C \times (\mathbf{r}_s - \mathbf{R}_C)$ and $\mathbf{r}_s$ is the position vector of point s.

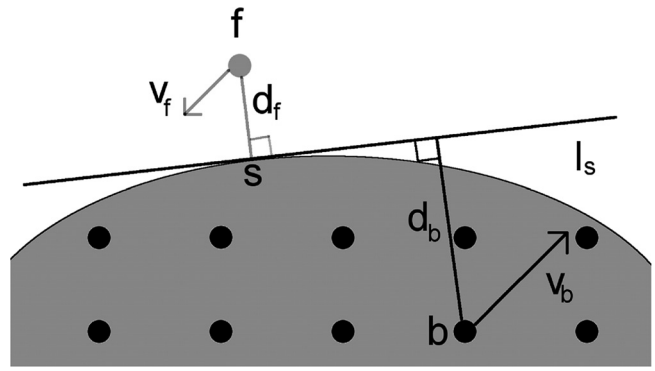

FIG. 1. A convex portion of a solid particle: f is a fluid particle and b is a boundary particle; s is the closest point on the surface to f and $\mathbf{d}_f \perp \mathbf{l}_s$, $\mathbf{d}_b \perp \mathbf{l}_s$; artificial velocity $\mathbf{v}_b = -(d_b/d_f)(\mathbf{v}_f - \mathbf{v}_s) + \mathbf{v}_s$ is used for viscous, stochastic force calculation.

s is always calculated as the closest point to fluid particle f. A distinction between convex and concave surfaces, as suggested in Ref. 52 was found to be unnecessary. For both convex and concave surfaces, the cutoff r_c should be at least smaller than the smallest surface curvature radius to have a converged result (in this article, convergence means that with a fixed number of neighboring particles, relevant results do not change as the total number of particles increases, see Sec. III). Note that $\mathbf{v}_b$ is not used to integrate boundary particle position but to enforce the correct interpolation only.

Assuming that the boundary particle b has the same viscosity η and temperature T as the solvent particle f, viscous and stochastic forces between particles b and f can be evaluated. Concerning the pressure boundary condition, we consider a Neumann condition with zero derivative between a fluid particle and a boundary particle, i.e., by linear approximation $p_b = p_f$, which allows to determine the pairwise pressure force in Eq. (7). Boundary particles are treated in the same way as solvent particles for the pair force calculation, except that two boundary particles belonging to the same structure do not interact with each other.

The procedure is repeated for every particle pair (b,f). Once all pair interactions involving b have been calculated, a total force $\mathbf{F}_b$ on b is summed up. Finally, a total force exerted by the surrounding solvent particles on the entire solid object can be obtained as $\mathbf{F}_C = \sum_{b\in B} \mathbf{F}_b$, where B is the domain occupied by the solid object. Accordingly, the translational acceleration of the solid particle is $\mathbf{a}_C = \mathbf{F}_C/M_C$. Similarly, a total torque on the solid can be calculated as $\tau_C = \sum_{b\in B} (\mathbf{r}_b - \mathbf{R}_C) \times \mathbf{F}_b$, and its angular acceleration is evaluated as $\alpha_C = \tau_C/I_C$, where I_C is momentum of inertia of the solid.

In practice, boundary particles do not fill the entire structure but are considered only within a thin layer of width r_c inside the surface of the solid. This choice saves computational time, especially for concentrated suspensions where the number of boundary particles can become comparable to the fluid ones. The same approach discussed above can be applied also to the modeling of arbitrary solid walls with random boundary particle distributions, which has been shown to reproduce better the mechanical properties of nano-systems.[49]

E. Time integration

An explicit modified velocity Verlet algorithm with $\lambda = 1/2$ is used as time integrator for solvent particles,[58]

$$\begin{aligned}
\widetilde{\mathbf{v}}_i(t+\Delta t) &= \mathbf{v}_i(t) + 1/2\Delta t \mathbf{f}_i(t),\\
\mathbf{r}_i(t+\Delta t) &= \mathbf{r}_i(t) + \Delta t \widetilde{\mathbf{v}}_i(t+\Delta t),\\
\mathbf{f}_i(t+\Delta t) &= f_i(\mathbf{r}(t+\Delta t), \widetilde{\mathbf{v}}(t+\Delta t)),\\
\mathbf{v}_i(t+\Delta t) &= \widetilde{\mathbf{v}}_i(t+\Delta t) + 1/2\Delta t \mathbf{f}_i(t+\Delta t),
\end{aligned} \tag{11}$$

where by predicting velocity before updating position, $\widetilde{\mathbf{v}}$ does not need to be stored, as it can occupy the same memory location as $\mathbf{v}$.

Some pioneers of DPD used $\widehat{\mathbf{v}}_b = V_C + (\mathbf{r}_b - \mathbf{R}_C) \times \Omega_C$ to update each solid-boundary-particle position at every time step. However, when the tangential component $(\mathbf{r}_b - \mathbf{R}_C) \times \Omega_C$ is multiplied by a finite Δt, the particle trajectory can cause an artificially expanding solid structure, which causes numerical instability. We have followed Ref. 59 and used a rotation matrix to track rotational solid structure. Both translational and rotational motions of a solid particle are updated using the same time integrator as solvent particles.

To maintain numerical stability of the explicit scheme, the time-step size Δt must be restricted by two conditions:[52] $\Delta t \leq (1/8)h^2/\nu$ and $\Delta t \leq (1/4)h/c_s$. For deterministic low Reynolds number flow problems with large resolutions, the viscous constraint is usually the dominating criterion.[52] However, in flow problems where the Brownian motion is important, the Courant-Friedrichs-Lewy (CFL) condition[60] may be the most strict limitation.

III. NUMERICAL RESULTS

In this section, we validate the SDPD model for suspended particles. A parallel version of the SDPD algorithm has been implemented using the parallel particle mesh (PPM) library[61] Non-Brownian test cases include: (1) flow through porous media, (2) dynamics of an isolated impulsively started solid particle, (3) a rotating particle under shear flow, and (4) hydrodynamic interactions between two approaching spheres; validation under Brownian conditions are considered by studying the translational/rotational diffusive behavior of a neutrally-buoyant rigid particle suspended in a solvent medium with periodic boundaries and anisotropic diffusion of a rigid particle near a planar wall.

In non-dimensional units, the solid particle radius R_C and equilibrium density ρ_0 are both equal to one. Simulations start with SDPD particles initially placed on a square (cubic) lattice with distance $dx = dy(= dz)$.

For deterministic simulations, the typical velocity V (either inflow velocity or solid particle's velocity) has the value of unity. Therefore, time has unit of R_C/V. A smoothing length $h = \kappa dx$ with $\kappa = 1.6$ (2D) or $\kappa = 1.33$ (3D), corresponding to an average number of neighboring particles of approximately 70 or 250, is adopted.

For Brownian simulations, the input energy $k_BT = 1$. Therefore, the velocity has unit of $\sqrt{k_BT/M_C}$ and time has unit of $R_C/\sqrt{k_BT/M_C}$. $\kappa = 1.0$ is universally used in both 2D and 3D simulations, corresponding to an average number of neighbors equal approximately to 27 and 106, respectively.

The speed of sound c_s is chosen to be at least 10 times larger than the typical velocity to keep fluid density variations reasonably small,[55] to balance pressure, viscous, and body forces,[52] and to satisfy time scale separation[62] (sonic time τ_c much smaller than viscous time τ_ν, i.e., $R_C/c_s \ll R_C^2/\nu$).

A. Flow through porous media

As the first test case, we consider the flow through a square/cubic periodic array of fixed circular/spherical objects. Hasimoto[63] derived an analytical expression of the drag coefficients for dilute arrays of disks and spheres by solving the Stokes equations of motion in Fourier space. Later, Sangani and Acrivos[64] extended Hasimoto's expressions to the semi-dilute case by including higher-order terms. In the two-dimensional case, the drag coefficient λ_{2D} is

$$\frac{F}{\eta V} = 4\pi\left[-\frac{1}{2}\ln C - 0.738 + C - 0.887C^2 + 2.039C^3 + O(C^4)\right]^{-1}, \tag{12}$$

where F is the drag on the disk, V is a far-field velocity, and $C = \pi R_C^2/L^2$ is the disk concentration. SDPD simulations have been performed with kinematic viscosity $\nu = 41.67$, maximum chosen sound speed $c_s = 2000$, and temperature $T = 0$ (non-Brownian regime). A fixed disk radius $R_C = 1.0$ is considered while different box lengths L are used to obtain different concentrations C. An inflow velocity $V = 1.0$ is chosen which defines a Reynolds number $\mathrm{Re} = VR_C/\nu \approx 0.024$ and a Mach number $\mathrm{Ma} = V/c_s = 5.0 \times 10^{-4}$.

By fixing the kernel overlap ($r_c = 3h = 4.8dx$) and changing resolutions (total number of particles), converged results were achieved according to the resolutions given in Table I. By increasing

TABLE I. Converged resolutions used in the simulation of flow through array of disks: $dx = dy$, $N_x = N_y$.

L	**15.0**	**7.5**	**5.0**	**4.0**	**3.5**	**3.0**	**2.7**	**2.5**	**2.3**	**2.2**
dx	0.1	0.1	0.1	0.05	0.0357	0.03125	0.025	0.02	0.0115	0.0088
N_x	150	75	50	80	98	96	108	125	200	250

L, the only constraint on resolution was the geometry of disk, which did not change. Therefore, resolutions are the same in Table I for box lengths $L \geq 5.0$. It has been suggested previously that, to obtain converged results, each pore throat/gap should be spanned by at least 15 fluid particles.[65] Therefore, when decreasing L, the number of particles in the gap between disks should be kept around 15.

Sangani and Acrivos[64] obtained a two-dimensional "lubrication approximation" for λ_{2D} in concentrated cases,

$$\frac{F}{\eta V} = \frac{9\pi}{2\sqrt{2}}\left[1 - \left(\frac{C}{C_{max}}\right)^{1/2}\right]^{-5/2}, \tag{13}$$

where the highest packing ratio is estimated as $C_{max} = \pi(R_C)^2/(2R_C)^2 \approx 0.785$ in the case of a square array of disks. Concentrated case up to $C = 0.649$ has been simulated and converged results obtained with the resolutions given in Table I. For $C = 0.649$, the total number of particles according to the converged resolution should be $N = N_x \times N_y = 250^2 = 62\,500$. However, the thin-layer surface model for the disk (see Fig. 2) allow to reduce N to 25 424 which reduces the number of particles of 60%. The thin-layer model becomes clearly even more effective in a concentrated three-dimensional system where the volume occupied by the solid objects increases as R_c^3.

Converged results for the drag coefficient are shown in Fig. 3, where good agreement with analytical theories and the two-dimensional direct DNS of Sangani and Acrivos[64] are achieved.

According to Table II, three-dimensional simulations of spheres for concentrations ranging from the dilute to semi-dilute regime have also been performed and again λ_{3D} compared with the theory of Sangani and Acrivos,[66] which in this case reads

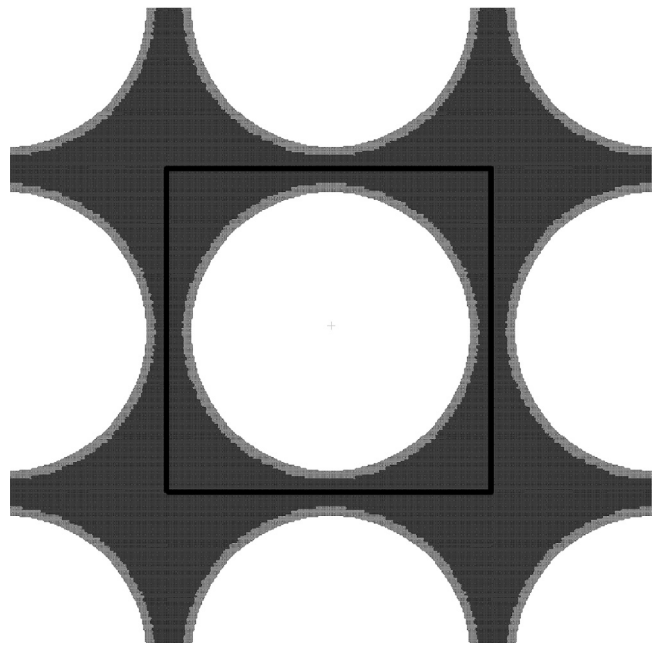

FIG. 2. A square periodic array of disks at the maximal concentration $C_{max} = 0.649$ simulated: light color are boundary particles and dark color are solvent particles. Number of particles used for converged results was $N = 25424$ while N could have been 62 500 without thin-layer model. Simulation was performed only within the black square box with periodic boundary conditions applied at its boundaries.

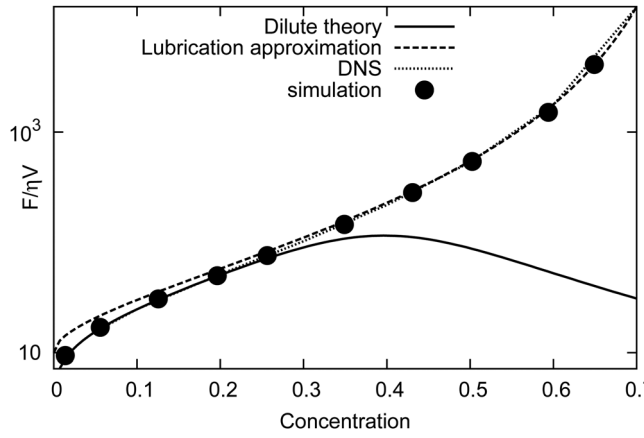

FIG. 3. Two-dimensional dimensionless drag coefficient: comparison with theories and DNS of Sangani and Acrivos.[64]

$$\frac{F}{6\pi\eta RV} = [1 - 1.7601C^{1/3} + C - 1.5593C^2 + 3.9799C^{8/3} - 3.0734C^{10/3} + O(C^{11/3})]^{-1}, \quad (14)$$

where the spheres concentration is $C = 4\pi R_C^3/3L^3$. The comparison of the converged simulation results with Eq. (14) is shown in Fig. 4, and again good agreement is achieved.

As shown from the 2D/3D drag coefficients above, the improvement on the no-slip boundary condition adopted gives effective hydrodynamic radius R_H equal to the input R_C even at moderate resolution. We have simulated problem described above also with frozen boundary particles (results not shown), i.e., without interpolation for the boundary particle velocity: the convergence of drag on the disk/sphere is much slower; therefore, $R_H \neq R_C$, similar to LB method.

B. Impulsively started non-Brownian particle

To test our particle model under unsteady situations, we have considered a circular/spherical particle moving in a Newtonian fluid. The fluid is initially at rest with kinematic viscosity $\nu = 20.0$, $c_s = 100.0$, and $T = 0$. A square(2D)/cubic(3D) computational domain with length L is considered with periodic boundary conditions applied in every direction. $L = 30$ is chosen to approximate the limiting case of an infinite solvent medium and to eliminate artificial effects due to the presence of periodic images.

At time $t = 0$, a velocity $V_C(t = 0) = V_0 = 1.0$ is assigned to the solid particle which approximates a Stokes flow, the corresponding Reynolds number is $\mathrm{Re} = R_C V_0/\nu = 0.05 \ll 1$ and Mach number is $\mathrm{Ma} = 0.01 \ll 1$.

We monitor the particle-velocity decay $V(t)$ as a function of time in the reference frame of the total system's center of mass, i.e., $V(t) = (V_C(t) - V_{CM})/(V_0 - V_{CM})$, where V_{CM} is the velocity for center of total mass. Since the total mass and momentum are conserved, $V_{CM} = M_C V_0/(M_C + M_f)$ is constant also, where $M_f = \sum_i m_i, \forall i \notin B$.

The evolution of $V(t)$ in a two-dimensional simulation is shown in Fig. 5(a). After an initial exponential decay, the typical long-time algebraic decay[67,68] $\propto t^{-1}$ is observed which is due to the hydrodynamic self-particle interaction. An enlarged logarithmic plot of the velocity decay is shown in the inset of the figure where the correct algebraic time-dependence can be observed.

TABLE II. Converged resolutions used in the simulation of flow through array of spheres: $dx = dy = dz$, $N_x = N_y = N_z$.

L	7.0	6.0	5.0	4.5	4.0	3.5	3.2	2.8	2.5
dx	0.1	0.1	0.1	0.1	0.1	0.07	0.05925	0.04	0.025
N_x	70	60	50	45	40	50	54	70	100

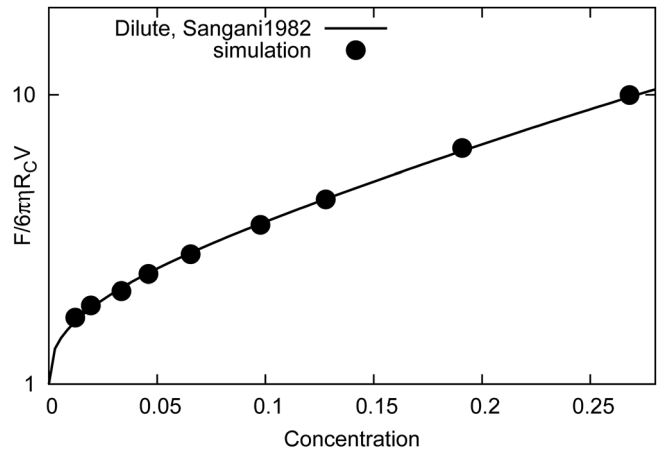

FIG. 4. Three-dimensional dimensionless drag coefficient: comparison with theories of Sangani and Acrivos.[66]

Same arguments apply to the three-dimensional case where the $V(t)$ of the corresponding sphere is shown in Fig. 5(b). Here, algebraic decay is also observed but the scaling is $\propto t^{-3/2}$ in agreement with the theory.[67]

C. A rotating particle under shear flow

As mentioned earlier in Sec. II B, the viscous force formulation adopted in Eq. (7) (formulation A for brevity) does not conserve strictly the angular momentum. We examine the accuracy of torque τ_C acting on a particle by performing two dimensional simulations of a rotating disk under a simple shear flow. The Stokes solution of τ_C in the case of low Reynolds number is given[69] as

$$\tau_C = 4\pi\dot{\gamma}\rho_0\nu R_C^2\left(\frac{1}{2} - \frac{\Omega}{\dot{\gamma}}\right), \tag{15}$$

where $\dot{\gamma}$ is the shear rate and Ω is the angular speed of the disk. The solvent particles are placed at distance with $dx = 0.2$, $\eta = 8.46$; therefore $\nu = \eta/\rho_0 = 8.46$, $C_s = 15.0$. Box size is taken as $L_x = L_y = 20.0$, which is sufficiently large to minimize the wall or periodic image effects. Shear rate between two parallel walls is $\dot{\gamma} = 0.10575$, which defines $Re = \dot{\gamma}R_C^2/\nu = 0.0125$ for the disk. The rotating speeds of the disk are taken as -0.14, -0.07, 0.0, 0.07, 0.14, where "—" means opposite direction of the shear rate. The results are shown in Fig. 6, where formulation A produces incorrect results, and the error of the torque is proportional to the absolute value of the angular speed. We compare the slope of the linear fit for torques at different speeds with the analytical solution. With resolution $dx = 0.2$, the slope has 52% relative error and with a doubled resolution $dx = 0.1$, the error reduces only to 48%. This error does not result from the thin-layer model, since during the rotation the mass of the disk is assumed to be evenly distributed. The discrepancy of

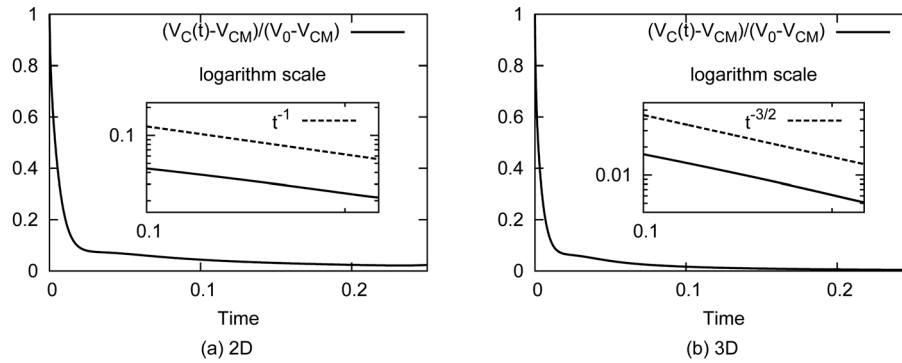

FIG. 5. Algebraical decay of normalized velocity: (a) 2D disk and (b) 3D sphere.

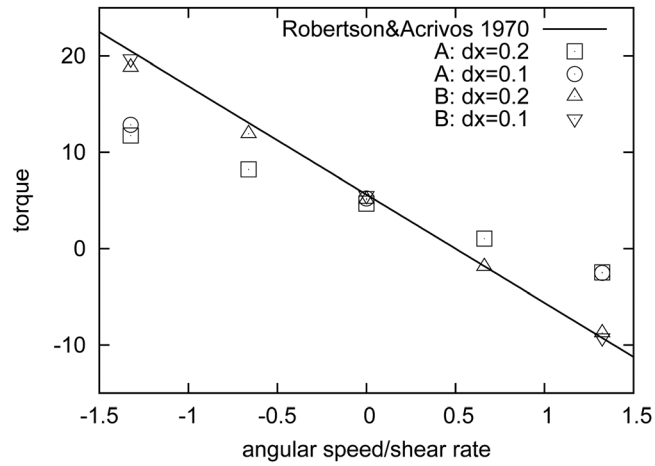

FIG. 6. Torque of a rotating disk under shear flow: formulation A does not conserve angular momentum and produces wrong torque; formulation B conserves angular momentum and produces accurate torque.

the torque should be due to the fact that the viscous force of formulation A is not acting along the center-to-center line between particle pairs; therefore, the angular momentum is not exactly conserved.

The torque may be captured accurately by selecting a type of viscous force acting along the center-to-center line of two particles. We select $F_{ij}^{vis} = 4\eta\left(\frac{1}{d_i^2}+\frac{1}{d_j^2}\right)\frac{\partial W}{\partial r_{ij}}\frac{\mathbf{e}_{ij}\cdot\mathbf{v}_{ij}}{r_{ij}}\mathbf{e}_{ij}$ (formulation B for brevity) from Ref. 70 to replace the viscous force in Eq. (7) and perform the same simulations. The results are also shown in Fig. 6 for comparison, where torque is captured accurately at all rotating speeds, with the error of the slope of linear fit below 3%.

Note that according to FDT viscous formulation B has different expression for thermal fluctuations as counterpart. Formulation B, although improving the results in case of rotating particles, has no effect on their drag. We have explicitly checked this by repeating the simulations presented in Sec. III, obtaining derivations in the results with respect to formulation A below 1%; therefore, the conclusions remain invariant. In the following test cases, standard formulation A will be considered.

D. Hydrodynamic interactions between moving particles

In a concentrated suspension of solid particles, the HIs between them play a crucial role for the macroscopic properties of the bulk system.[71] In this section, we investigate the accuracy of SDPD in describing them. This is an important test case for dynamic simulations of particle suspension, as it can estimate the minimal fluid resolution needed for the correct modeling of the interstitial fluid.

Analytical solutions are available for two spheres defined in a unbounded domain and interacting implicitly through the solvent. In particular, we consider the two following situations: (1) two spheres approaching each other with equal but opposite velocity along their center-to-center line; (2) two spheres moving with relative velocity perpendicular to their center-to-center line.

1. Squeezing motion

Two identical spheres ($R_C^1 = R_C^2 = 1.0$) are immersed in a quiescent solvent characterized by $\nu = 40.0$, $c_s = 400.0$, and $T = 0$. At time $t = 0$, they are forced to start moving with constant velocity magnitude $|\mathbf{V}_x| = 1.0$ towards each other along their center-to-center line until touching. The corresponding Reynolds number $\mathrm{Re} = VR_C/\nu = 2.5 \times 10^{-2}$ and Mach number $\mathrm{Ma} = V/c_s = 2.5 \times 10^{-3}$. A rectangular domain of size $[14, 9, 9]$ is found to be necessary to remove box size effects due to periodic images.

The three-dimensional solution for the drag coefficient $\mathrm{F}_{\|}$ of two nearly touching spheres parallel to their center-to-center line can be obtained by using the method of reflections.[72,73] This is

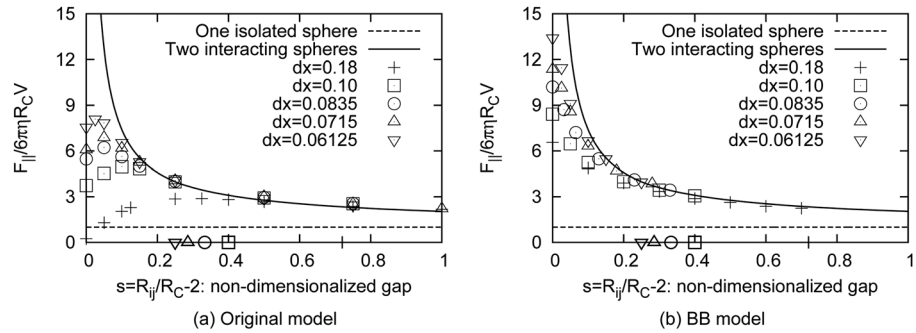

FIG. 7. Drag coefficients vs. gap s between two spheres approaching each other along their center-to-center line (squeezing motion): (a) interactions allowed only through solvent particles; (b) interactions between boundary-boundary particles of different spheres also allowed. The symbols on s axis are r_c corresponding to different resolutions.

plotted in Fig. 7 (solid line) and compared with SDPD simulations for several particle resolutions. Note that for gap distances $s \leq r_c$, kernels centered on boundary particles of different solid spheres could start overlapping and the corresponding SDPD particles could in principle interact.

We consider first the situation where no interaction between different boundary particles is allowed (Fig. 7(a)), and the HIs are mediated uniquely by the solvent. HI are well resolved at moderate inter-particle distances, whereas they start deviating from the theoretical solution as s is getting smaller and eventually they fail completely to recover the expected singular behavior for $s \to 0$. Symbols on the abscissa correspond to the typical cutoff radii r_c used for different resolutions. It can be observed that HI deviate typically for $s \leq r_c/2$, corresponding to less than two fluid particles in the interstitial region along the center-to-center line. At smaller distances, fluid particles in the gap are completely squeezed out, producing smaller repulsive forces and, eventually, depleted layers. Therefore, for two freely moving spheres in a real dynamic simulation, penetration could occur due to absence of any extra force between nearly touching spheres other than the implicit one mediated by the SDPD solvent.

To increase pressure and viscous force between solid particles at small gap distances, we consider the next case in which two boundary particles belonging to different spheres are allowed to interact through the forces described in Eq. (7). Since in this case no specific boundary condition must be enforced, we assign to the boundary particles the "real" rigid body velocity of the corresponding solid structure. This second type of model is denoted for brevity as BB (boundary-boundary). Again, we have performed simulations with different resolutions, and the results are shown in Fig. 7(b). Due to the extra boundary-boundary particle interactions, HIs are recovered up to smaller gap distances and, unlike the previous case, they increase monotonically as decreasing s. This modification introduces extra forces between boundary particles of different spheres which should not be present in a continuum description. However, the range of interaction falls below the typical cutoff radius r_c, and therefore, they can be interpreted as a sub-particle scale lubrication model which prevents penetration. Although improved, the singular behavior is not correctly captured for $s \to 0$. This is, however, not surprising as the interaction forces between particle-pair in Eq. (7) are themselves not singular.

To capture the correct singular behavior at $s \to 0$, either larger resolutions or explicit lubrication corrections could be considered, similar to those presented in Ref. 74, for example, which are, however, limited to spherical particle and do not apply to the arbitrarily shaped objects considered in this work. A more general approach to model the short-range lubrication could be represented by the introduction of extra pair forces between boundary particles belonging to different solid objects with functional form, for example, of the type used in Ref. 36. This approach is currently under investigation and will be presented in a future work.

2. Shear motion

The three-dimensional solution for two spheres moving perpendicular to their center-to-center line is also given in Refs. 72 and 73. Simulations have been performed with two spheres moving

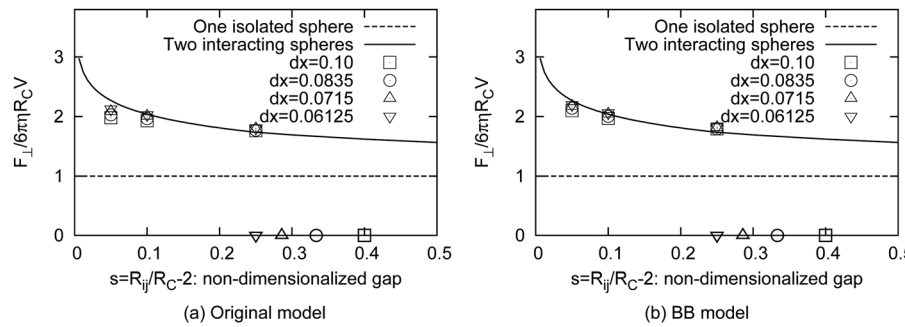

FIG. 8. Drag coefficient vs. gap s between two spheres in opposite motion perpendicular to their center-to-center line (shear motion): (a) interactions through only solvent particles; (b) interactions between boundary-boundary particles of different spheres also allowed. The symbols on s axis are r_c corresponding to different resolutions.

with the same constant velocity magnitude ($|\mathbf{V}_y| = 1.0$) in opposite directions. In this case, box size $[12, 8, 8]$ is considered sufficient to eliminate image effects. Similar to Sec. III D 1, results for two spheres interacting only through solvent particles are shown in Fig. 8(a) for different resolutions. Since for the shear motion considered here there is no squeezing of solvent particles in the gap, good results for $F_\perp$ are obtained up to gap distances $\sim r_c/4$ corresponding to one single SDPD particle only describing the interstitial fluid. Again, slightly better results at smaller distances are achieved by considering extra boundary-boundary particle interactions, see Fig. 8(b).

Note also the much softer logarithmic dependence of $F_\perp$ on s compared to $F_\parallel$ in Fig. 7, suggesting that $F_\parallel$ produced by fluid squeezing between nearly touching spheres should dominate the dynamics for concentrated suspensions.

E. Brownian translation/rotation of solid particle

A micro/nano-sized solid particle is affected by the presence of thermal fluctuations producing its ultimate Brownian diffusive dynamics. In this section, we validate our method for temperature $T \neq 0$ in Eq. (8). A single solid particle is defined in a two/three dimensional domain and its diffusional behavior studied. In particular, we focus on a convergence analysis of its mean square displacements (MSDs) in two-dimensional domain, to understand possible resolution-dependent effects, which provide a guideline for 3D simulations.

1. Brownian disk

A disk of radius $R_c = 1.0$ free to translate and rotate is contained in a periodic square domain of size $L_{x,y} = 5.0$. Fluid solvent is modeled as SDPD particles and characterized by kinematic viscosity $\nu = 15.0$ and thermal energy $k_BT = 1.0$. One such simulation with $t_{end} \approx 340$ is called one realization. To check numerical convergence of the results, three different particle-resolutions are considered: $dx = 0.2$, 0.125, and 0.1.

According to Eq. (9), the maximum variance of solvent thermal velocity (v_{th}^{max}) occurs in the case of highest resolution ($dx = 0.1$). Therefore, we chose the sound speed $c_s \approx 15 v_{th}^{max} = 343.24$ to all the resolutions considered so that a small density variation is obtained. The thermal velocity of the disk is $V_{th} = \sqrt{2k_BT/M_c} = 1.414$; therefore, $Re = V_{th}R_C/\nu = 0.094$ and $Ma = V_{th}/c_s = 0.00412$.

To obtain statistical averages, 50 realizations have been performed for each resolution starting with different random number seed. Velocity probability distribution functions (PDF) for both solvent particles and solid disk satisfy Maxwell-Boltzmann distribution,[47]

$$f(v) = \sqrt{\frac{m}{2\pi k_B T}} exp\left(\frac{-mv^2}{2k_BT}\right). \tag{16}$$

It has been shown that the PDF for solvent particles velocity scales consistently with resolutions while for a solid particle with predefined volume is fixed independent of resolutions.[47]

We check further the diffusive behavior of the disk by calculating its translational and rotational MSD, which are defined as

$$MSD_t(\tau) = \left\langle \mathbf{R}_C^2(t+\tau) - \mathbf{R}_C^2(t) \right\rangle \tag{17}$$

and

$$MSD_r(\tau) = \left\langle \Theta_C^2(t+\tau) - \Theta_C^2(t) \right\rangle, \tag{18}$$

where Θ_C is rotating angle and $\langle\rangle$ is the ensemble average taken over at time t with a time interval τ. The translational MSDs for different resolutions are shown in Fig. 9, where the correct behavior is captured at a rather rough resolution ($dx = 0.2$). The rotational MSDs for different resolutions are plotted in Fig. 10 showing converged results at $dx = 0.125$. Since the momentum of inertia for the disk is fixed for different resolutions, the relative slower convergence of resolution (compared to translation) can be due to the deficiency of torque calculation at low resolution.

The simulations show consistent diffusion behavior for a predefined inclusion as long as the resolution is high enough to calculate force/torque correctly. Due to the connection with SPH, resolution effects, which are somehow difficult to control in DPD methods,[33,40] can be analyzed straightforward in SDPD.

2. Brownian sphere

We performed 15 realizations of a single spherical particle diffusing in a three-dimensional periodic box of size $L_{x,y,z} = 5.0$. We chose $dx = 0.2$, since it is sufficient to capture the translational behavior. All other parameters in these simulations are the same as in the two-dimensional case.

We checked the velocity PDF of solvent particles and compared it with Maxwell-Boltzmann distribution in Fig. 11, where good agreement is obtained. The PDF of the spherical-particle velocity is also validated in Fig. 12.

According to the Einstein-Stokes equation,

$$D_0 = \frac{k_B T}{6\pi\eta R_C}, \tag{19}$$

the diffusion coefficient D_0 of a sphere suspended in an infinite fluid medium can be predicted by the temperature and viscosity of the fluid. If the fluid domain is finite and periodic, the dynamics of the sphere is affected by the complex hydrodynamic interactions with its images. The actual diffusion coefficient D has a correction from D_0 which reads[20]

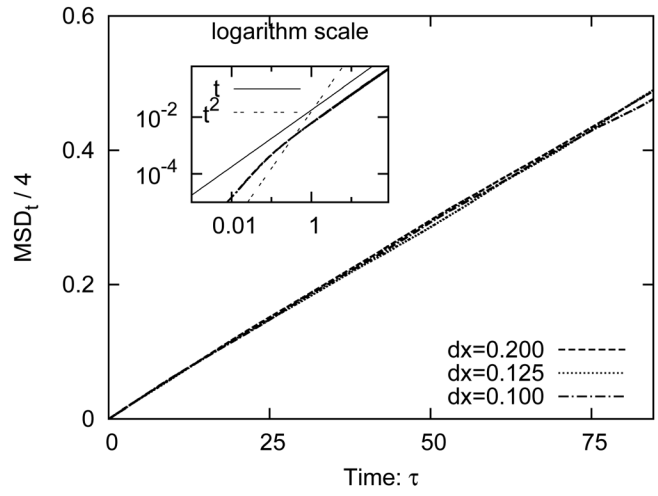

FIG. 9. Convergence of translational mean square displacement for a disk: the slope represents the translational diffusion coefficient in 2D; the inset shows the transition from ballistic to diffusive regime in log-log scale.

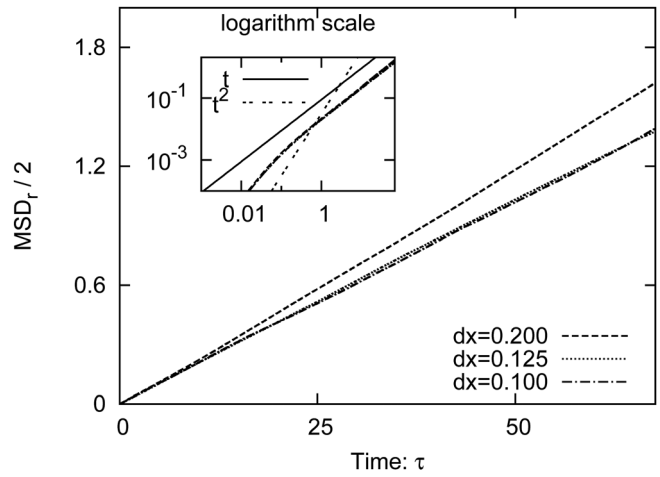

FIG. 10. Convergence of rotational mean square displacement for a disk: the slope represents the rotational diffusion coefficient in 2D; the inset shows the transition from ballistic to diffusive regime in log-log scale.

$$D = \frac{D_0}{\lambda} = \frac{k_B T}{6\pi\eta R_C \lambda}, \tag{20}$$

where λ is the drag coefficient at corresponding concentration of spheres (see Sec. III A. $\lambda \approx 2.15$ in this case).

Analytically, D is related to the translational MSD as

$$D = \frac{1}{6}\lim_{t\to\infty}\frac{d}{dt}(MSD). \tag{21}$$

In Fig. 13, we compare $D_0 t/\lambda$ with the MSD extracted from simulations in a range of sufficiently long time. The linear fit of the MSD in diffusive regime produces a diffusion coefficient with discrepancy to analytical solution smaller than 2%.

F. A colloidal particle near a rigid wall

In this section, we show the ability of the SDPD method to model a particle in the vicinity of an external boundary. The diffusion of a colloidal particle near a flat wall is hindered, as the drag coefficient λ of the particle is enhanced by the complex hydrodynamic interactions. Close to the wall, diffusion D is anisotropic[75] and, therefore, can be split into the motion parallel (along the

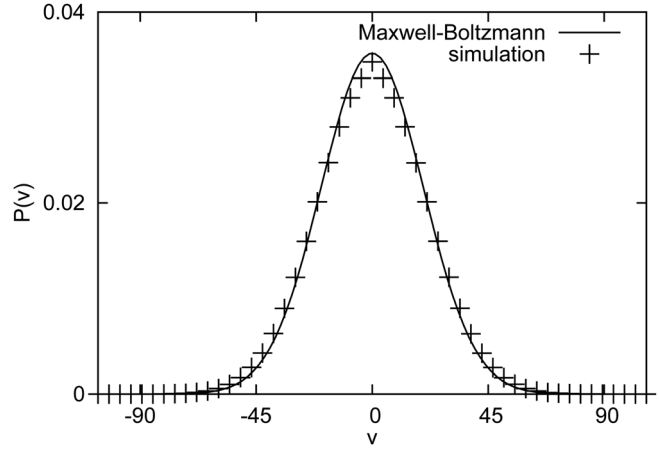

FIG. 11. Probability distribution function for velocity of solvent particles in 3D.

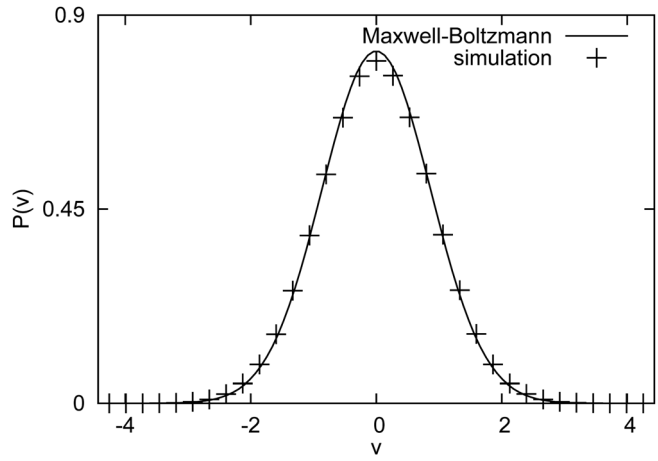

FIG. 12. Probability distribution function for velocity of a sphere in 3D.

plane x, y) and perpendicular (normal to the plane z) to the wall, with both quantities depending on the gap s between the particle surface and the wall, i.e.,

$$\begin{aligned} D_{\perp}(s) &= \frac{D_0}{\lambda_{\perp}(s)} = \frac{1}{2}\lim_{t\to\infty}\frac{d}{dt}(MSD_{\perp}(s)), \\ D_{||}(s) &= \frac{D_0}{\lambda_{||}(s)} = \frac{1}{2}\lim_{t\to\infty}\frac{d}{dt}(MSD_{||}(s)). \end{aligned} \tag{22}$$

The exact solution of $\lambda_{\perp}$ has been given as an infinite series,[76]

$$\lambda_{\perp}(s) = \frac{4}{3}\sinh\alpha\sum_{n=1}^{\infty}\frac{n(n+1)}{(2n-1)(2n+3)}\left[\frac{2\sinh(2n+1)\alpha + (2n+1)\sinh 2\alpha}{4\sinh^2(n+\frac{1}{2})\alpha - (2n+1)^2\sinh^2\alpha} - 1\right], \tag{23}$$

where $\alpha = \cosh^{-1}(1 + s/R_C)$. Without closed analytical form, the $\lambda_{||}$ approximation is derived up to fifth order using the method of reflections,[76]

$$\lambda_{||}(s) \approx 1 - \frac{9}{16}\beta + \frac{1}{8}\beta^3 - \frac{45}{256}\beta^4 - \frac{1}{16}\beta^5 + O(\beta^6), \tag{24}$$

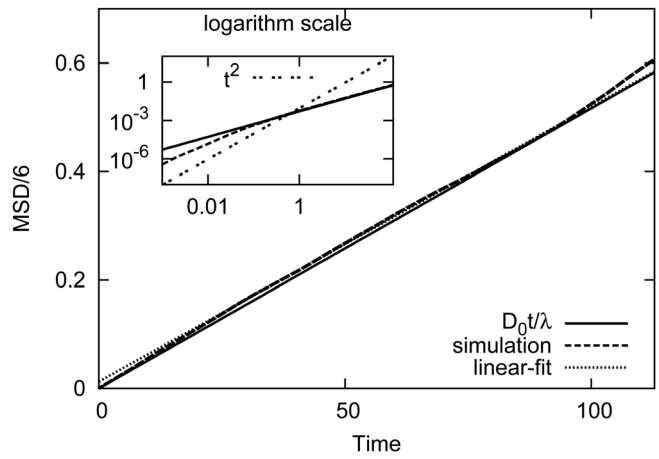

FIG. 13. Comparison of translational mean square displacement of a sphere: the slope represents the translational diffusion coefficient in 3D; the inset shows the transition from ballistic to diffusive regime in log-log scale.

where $\beta = (1 + s/R_C)^{-1}$. Both $\lambda_\perp$ and $\lambda_{||}$ show monotonic increase as the gap s decreases. However, experimental verification of such predictions has been difficult. This is mainly due to the fact that accurate $3D$ trajectories of a sub-micro-sized colloidal particle are difficult to obtain, since the particle may be out of the focal plane of microscopy at any time. Lin *et al.*[11] used optical tweezers to trap the particle location and have a control over s; Carbajal-Tinoco *et al.*[12] found a monotonic relation between the radius of the external ring of the point spread function (PSF) and s, when the fluorescent particle is out of focus. Both of the novel experiments have measured D as a function of s and corroborated the theoretical predictions of Eqs. (23) and (24).

Numerical simulations have no difficulty in this situation, since they record a complete history of the dynamics of the system. We perform a set of SDPD simulations of a sphere near a rigid wall to corroborate Eqs. (23) and (24) and experimental results, meanwhile validate our model of a colloidal particle coupled with an external boundary. A schematic system is illustrated in Fig. 14. A recent similar DPD simulation was performed for the case of a Brownian sphere diffusing between two parallel walls.[77]

Simulations parameters are taken to be the same as in Sec. III E except that the computational domain is increased to be [13, 13, 16] with periodic boundaries in x, y directions and two planar walls in z direction. No-slip boundary conditions as described in Sec. II D are applied at both walls. About 150 realizations have been computed with a spherical particle located at different initial positions Z_C along the direction z normal to the wall. Each Z_C is chosen to be in the vicinity ($Z_C <= 5$) of the bottom wall, which reduces the effect of the upper wall on the results. A post-processing procedure as described in Ref. 12 is adopted, which divides the particle trajectory for each realization into sub-trajectories. Each piece is sufficient long to capture the particle dynamics in the linear diffusive regime. Depending on the initial separations s of each sub-trajectory, ensemble averages of MSD perpendicular/parallel to the wall are calculated, from which $D_\perp(s)$ and $D_{||}(s)$ are extracted.

D_0 is known according to Eq. (19). In Fig. 15, we compare simulation results of $D(s)/D_0$ with Eqs. (23) and (24). Quantitative agreement is achieved except the region very close to the wall ($s < r_c/2$), where hydrodynamic effects can not be fully captured. The density profile using Eq. (5) for the fluid near the wall is averaged over time and shown in the inset of Fig. 15, where fluctuation near the wall is hardly observed.

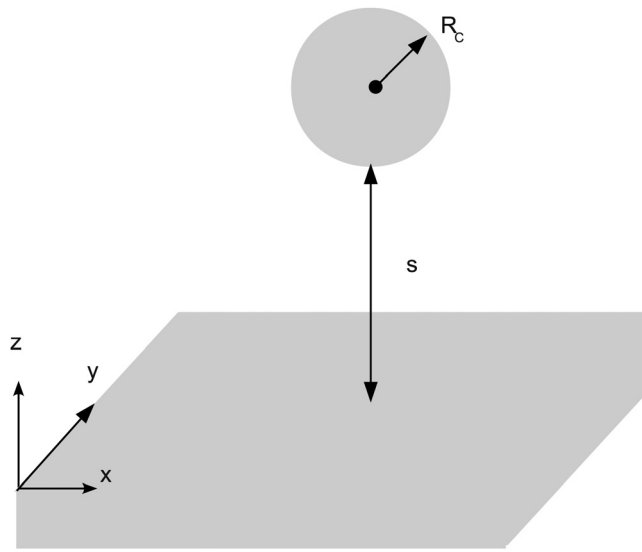

FIG. 14. Scheme of a colloidal particle moving near a rigid plane wall: periodic boundaries in x, y direction and walls in z direction; upper wall is placed sufficiently far; and the diffusion coefficient is anisotropic in perpendicular and parallel directions to the wall.

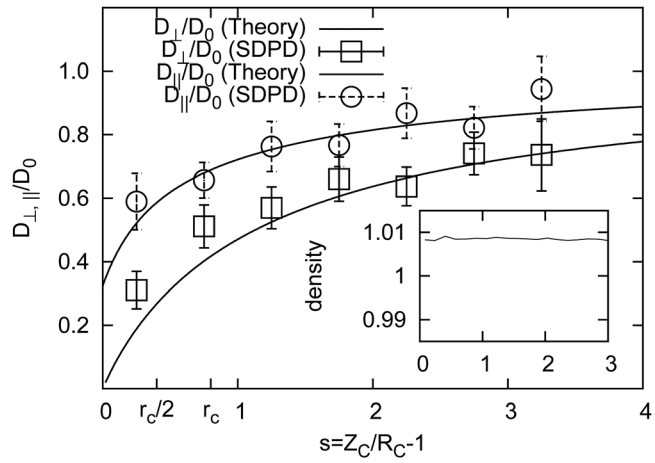

FIG. 15. Diffusion coefficients of a Brownian sphere near a rigid wall: perpendicular and parallel to the wall; the inset shows the normalized fluid density profile averaged over time near the wall.

IV. CONCLUSION

We have presented a model for solid particles in suspension using SDPD.[41] By extending the boundary condition method of Morris *et al.*,[52] particles with general shapes, with arbitrary translation and rotation, can be simulated. With regards to the numerical performance of the present SDPD model, similar to a conventional DPD, the computational cost scales linearly with the total number of suspended solid particles N_C, which is superior to $O(N_C \ln N_C)$ of the accelerated SD (Ref. 16) in number of solid particles. On the other hand, SD takes into account fluid implicitly while SDPD needs to model solvent explicitly. Moreover, the exact representation of the solid particle requires a large number of SDPD boundary particles with consequent increase of the computational cost, which is necessary for description of arbitrarily shaped solid particle. Note that the thin-layer model presented here, by reducing the number of boundary particles to only those lying within a distance r_c from the solid-liquid interface, can speed up dramatically the search of neighboring particles in the cell list, especially in the case of concentrated suspension.

A remark on the comparison of the present model with DPD is in order. The cutoff radius r_c in a SDPD simulation should be $2-4$ times bigger than a typical one used in DPD,[58] with consequent increase in the number of neighbors for each particle and CPU time. This is the price to pay to have an accurate description of the Navier-Stokes equations in the fluid domain. However, this does not prevent us to choose a smaller cutoff radius to reduce the amount of numerical operations, in which case kinetic theory or pre-run would be needed to calibrate the viscosity as in conventional DPD model.

The SDPD particle model presented here has been implemented in the parallel framework of PPM,[61] which is based on message passing interface (MPI) and has communication cost in the order of 10% of the total time by using up to 100 processors, enabling us to run realistic SDPD simulations of particle suspension. Validations ranging from diffusion-dominated regime typical of sub-micro-sized objects towards the non-Brownian regime characterizing macro-continuum flow conditions show good agreement with analytical results. Simulation of anisotropic diffusive behavior of a colloidal particle near a rigid wall has also been performed and validated by analytical solutions.

The development of a lubrication model based on extra "local" pair forces between SDPD boundary particles is currently under investigation and should allow to extend the generality of the current method to the case of concentrated suspensions of arbitrarily shaped objects.

ACKNOWLEDGMENTS

The authors would like to thank the financial support provided by the DFG (German Research Foundation) via Grant No. EL503/1-1 and appreciate discussions with X. Y. Hu and S. Adami. X.B. gratefully acknowledges the support of the TUM-Graduate School's Faculty Graduate Center

Mechanical Engineering at the Technische Universität München. 3D simulations have been mainly performed on National Supercomputer HLRB-II: *SGI Altix 4700* located at Leibniz-Rechenzentrum Garching by Munich, Germany.

[1]J. Mewis and N. J. Wagner, "Current trends in suspension rheology," J. Non-Newtonian Fluid Mech. **157**, 147 (2009).
[2]N. J. Wagner and J. Brady, "Shear thickening in colloidal dispersions," Phys. Today, **62**(10), 27 (2009).
[3]P. Tabeling, *Introduction to Microfluidics*, 2nd ed. (Oxford University Press, Oxford, 2006).
[4]G. E. Karniadakis and A. Beskok, *Microflows and Nanoflows: Fundamentals and Simulation* (Springer, New York, 2005).
[5]M. Pugia, G. Blankenstein, R. Peters, J. Profitt, K. Kadel, T. Willms, R. Sommer, H. Kuo, and L. Schulman, "Microfluidic tool box as technology platform for hand-held diagnostics," Clin. Chem. **51**, 1923 (2005).
[6]W. R. Hwang, M. A. Hulsen, and H. E. H. Meijer, "Direct simulation of particle suspensions in sliding bi-periodic frames," J. Comput. Phys. **194**, 742 (2004).
[7]R. Glowinski, T. Pan, T. Hesla, and D. Joseph, "A distributed Lagrange multiplier fictitious domain method for particulate flows," Int. J. Multiphase Flow **25**, 755 (1999).
[8]N. Patankar, P. Singh, D. Joseph, R. Glowinski, and T. Pan, "A new formulation of the distributed Lagrange multiplier/fictitious domain method for particulate flows," Int. J. Multiphase Flow **26**, 1509 (2000).
[9]Y. Nakayama and R. Yamamoto, "Simulation method to resolve hydrodynamic interactions in colloidal dispersions," Phys. Rev. E **71**, 036707 (2005).
[10]X. Luo, M. R. Maxey, and G. E. Karniadakis, "Smoothed profile method for particulate flows: Error analysis and simulations," J. Comput. Phys. **228**, 1750 (2009).
[11]B. H. Lin, J. Yu, and S. A. Rice, "Direct measurements of constrained Brownian motion of an isolated sphere between two walls," Phys. Rev. E **62**, 3909 (2000).
[12]M. D. Carbajal-Tinoco, R. Lopez-Fernandez, and J. L. Arauz-Lara, "Asymmetry in colloidal diffusion near a rigid wall," Phys. Rev. Lett. **99**, 138303 (2007).
[13]D. Ermak and J. A. McCammon, "Brownian dynamics with hydrodynamic interactions," J. Chem. Phys. **69**, 1352 (1978).
[14]L. Durlofsky, J. F. Brady, and G. Bossis, "Dynamic simulation of hydrodynamically interacting particles," J. Fluid Mech. **180**, 21 (1987).
[15]J. F. Brady and G. Bossis, "Stokesian dynamics," Annu. Rev. Fluid Mech. **20**, 111 (1988).
[16]A. Sierou and J. F. Brady, "Accelerated Stokesian dynamics simulations," J. Fluid Mech. **448**, 115 (2001).
[17]J. W. Swan and J. F. Brady, "Simulation of hydrodynamically interacting particles near a no-slip boundary," Phys. Fluids **19**, 113306 (2007).
[18]R. Kutteh, "Rigid body dynamics approach to Stokesian dynamics simulations of nonspherical particles," J. Chem. Phys. **132**, 174107 (2010).
[19]S. Weinbaum, P. Ganatos, and Z. Yang, "Numerical multipole and boundary integral-equation techniques in Stokes-flow," Annu. Rev. Fluid Mech. **22**, 275 (1990).
[20]N. Sharma and N. A. Patankar, "Direct numerical simulation of the Brownian motion of particles by using fluctuating hydrodynamic equations," J. Comput. Phys. **201**, 466 (2004).
[21]L. D. Landau and E. M. Lifshitz, *Fluid Mechanics*, 2nd ed. (Pergamon, Oxford, 1987).
[22]A. J. C. Ladd, "Numerical simulations of particulate suspensions via a discretized Boltzmann equation. Part 1. Theoretical foundation," J. Fluid Mech. **271**, 285 (1994).
[23]A. J. C. Ladd and R. Verberg, "Lattice-Boltzmann simulations of particle-fluid suspensions," J. Stat. Phys. **104**(5–6), 1191 (2001).
[24]D. L. Koch and A. J. C. Ladd, "Moderate Reynolds number flows through periodic and random arrays of aligned cylinders," J. Fluid Mech. **349**, 31 (1997).
[25]M. A. Van der Hoef, R. Beetstra, and J. A. M. Kuipers, "Lattice-Boltzmann simulations of low-Reynolds-number flow past mono- and bidisperse arrays of spheres: Results for the permeability and drag force," J. Fluid Mech. **528**, 233 (2005).
[26]C. Pan, L. Luo, and C. T. Miller, "An evaluation of lattice Boltzmann schemes for porous medium flow simulation," Comput. Fluids **35**, 898 (2006).
[27]R. S. Maier and R. S. Bernard, "Lattice-Boltzmann accuracy in pore-scale flow simulation," J. Comput. Phys. **229**, 233 (2010).
[28]T. Iwashita and R. Yamamoto, "Short-time motion of Brownian particles in a shear flow," Phys. Rev. E **79**, 031401 (2009).
[29]T. Iwashita and R. Yamamoto, "Direct numerical simulations for non-Newtonian rheology of concentrated particle dispersions," Phys. Rev. E **80**, 061402 (2009).
[30]P. J. Hoogerbrugge and J. M. V. A. Koelman, "Simulating microscopic hydrodynamics phenomena with dissipative particle dynamics," Europhys. Lett. **19**, 155 (1992).
[31]P. Español and P. Warren, "Statistical mechanics of dissipative particle dynamics," Europhys. Lett. **30**, 191 (1995).
[32]J. M. V. A. Koelman and P. J. Hoogerbrugge, "Dynamic simulations of hard-sphere suspensions under steady shear," Europhys. Lett. **21**, 363 (1993).
[33]E. S. Boek, P. V. Conveney, H. N. W. Lekkerkerker, and P. van der Schoot, "Simulating the rheology of dense colloidal suspensions using dissipative particle dynamics," Phys. Rev. E **55**, 3124 (1997).
[34]N. S. Martys, "Study of a dissipative particle dynamics based approach for modeling suspensions," J. Rheol. **49**, 401 (2005).
[35]W. Pan, B. Caswell, and G. E. Karniadakis, "Rheology, microstructure and migration in Brownian colloidal suspensions," Langmuir **26**, 133 (2009).
[36]M. Whittle and K. P. Travis, "Dynamic simulations of colloids by core-modified dissipative particle dynamics," J. Chem. Phys. **132**, 124906 (2010).
[37]C. Marsh, G. Backx, and M. Ernst, "Fokker-Planck-Boltzmann equation for dissipative particle dynamics," Europhys. Lett. **38**, 411 (1997).

[38]J. Backer, C. Lowe, H. Hoefsloot, and P. Iedema, "Combined length scales in dissipative particle dynamics," J. Chem. Phys. **123**, 114905 (2005).
[39]R. Qiao and P. He, "Mapping of dissipative particle dynamics in fluctuating hydrodynamics simulations," J. Chem. Phys. **128**, 126101 (2008).
[40]E. S. Boek and P. van der Schoot, "Resolution effects in dissipative particle dynamics simulations," Int. J. Mod. Phys. C **9**, 1307 (1998).
[41]P. Español and M. Revenga, "Smoothed dissipative particle dynamics," Phys. Rev. E **67**, 026705 (2003).
[42]M. Grmela and H. C. Öttinger, "Dynamics and thermodynamics of complex fluids. I. Development of a general formalism," Phys. Rev. E **56**, 6620 (1997).
[43]H. C. Öttinger and M. Grmela, "Dynamics and thermodynamics of complex fluids. II. Illustrations of a general formalism," Phys. Rev. E **56**, 6633 (1997).
[44]J. J. Monaghan, "Smoothed particle hydrodynamics," Annu. Rev. Astron. Astrophys. **30**, 543 (1992).
[45]J. J. Monaghan, "Smoothed particle hydrodynamics," Rep. Prog. Phys. **68**, 1703 (2005).
[46]P. Español, M. Serrano, and H. C. Öttinger, "Thermodynamically admissible form for discrete hydrodynamics," Phys. Rev. Lett. **83**, 4542 (1999).
[47]A. Vázquez-Quesada, M. Ellero, and P. Español, "Consistent scaling of thermal fluctuations in smoothed dissipative particle dynamics," J. Chem. Phys. **130**, 034901 (2009).
[48]S. Litvinov, M. Ellero, X. Y. Hu, and N. A. Adams, "Smoothed dissipative particle dynamics model for polymer molecules in suspension," Phys. Rev. E **77**, 066703 (2008).
[49]S. Litvinov, M. Ellero, X. Y. Hu, and N. A. Adams, "Particle-layering effect in wall-bounded dissipative particle dynamics," Phys. Rev. E **82**, 066704 (2010).
[50]X. Y. Hu and N. A. Adams, "A multi-phase SPH method for macroscopic and mesoscopic flows," J. Comput. Phys. **213**, 844 (2006).
[51]A. Vázquez-Quesada, M. Ellero, and P. Español, "Smoothed particle hydrodynamic model for viscoelastic fluids with thermal fluctuations," Phys. Rev. E **79**, 056707 (2009).
[52]J. P. Morris, P. J. Fox, and Y. Zhu, "Modeling low Reynolds number incompressible flows using SPH," J. Comput. Phys. **136**, 214 (1997).
[53]A. S. Khair and J. F. Brady, "Microrheology of colloidal dispersions: Shape matters," J. Rheol. **52**, 165 (2008).
[54]G. K. Batchelor, *An Introduction to Fluid Dynamics* (Cambridge University Press, Cambridge, UK, 1967).
[55]J. J. Monaghan, "Simulating free surface flows with SPH," J. Comp. Phys. **110**, 399 (1994).
[56]M. Ellero and N. A. Adams, "SPH simulations of flow around a periodic array of cylinders confined in a channel," Int. J. Numer. Methods Eng. **86**, 1027 (2011).
[57]N. J. Quinlan, M. Basa, and M. Lastiwka, "Truncation error in mesh-free particle methods," Int. J. Numer. Methods Eng. **66**, 2064 (2006).
[58]R. D. Groot and P. B. Warren, "Dissipative particle dynamics: Bridging the gap between atomistic and mesoscopic simulation," J. Chem. Phys. **107**, 4423 (1997).
[59]S. Chen, N. Phan-Thien, B. C. Khoo, and X. J. Fan, "Flow around spheres by dissipative particle dynamics," Phys. Fluids **18**, 103605 (2006).
[60]R. Courant, K. Friedrichs, and H. Lewy, "Über did partiellen Differenzengleichungen der mathematicshcen Physik," Math. Ann. **100**, 32 (1928).
[61]I. F. Sbalzarini, J. H. Walther, M. Bergdorf, S. E. Hieber, E. M. Kotsalis, and P. Koumoutsakos, "PPM—A highly efficient parallel particle-mesh library for the simulation of continuum systems," J. Comput. Phys. **215**, 566 (2006).
[62]J. T. Padding and A. A. Louis, "Hydrodynamic interactions and Brownian forces in colloidal suspensions: Coarse-graining over time and length scales," Phys. Rev. E **74**, 031402 (2006).
[63]H. Hasimoto, "On the periodic fundamental solutions of the Stokes equations and their application to viscous flow past a cubic array of spheres," J. Fluid Mech. **5**, 317 (1959).
[64]A. S. Sangani and A. Acrivos, "Slow flow past periodic array of cylinders with application to heat transfer," Int. J. Multiphase Flow **8**, 193 (1982).
[65]Y. Zhu, P. J. Fox, and J. P. Morris, "A pore-scale numerical model for flow through porous media," Int. J. Numer. Analyt. Meth. Geomech. **23**, 881 (1999).
[66]A. S. Sangani and A. Acrivos, "Slow flow through a periodic array of spheres," Int. J. Multiphase Flow **8**, 343 (1982).
[67]B. J. Alder and T. E. Wainwright, "Decay of the velocity autocorrelation function," Phys. Rev. A **1**, 18 (1970).
[68]M. H. Hagen, I. Pagonabarraga, C. P. Lowe, and D. Frenkel, "Algebraic decay of velocity fluctuations in a confined fluid," Phys. Rev. Lett. **78**, 3785 (1997).
[69]C. R. Robertson and A. Acrivos, "Low Reynolds number shear flow past a rotating circular cylinder. Part 1. Momentum transfer," J. Fluid Mech. **40**(4), 685 (1970).
[70]X. Y. Hu and N. A. Adams, "Angular-momentum conservative smoothed particle hydrodynamics for incompressible viscous flows," Phys. Fluids **18**, 101702 (2006).
[71]G. K. Batchelor, "The determination of the bulk stress in a suspension of spherical particles to order c^2," J. Fluid Mech. **56**, 401 (1972).
[72]D. J. Jeffrey and Y. Onishi, "Calculation of the resistance and mobility functions for two unequal rigid spheres in low-Reynolds-number flow," J. Fluid. Mech. **139**, 261 (1984).
[73]S. Kim and S. J. Karrila, *Microhydrodynamics: Principles and Selected Applications* (Butterworth-Heinemann, Boston, MA, 1991).
[74]N. Q. Nguyen and A. J. C. Ladd, "Lubrication corrections for lattice-Boltzmann simulations of particle suspensions," Phys. Rev. E **66**, 046708 (2002).
[75]S. Jeney, B. Lukić, J. A. Kraus, T. Franosch, and L. Forró, "Anisotropic memory effects in confined colloidal diffusion," Phys. Rev. Lett. **100**, 240604 (2008).
[76]J. Happel and H. Brenner, *Low Reynolds Number Hydrodynamics with Special Applications to Particulate Media* (Martinus Nijhoff, The Hague, 1983).
[77]Z. Li and G. Drazer, "Hydrodynamic interaction in dissipative particle dynamics," Phys. Fluids **20**, 103601 (2008).

Computer Physics Communications 185 (2014) 53–62

Contents lists available at ScienceDirect

Computer Physics Communications

journal homepage: www.elsevier.com/locate/cpc

A splitting integration scheme for the SPH simulation of concentrated particle suspensions

Xin Bian *, Marco Ellero

Lehrstuhl für Aerodynamik und Strömungsmechanik, Technische Universität München, Boltzmannstr. 15, D-85748 Garching bei München, Germany

ARTICLE INFO

Article history:
Received 26 October 2012
Received in revised form
14 June 2013
Accepted 16 August 2013
Available online 30 August 2013

Keywords:
Non-colloidal suspension
Concentrated suspension
Lubrication force
Couette flow
Smoothed particle hydrodynamics
Splitting integration
Pairwise implicit integration

ABSTRACT

Simulating nearly contacting solid particles in suspension is a challenging task due to the diverging behavior of short-range lubrication forces, which pose a serious time-step limitation for explicit integration schemes. This general difficulty limits severely the total duration of simulations of concentrated suspensions. Inspired by the ideas developed in [S. Litvinov, M. Ellero, X.Y. Hu, N.A. Adams, J. Comput. Phys. 229 (2010) 5457–5464] for the simulation of highly dissipative fluids, we propose in this work a splitting integration scheme for the direct simulation of solid particles suspended in a Newtonian liquid. The scheme separates the contributions of different forces acting on the solid particles. In particular, intermediate- and long-range multi-body hydrodynamic forces, which are computed from the discretization of the Navier–Stokes equations using the smoothed particle hydrodynamics (SPH) method, are taken into account using an explicit integration; for short-range lubrication forces, velocities of pairwise interacting solid particles are updated implicitly by sweeping over all the neighboring pairs iteratively, until convergence in the solution is obtained. By using the splitting integration, simulations can be run stably and efficiently up to very large solid particle concentrations. Moreover, the proposed scheme is not limited to the SPH method presented here, but can be easily applied to other simulation techniques employed for particulate suspensions.

1. Introduction

Particulate suspensions are used in foodstuffs, pharmaceuticals, cosmetics and intermediates in many other industrial manufacturing processes [1]. Understanding the rheological properties of such particulate material is a subject both of industrial interest and scientific importance [2,3].

Unlike experiments, numerical simulations can provide full details on the dynamics in a particulate suspension, assuming that a proper physical model is established. There are generally two mainstream directions to model a particulate suspension: in the first type of methods the suspending medium is modeled implicitly and hydrodynamic interactions are embraced in a grand resistance matrix **M** by relating velocities with forces acting on the solid particles. The most representative method in this class is Stokesian dynamics (SD) [4,5]. In the SD method, **M** has a size $6N \times 6N$, where 6 is the number of degrees of freedom for translation and rotation in three dimensions, and N is the total number of particles. The velocities of the particles at a new time step are updated implicitly by inverting **M** and afterward the positions are integrated explicitly [5]. Computational cost of SD scales well as $N \ln N$ in the accelerated version of SD [6]. However, since SD relies on the analytical solutions of the Stokes flow around spheres, it poses some difficulties to extend its application to model arbitrarily-shaped objects, non-zero particle inertia, non-periodic boundary conditions such as solid walls [7,8], as well as transient and compressible effects.

The second type of approaches represented by direct numerical simulation (DNS), where the hydrodynamic interactions between solid particles are taken into account explicitly by solving the full set of hydrodynamic equations within the fluid domain, does not suffer from the shortcomings mentioned above. This type includes extended finite element (xFEM) [9,10] and the like, lattice Boltzmann (LB) [11,12], dissipative particle dynamics (DPD) [13] and smoothed particle hydrodynamics (SPH) [14], among others. With the exception of the work of Hulsen and collaborators [9,10], where adaptive resolution is considered, limited resolution generally requires the introduction of pairwise lubrication forces between solid particles, to capture accurately the unresolved hydrodynamic interactions at very short distances. The number of operations in DNS methods usually scales linearly as $C \times N$, where C is independent of N. Nevertheless, as DNS recovers the Navier–Stokes equations for the fluid explicitly, C is usually large and related to numerical resolution. Therefore, DNS methods are often computationally more expensive than the SD method. Computational cost can be further increased in a DNS method coupled with an explicit

* Corresponding author. Tel.: +49 89 15999.
E-mail addresses: xin.z.bian@gmail.com, xin.bian@aer.mw.tum.de (X. Bian).

0010-4655/$ – see front matter © 2013 Elsevier B.V. All rights reserved.
http://dx.doi.org/10.1016/j.cpc.2013.08.015

integration scheme in the case of highly concentrated suspension,[1] where the lubrication forces are dominating and extremely small time steps must be used for stabilization.

To circumvent limitations of explicit integration in a highly concentrated suspension, Nguyen and Ladd [15] proposed in the LB method an implicit integration algorithm applied to "cluster" regions of solid particles, where each dynamic cluster is defined based on the current distances between neighboring solid particles. Thereafter, velocities in each cluster are updated implicitly and simultaneously. However, this implicit algorithm requires the proper identification of new clusters at every time step, which is a computationally expensive task and, more seriously, clusters might not be uniquely defined.

Motivated by previous work on the DPD method of highly viscous fluids [16,17], we propose here an integration scheme based on splitting of forces acting on solid particles suspended in a Newtonian fluid modeled via SPH. In particular, the dominating pairwise lubrication forces are taken into account implicitly by updating the velocities over each pair of solid particles iteratively, until a given threshold residual in the solution is reached. The remaining forces acting on the solid particles, such as multi-body SPH hydrodynamic forces and repulsive force, are integrated explicitly, as in the usual SPH scheme for the fluid. The concept of the splitting scheme is simple, effective and allows us to speed up the simulations significantly. Moreover, although the simulations presented in this work are based on SPH, no obstacles are foreseen in applying the splitting integration scheme to LB, FEM or other DNS methods, which solve hydrodynamics explicitly together with lubrication correction forces at short inter-solid-particle distances.

This work is organized as follows. In Section 2 the SPH-based model of solid particle suspension is briefly reviewed; details of the splitting integration scheme are given in Section 3; performance analysis and results of accuracy are presented in Section 4, followed by a discussion with conclusions in Section 5.

2. The SPH-based suspension model

2.1. SPH discretization of Navier–Stokes equations

In this section we briefly review the SPH formulation adopted to discretize the Navier–Stokes equations on the fluid domain. SPH is a Lagrangian meshless method in which the hydrodynamic equations are solved on a set of numerical particles advected with the local flow velocity[2] [18,19].

The continuity equation can be implemented in SPH by a discrete summation form [19]

$$d_i = \frac{1}{\mathcal{V}_i} = \frac{\rho_i}{m_i} = \sum_j W_{ij}, \qquad \dot{\mathbf{r}}_i = \mathbf{v}_i, \tag{1}$$

where d_i, $\mathcal{V}_i$, m_i, ρ_i, $\mathbf{r}_i$ and $\mathbf{v}_i$ are number density, volume, mass, mass density, position, and velocity of particle i, respectively; each particle has a constant mass m_0; $W_{ij} = W(r_{ij})$ is a bell shaped kernel function, which depends on the inter-particle distance r_{ij} and vanishes beyond a cutoff radius r_c, that is, $W_{ij} = 0$ for $r_{ij} > r_c$. In this work we use a quintic spline kernel [20]

$$f(s) = c_D \begin{cases} (3-s)^5 - 6(2-s)^5 + 15(1-s)^5, & 0 \le s < 1; \\ (3-s)^5 - 6(2-s)^5, & 1 \le s < 2; \\ (3-s)^5, & 2 \le s < 3; \\ 0, & s \ge 3, \end{cases} \tag{2}$$

where $s = r_{ij}/h = 3r_{ij}/r_c$ and h is the smoothing length of the kernel. The normalization coefficient $c_2 = 63/(478\pi {r_c}^2)$ and $c_3 = 81/(359\pi {r_c}^3)$ in two and three dimensions respectively [21]. Provided that the total number of SPH particles remains constant, total mass is exactly conserved and Eq. (1) provides an operative way to calculate the density.

For the discretization of the momentum equation in the case of viscous incompressible flow, we adopt the following formulation [14]

$$m_i \dot{\mathbf{v}}_i = -\sum_j \left(\frac{p_i}{d_i^2} + \frac{p_j}{d_j^2} \right) \frac{\partial W}{\partial r_{ij}} \mathbf{e}_{ij} + \sum_j (D+2)\eta \left(\frac{1}{d_i^2} + \frac{1}{d_j^2} \right) \frac{\partial W}{\partial r_{ij}} \frac{\mathbf{e}_{ij} \cdot \mathbf{v}_{ij}}{r_{ij}} \mathbf{e}_{ij}. \tag{3}$$

The first part on the rhs is the sum of pairwise conservative pressure force $\mathbf{F}_{ij}^C$. An equation of state relating density ρ to pressure p may be written as

$$p = p_0 \left[\left(\frac{\rho}{\rho_r} \right)^7 - 1 \right], \tag{4}$$

where p_0 (related to sound speed c_s) and ρ_r are parameters chosen based on a scale analysis [20,22], to have sufficiently small density variations. The second part on the rhs is the sum of pairwise dissipative viscous force $\mathbf{F}_{ij}^D$, which reduces relative velocity $\mathbf{v}_{ij} = \mathbf{v}_i - \mathbf{v}_j$. Dynamic viscosity η is taken constant for each particle. We take $r_c = 4.5dx$, dx being the initial distance between neighboring particles, as this choice allows us to obtain the Stokes drag acting on a solid particle with 1% accuracy according to its geometrical radius [23]. To reduce computation cost derived by the large number of neighboring particles, a smaller r_c can be used. In this case, the solution of SPH is shown to converge towards a Stokes drag characterized by a hydrodynamic radius *not equal* to the geometrical one, as usually adopted in DPD [24,25], LB [26] and other methods. However, for quantitative comparison of a non-spherical solid particle in suspension, numerical convergence towards the geometrical size would be essential.

Both $\mathbf{F}_{ij}^C$ and $\mathbf{F}_{ij}^D$ are anti-symmetric by interchanging particle indices and therefore conserve linear momentum exactly. Furthermore, both $\mathbf{F}_{ij}^C$ and $\mathbf{F}_{ij}^D$ act along the unit vector $\mathbf{e}_{ij} = \mathbf{r}_{ij}/r_{ij} = (\mathbf{r}_i - \mathbf{r}_j)/|\mathbf{r}_{ij}|$ pointing from particle j to particle i, therefore angular momentum is also strictly conserved, which is crucial for recovering the correct rotation of a solid particle under shear flow [14,27].

2.2. Suspended solid particle

Any solid particle suspended in a fluid (or any solid wall) can be modeled by collecting a group of SPH boundary particles within the solid domain. These boundary particles interact with fluid particles by means of suitable SPH forces which enforce the no-slip boundary condition at the liquid–solid interface. Initially, fluid particles are placed on a square grid and inside each spherical solid particle a new set of SPH boundary particles is created parallel to the surface as shown in Fig. 1. The distance between neighboring layers is dx as well as the distance between two neighboring particles in the same layer. This choice ensures having an approximately constant number of interpolating points also near the interface.

During the pairwise viscous force calculation $\mathbf{F}_{bf}^D$, velocity of any boundary particle b inside a solid particle α is extrapolated from its interacting fluid particle f by requiring the no-slip condition on the solid geometrical surface [14,20]. Afterward, the total force

[1] Concentration ϕ is defined as the ratio between area/volume of the solid particles and total area/volume of the suspension.

[2] Note that a numerical particle in SPH should be distinguished from a suspended solid particle: the former simply represents a Lagrangian discretization element; the latter is a physical solid grain whose model is described in Section 2.2.

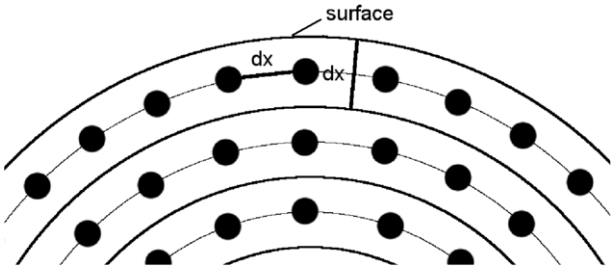

Fig. 1. Representation of a spherical solid particle: SPH frozen boundary particles are placed parallel to the surface with the same neighboring distance *dx*.

and torque exerted by the surrounding fluid on α are computed by collecting forces and torques on each b as follows [14,28],

$$\mathbf{F}_{\alpha}^{\mathrm{SPH}} = \sum_{b}\sum_{f}(\mathbf{F}_{bf}^{C} + \mathbf{F}_{bf}^{D}), \tag{5}$$

$$\mathbf{T}_{\alpha}^{\mathrm{SPH}} = \sum_{b}\sum_{f}(\mathbf{r}_{b} - \mathbf{R}_{\alpha}) \times (\mathbf{F}_{bf}^{C} + \mathbf{F}_{bf}^{D}), \tag{6}$$

where $\mathbf{r}_b$ is position of b and $\mathbf{R}_\alpha$ is center position of α. In this way, the long-range hydrodynamics is captured correctly [14].

2.3. Lubrication force correction

When two solid particles are in near contact, the flow of the liquid in the gap cannot be captured accurately due to the limited numerical resolution, therefore the hydrodynamic forces acting on them are poorly represented. One possible strategy is to increase the resolution locally within the gap until the flow is fully resolved [9,10]. However, this choice is computationally impractical, especially in the case of a concentrated suspension where many nearly-touching pairs of solid particles can be present at once. To remedy this problem, the pairwise lubrication force at short distance between solid particles is generally introduced [15,26,29,30].

In the case of SPH, when simulating two disks/spheres moving towards each other with constant velocity, the hydrodynamic force acting on them computed from the discretization of the suspending fluid deviates from the divergent behavior predicted by the theory typically at a gap distance equal to half cutoff $r_c/2$, and remains approximately constant at smaller distances [14]. For the weaker divergent shear and rotating motions of the two [31,32], the SPH solutions fail at a shorter distance of $r_c/4$ [14]. As a consequence, we use the drag force and torque computed from the SPH solutions for all three lubrication components and consider correction only for the squeezing component for those solid particles, whose surfaces are located at distances smaller than $r_c/2$. This is justified in Section 4.1 by simulating two solid particles in close proximity under shear flow.

A 2D squeezing lubrication force for two equal-sized discoidal particles is given as in Refs. [32,33]

$$\mathbf{F}_{\alpha\beta}^{lub}(s) = -\frac{\eta}{2}\mathbf{V}_{\alpha\beta}\cdot\mathbf{e}_{\alpha\beta}\left[A_1\left(\frac{2a}{s}\right)^{3/2} + A_2\left(\frac{2a}{s}\right)^{1/2}\right]\mathbf{e}_{\alpha\beta}, \tag{7}$$

where $A_1 = \frac{3}{4}\pi\sqrt{2} = 3.3322, A_2 = \frac{231}{80}\pi\sqrt{2} = 12.829$; each solid particle has the same radius a and s is the separation distance between the surfaces of solid particle α and β; $\mathbf{V}_{\alpha\beta}\cdot\mathbf{e}_{\alpha\beta}$ is the component of velocity difference along the center-to-center line. Similar to the case in three dimensions [31,12,34,3], Eq. (7) implies that if α and β move towards each other along $\mathbf{e}_{\alpha\beta}$ with a constant $V_{\alpha\beta}$, they experience a repulsive viscous force $F_{\alpha\beta}^{lub}(s)$ and its value monotonically increases to infinity as $s \to 0$, as shown in Fig. 2; $F_{\alpha\beta}^{lub}(s)$ is completely reversible and becomes attractive when α and β move apart along $\mathbf{e}_{\alpha\beta}$.

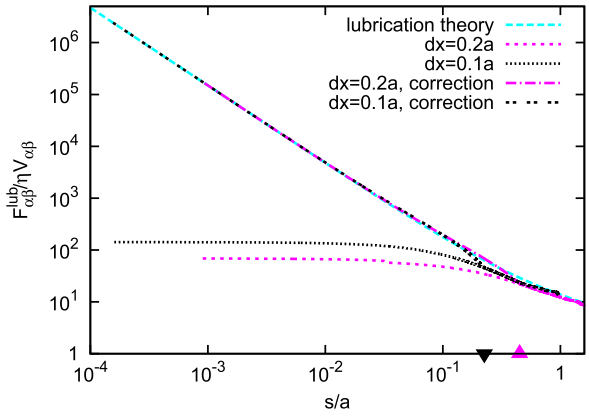

Fig. 2. Lubrication force $F_{\alpha\beta}^{lub}$ for two disks moving towards each other with constant $V_{\alpha\beta}$ along center-to-center line $\mathbf{e}_{\alpha\beta}$: theory is according to Eq. (7); SPH results before and after correction using Eq. (8); ▲: $s_c = r_c/2 = 0.45a$ for $dx = 0.2a$; ▼: $s_c = r_c/2 = 0.225a$ for $dx = 0.1a$.

As mentioned above, the hydrodynamic force in the $\mathbf{e}_{\alpha\beta}$ direction obtained by the SPH solution remains almost constant for $s < s_c = r_c/2$. This contribution should not be present when the analytical solution Eq. (7) is applied at short distances, therefore, we introduce a shifted force $\mathbf{F}_{\alpha\beta}^{lub\_cor}$ to correct the lubrication force in SPH

$$\mathbf{F}_{\alpha\beta}^{lub\_cor}(s) = \begin{cases} \mathbf{F}_{\alpha\beta}^{lub}(s) - \mathbf{F}_{\alpha\beta}^{lub}(s_c), & s < s_c; \\ 0, & s \geq s_c. \end{cases} \tag{8}$$

For the typical SPH resolutions $dx = 0.2a$ and $0.1a$ considered in this work, $s_c = r_c/2 = 0.45a$ and $0.225a$. Corrected with Eq. (8) SPH simulations reproduce quite well the short-range hydrodynamics according to Eq. (7), as shown in Fig. 2. Note again that, the forces being such that $\mathbf{F}_{\alpha\beta}^{lub\_cor} = -\mathbf{F}_{\beta\alpha}^{lub\_cor}$ and acting along $\mathbf{e}_{\alpha\beta}$, both linear and angular momenta are strictly conserved. It has been proved [35–39,30] that the most divergent lubrication component along $\mathbf{e}_{\alpha\beta}$ alone captures the essential physics and produces correctly the dynamics and rheology of a multiple-solid-particles suspension under shear flow.

2.4. Short-range repulsive force

It is commonly acknowledged that an ideal non-Brownian concentrated particulate suspension under shear flow is a singular problem [35,36,40,41], that is, the distance between neighboring solid particles is getting indefinitely smaller along the compression axis and there is no steady state under shear flow. In a real suspension, Brownian forces, excluded volume effects and surface roughness would prevent unphysical overlap between solid particles. Therefore, in numerical simulations a very short-range repulsive force is usually introduced to stabilize an ideal non-Brownian suspension. The specific form of the repulsive force is not crucial as long as it is stiff [40]. In this work we adopt a Derjaguin–Landau–Verwey–Overbeek type which reads [42,40,41],

$$\mathbf{F}_{\alpha\beta}^{rep}(s) = F_0\frac{\tau e^{-\tau s}}{1 - e^{-\tau s}}\mathbf{e}_{\alpha\beta}, \tag{9}$$

where $\tau^{-1} = 0.01a$ sets the active range and $|F_0|$ sets the magnitude. As $\mathbf{F}_{\alpha\beta}^{rep} = -\mathbf{F}_{\beta\alpha}^{rep}$ and they act along $\mathbf{e}_{\alpha\beta}$, both linear and angular momenta are always conserved.

3. Splitting integration scheme

To update the positions/velocities of the SPH fluid particles, a modified explicit velocity Verlet algorithm is used [43]. To maintain the numerical stability of the explicit time-integrator, time-step size Δt must be restricted by three conditions:

1. $\Delta t \leq 0.125h^2/\nu$: viscous constraint [20];
2. $\Delta t \leq 0.25h/c_s$: Courant–Friedrichs–Lewy condition [44];
3. $\Delta t \leq 0.25\min\sqrt{(h/f_s)}$: maximum fluid particle acceleration [20],

where the kinematic viscosity $\nu = \eta/\rho$; c_s is the fluid speed of sound; f_s is acceleration acting on any fluid particle.

For each solid particle α, the total force and torque acting on it are

$$\mathbf{F}_\alpha = \mathbf{F}_\alpha^{\mathrm{SPH}} + \sum_{\beta\neq\alpha}\mathbf{F}_{\alpha\beta}^{lub\_cor} + \sum_{\beta\neq\alpha}\mathbf{F}_{\alpha\beta}^{rep},$$

$$\mathbf{T}_\alpha = \mathbf{T}_\alpha^{\mathrm{SPH}}. \tag{10}$$

To integrate the previous set of ordinary differential equations we have first followed Ref. [14] and used both the Euler and modified velocity Verlet *explicit* integration schemes, which work properly under conditions of dilute or semi-dilute concentration. However, as the number of solid particles increases, near-contact encounters become extremely frequent and the lubrication term $\sum_{\beta\neq\alpha}\mathbf{F}_{\alpha\beta}^{lub\_cor}$ represents the dominating force contribution. For a stable explicit integration of the velocities and positions of the solid particles, either an adaptive time step scheme constrained by the maximum acceleration of the solid particle, i.e., $\Delta t_{sub} \leq 0.25\min\sqrt{(h/f_\alpha)}$, or a sub-time-step scheme, i.e., $\Delta t_{sub} = \Delta t/N_{sub}$, has to be used. In both cases, when simulating solid particle concentrations exceeding 40%, Δt_{sub} needs to be generally up to 10^2–10^3 times smaller than the Δt used for the fluid, making the simulation practically unfeasible. When simulating $\phi = 68.7\%$, the simulation becomes unstable and the run blows up rapidly, even at the smallest time step Δt_{sub} adopted.

In this section we present a strategy for the stable time-integration of solid-particles quantities: to update the velocity and position of each solid particle from time step n to $n+1$, we *split* the force contributions into different parts. In particular, for each solid particle α, we first update its velocity according to the SPH force explicitly as

$$\mathbf{V}'_\alpha = \mathbf{V}_\alpha^n + \mathbf{F}_\alpha^{\mathrm{SPH}}\Delta t/m_\alpha, \tag{11}$$

where m_α is the mass of α. This integration of velocities for solid particles is comparably stable to that used for the fluid particles.

In a second stage we consider the integration of the dominant short-range lubrication forces. Due to their pairwise nature, it is possible to apply the general ideas discussed in Ref. [16] for the integration of DPD equations for highly viscous fluids. In particular, we consider the lubrication contribution by sweeping over all pairs of neighboring solid particles over a certain number of iterations N_{sweep}. Accordingly, an iterative sub-time step $\Delta t_{sweep} = \Delta t/N_{sweep}$ is introduced. For each pair of solid particles α and β, their velocities are updated simultaneously and implicitly as follows

$$\begin{aligned}\tilde{\mathbf{V}}_\alpha &= \mathbf{V}'_\alpha + \tilde{\mathbf{F}}_{\alpha\beta}^{lub\_cor}\Delta t_{sweep}/m_\alpha,\\ \tilde{\mathbf{V}}_\beta &= \mathbf{V}'_\beta - \tilde{\mathbf{F}}_{\alpha\beta}^{lub\_cor}\Delta t_{sweep}/m_\beta,\end{aligned} \tag{12}$$

where $\tilde{\mathbf{F}}_{\alpha\beta}^{lub\_cor}$ is a linear function of $\tilde{\mathbf{V}}_\alpha$ and $\tilde{\mathbf{V}}_\beta$. Being this small system of equations (4 equations in 2D, 6 equations in 3D) linear in the particle velocities, no numerical inversion of the matrix is needed and one can solve it analytically using any algebra software (see the Appendix). Afterward, the resulting expression can be directly implemented in the code and Eq. (12) is solved for each pair N_{sweep} times over each Δt.

After N_{sweep} times of sweeping for the lubrication forces, we consider the contribution from the repulsive force. Being that the repulsive force is only position-dependent, we use a Verlet scheme. For each solid particle α,

$$\mathbf{V}_\alpha^{n+1/2} = \tilde{\mathbf{V}}_\alpha + \frac{1}{2}\mathbf{F}_\alpha^{rep,n}\Delta t/m_\alpha, \tag{13}$$

Table 1
Integration of 2D lubrication force for one sub-step: explicit vs. implicit.

Line	Explicit	Count	Pairwise implicit	Count
1	DO $\alpha = 1, N-1$		DO $\alpha = 1, N-1$	
2	DO $\beta = \alpha+1, N$		DO $\beta = \alpha+1, N$	
3	IF $(s_{\alpha\beta} < s_c)$	6	IF $(s_{\alpha\beta} < s_c)$	6
4	$F_{\alpha\beta} = F_{\alpha\beta}^{lub\_cor}(s_{\alpha\beta})$	25	Solve Eq. (12)	
5	$F_\alpha = F_\alpha + F_{\alpha\beta}$	1	Implicitly	
6	$F_\beta = F_\beta - F_{\alpha\beta}$	1	(See Appendix)	82
7	END IF		END IF	
8	END DO		END DO	
9	END DO		END DO	
10				
11	DO $\alpha = 1, N_p$			
12	$V_\alpha += F_\alpha\Delta t_{sub}/m_\alpha$	3	–	0
13	END DO			

where $\mathbf{F}_\alpha^{rep,n} = \sum_{\beta\neq\alpha}\mathbf{F}_{\alpha\beta}^{rep,n}$ is the total repulsive force on α exerted by the other solid particles with positions at time step n. The new position at time step $n+1$ is updated as

$$\mathbf{R}_\alpha^{n+1} = \mathbf{R}_\alpha^n + \mathbf{V}_\alpha^{n+1/2}\Delta t. \tag{14}$$

Finally, we obtain the velocity at the new time step as

$$\mathbf{V}_\alpha^{n+1} = \mathbf{V}_\alpha^{n+1/2} + \frac{1}{2}\mathbf{F}_\alpha^{rep,n+1}\Delta t/m_\alpha, \tag{15}$$

where $\mathbf{F}_\alpha^{rep,n+1} = \sum_{\beta\neq\alpha}\mathbf{F}_{\alpha\beta}^{rep,n+1}$ is the total repulsive force on α from other solid particles with positions at time step $n+1$.

A remark about the number of implicit sweeps N_{sweep} for the lubrication contribution is in order here. We use an adaptive criterion similar to Ref. [45]. At the time step n, we perform one default number of sweeps $N_{sweep} = 2^m$ and another one with $N'_{sweep} = 2^{m-1}$. Then we use a non-dimensionalized L_2 norm $e^m = \frac{\sqrt{\sum_{\alpha=1}^N (V_\alpha^m - V_\alpha^{m-1})^2}}{\sqrt{\sum_{\alpha=1}^N (V_\alpha^m)^2}}$ to measure velocity difference between the two solutions obtained. On the one hand, if $e^m < \epsilon$ (a pre-defined tolerance), we half the number of sweeps q times until $e^{m-q} \geq \epsilon$ or $2^{m-q-1} = 1$ and we use the solution obtained with $N_{sweep} = 2^{m-q+1}$ which becomes the default number of sweeps at the next time step $n+1$; on the other hand, if the residual $e^m > \epsilon$, we double the number of sweeps q times until $e^{m+q} < \epsilon$ or 2^{m+q} reaches a pre-defined maximum number of sweeps and we use the solution obtained with 2^{m+q} sweeps, this being the default number of sweeps at the next time step $n+1$.

3.1. Algorithm complexity

Whether we adopt an explicit or implicit integration for the lubrication forces, the rest of the numerical operations, such as operations on SPH fluid, are identical. Therefore, we only focus on the analysis of complexity on integrating velocities using lubrication forces. The complexity details of each algorithm are listed in Table 1, where we count $+, -, \times, \div$ each as one floating-point operation and $()^{power}$ as three.

To search for neighboring particles, $N(N-1)/2$ pairs have to be checked as in lines 1 and 2 for both explicit and pairwise implicit methods. For calculating gap distance $s_{\alpha\beta}$ we need 6 operations. The calculation of lines 4–6 depends on the actual number of neighbors N_{neigh} in simulations, which, for example, is $N_{neigh} \approx 3$ for $\phi = 58.9\%$ (see Section 4.2.1). Additional lines 11–13 are performed in explicit integration for updating velocity in a separate loop. As the only difference lies in lines 4–6, and 11–13, we compare these parts literally, using $\phi = 58.9\%$ as an example, where for the explicit method the count is $(27N \times N_{neigh} + 3N) \times N_{sub} = 84N \times N_{sub}$; and for pairwise implicit the count is $(82N \times N_{neigh}) \times N_{sweep} = 246N \times N_{sweep}$.

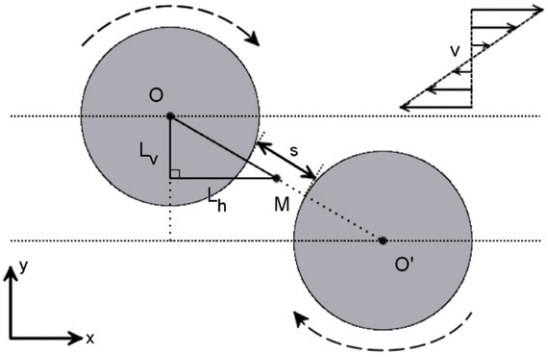

Fig. 3. Two rotating solid particles under shear flow: shear flow is clock-wise. M is middle point of the two particles. L_h, L_v are horizontal and vertical distances of the two to M. s is the surface distance.

Therefore, to compare the computational costs of pairwise implicit and explicit integration of lubrication forces, it further relies on the comparison of the number of implicit sweeps N_{sweep} and number of explicit sub-time-steps N_{sub}. It is clear that as long as $3N_{sweep} \lessapprox N_{sub}$ the splitting integration would be faster than the purely explicit integration.

Note that in 3D the number of operations increases 1.5 times for the explicit scheme and $1.5^2 = 2.25$ times for the pairwise implicit scheme. The small relative factor $2.25/1.5 = 1.5$ would not play a role and conclusions drawn from the following 2D simulations shall be retained in 3D.

4. Numerical results

To validate the suspension model with the proposed integration schemes, we perform simulations of suspensions confined between two parallel walls under constant shear flow. The first test case discussed in Section 4.1 is represented by the problem of two hydrodynamically interacting and rotating solid particles, where analytical solutions are available. In Section 4.2, a numerical analysis on the performance and accuracy of the implicit integration scheme is carried out for a multiple-solid-particles suspension. Thereafter, effective viscosity and microstructure of the suspension are presented and compared with that of the explicit scheme and references.

4.1. Two-solid-particles dynamics under shear flow

In this section we consider the dynamics of two interacting solid particles immersed in a liquid undergoing a steady shear flow. The sketch of the problem is provided in Fig. 3. The corresponding Stokes flow has been solved analytically. In particular, in two dimensions the analytical expressions for the trajectories of two neutrally buoyant particles have been given in Ref. [46]. Depending on the initial separation L_h and L_v, the trajectory of the two particles can be either open or closed [46,47].

To solve the problem numerically, we take two equal-sized solid particles with radius $a = 1$ and define a simulation box of size $L_x = L_y = 40$, with periodic boundary conditions applied to the x direction and solid walls placed at $y = 0$ and L_y. This choice of box size is sufficient to minimize the effects of the walls and the periodic images on the dynamics. The upper and bottom walls move in opposite directions with velocity magnitude $|v_0| = 2.115$, which defines a clock-wise shear rate $\dot{\gamma} = 2|v_0|/L_y = 0.10575$. The fluid viscosity $\eta = 8.46$, and density $\rho = 1.0$, defines a particle Reynolds number $\mathrm{Re}_p = \dot{\gamma}a^2\rho/\eta = 0.0125$. The sound speed is chosen as $c_s = 50$, which restricts density variations to well below 1% during simulations.

The middle point $M(x_M, y_M)$ of the two solid particles is at the center of the computational box as shown in Fig. 3. The initial horizontal and vertical distances of the two to M are L_h and L_v, respectively. We perform simulations with 4 initial configurations $[L_h = 1.5, L_v = 1.0]$, $[L_h = 1.5, L_v = 0.6]$, $[L_h = 1.2, L_v = 0.0]$ and $[L_h = 1.1, L_v = 0.0]$, and with two resolutions $dx = 0.2$ and $dx = 0.1$.

Relative positions and distances of the two solid particles are shown in Fig. 4, where simulations are compared with analytical solutions. Due to symmetry, two particles always have synchronized rotation and translation. When the two particles are aligned in the y direction, they have the minimum surface distance $s_{\min}$ [46]. If $s_{\min}/2 \leq 0.1$, the maximum distance of the two is bound and they have closed trajectory forming a permanent doublet. Otherwise, the trajectories are open and going to infinity. Due to limited resolutions, lubrication correction is switched on in SPH whenever surface distance $s < r_c/2$. Therefore, for $dx = 0.2$ and 0.1 simulations are with lubrication correction forces when $OM/a < 1.225$ and 1.1125 respectively (Fig. 4, right plot). Results produced by two different resolutions are very similar and agree well with analytical solutions. The whole scenario of two solid particles under shear flow is captured well by SPH simulations with lubrication corrections.

The same simulations have been previously performed using the LB method [33]. However, no comparison with 2D analytical solutions was done nor closed trajectories were shown, which is a fundamental step towards simulating multiple-solid-particles suspension.

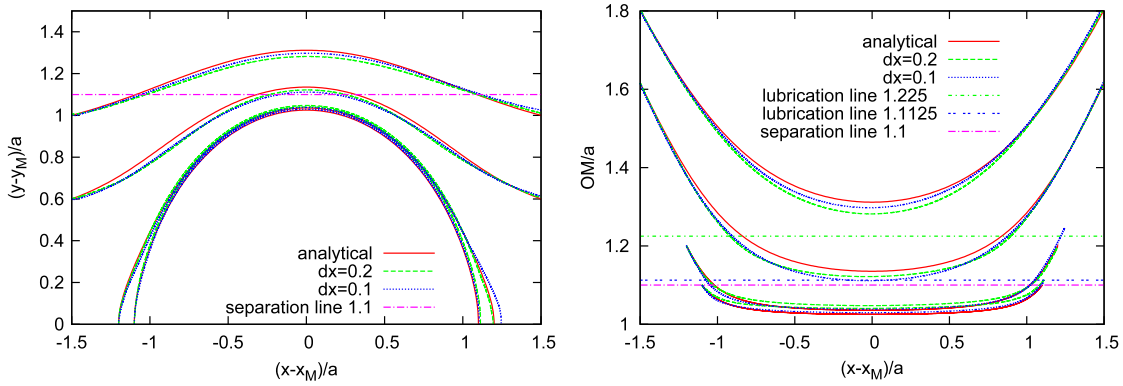

Fig. 4. Relative position (left) and distance (right) of two solid particles to the center of mass M under shear flow ($r_c = 4.5dx$ with the proposed splitting integration scheme): $O'M = OM = \sqrt{(x - x_M)^2 + (y - y_M)^2}$. For $dx = 0.2$, lubrication correction is switched on when $OM/a < 1.225$; for $dx = 0.1$, lubrication correction is switched on when $OM/a < 1.1125$. 1.1 is the separation line between closed and open trajectories. Due to the nature of Stokes flow, the paths and distances are symmetrical in x, y direction.
Source: Analytical solutions are taken from Ref. [46].

Table 2
Computation box [16, 16], implicit tolerance $\epsilon = 10^{-3}$: comparison of run time (wall time) for the same physical time $T = 1330$ in simulations (according to $10^6 \Delta t$ and Δt is SPH fluid time step); simulation code is implemented in Fortran 99 and compiled with ifort 11.1 on Intel Xeon CPU E5410@2.33 GHz.

N	ϕ	Implicit $\overline{N}_{sweep}$	Run time (h)	Explicit[a] N_{sub}	Run time (h)	$\overline{N}_{neigh}^{r=2.45}$
8	9.8%	1.00		1		
16	19.6%	1.01		1		
24	29.5%	1.28		1		
32	39.3%	3.01	29.3	32	48.4	1.83
40	49.1%	10.02	34.7	128	87.1	2.59
48	58.9%	27.53	43.3	1024	340.7	3.28
56	68.7%	78.81	54.5	–	–	4.05

[a] Explicit N_{sub} is initially set to be 1 and doubled until a stable simulation with a convergent shear stress is achieved.

4.2. Multiple-solid-particles suspension under shear flow

When more solid particles are considered, the suspension becomes semi-dilute or even concentrated and an extremely small time step is necessary for integrating the dynamics explicitly. To be computationally practical, an implicit scheme for the integration of the solid particles dynamics in a concentrated suspension is preferred.

In the first part of this section the performance of the proposed splitting scheme is evaluated, which takes into account different force contributions either explicitly or implicitly. In particular, we focus on the pairwise implicit part, which due to the requirement $N_{sweep} > 1$ dominates the integration costs for the solid particles. In the second part, the physical results of the multiple-solid-particles suspension under shear flow are discussed.

4.2.1. Tolerance and number of implicit sweeps for the lubrication force

Taking the same parameters for the fluid and solid particles as in Section 4.1, we choose a computational box as $[L_x, L_y] = [16, 16]$ and suspend a different number of solid particles randomly to span over different concentrations as given in Table 2. The lubrication correction force is active whenever the inter-solid-particle gap s is smaller than $r_c/2$. Repulsive force is active with $F_0 = 0.894645$ and $\tau^{-1} = 0.01$ to prevent overlap or contact of particles. All simulations start with $N_{sweep} = 2$ at time step $n = 0$.

For all the SPH simulations, we analyze the features of the splitting scheme, particularly the pairwise implicit part, to understand its performance. A typical concentrated suspension with $\phi = 58.9\%$ is considered, corresponding to the snapshot shown in Fig. 5. The conclusions drawn are similarly applicable to other concentrations. Note the intentionally adopted under-resolved flow between solid particles in Fig. 5, where solvent liquid contained in specific inter-solid-particle gaps is reproduced only by a few SPH fluid particles and its effect on the solid grains is implicitly taken into account by the lubrication model (Section 2.3). Note also that at the resolution considered, lubrication forces capture accurately the inter-solid-particle dynamics as discussed in detail in Fig. 4 (Section 4.1).

For small values of the tolerance ϵ, an increasingly large number of sweeps N_{sweep} (with consequent computational effort) is necessary: the time history of N_{sweep} for different tolerances ϵ is shown in Fig. 6(a), where for $\phi = 58.9\%$ one order of magnitude reduction in the tolerance requires approximately ten times larger number of sweeps. Furthermore, the effect of different tolerances on the iteration convergence is also studied for simulations at other concentrations, confirming the increase of computational cost for smaller tolerances. Therefore, it is very important to select carefully the value of ϵ, namely sufficiently small to enforce accuracy, yet not too small to avoid unnecessary computational cost.

Effective viscosity of the suspension is an important rheological quantity and a useful guideline to determine the tolerance. The instantaneous viscosity $\eta_s(t)$ of the suspension is defined as the ratio of the instantaneous shear stress on the wall and the shear rate. The constant effective suspension viscosity η_s is therefore obtained by averaging $\eta_s(t)$ over 3 million steps after steady state, to reduce the statistical error. We measure η_s and compare it for different tolerances, as shown in Fig. 6(b). It is clear that a certain number of sweeps corresponding to a tolerance $\epsilon = 10^{-3}$ is sufficient for converged results. Accordingly, we use $\epsilon = 10^{-3}$ as standard tolerance for all simulations performed. For a qualitative rather than quantitative study, $\epsilon = 10^{-2}$ would be still sufficient, which requires only a couple of sweeps in the algorithm to run stably. Note that errors in this case (with respect to the converged viscosity values) are below 5% at the largest concentration and even smaller otherwise.

Time averaged numbers of implicit sweeps with $\epsilon = 10^{-3}$ are compared with the number of explicit sub-time-steps N_{sub} for all concentrations in Table 2: N_{sub} is significantly larger than $\overline{N}_{sweep}$ for non-dilute concentrations. For example, in the case $\phi = 58.9\%$ only $\overline{N}_{sweep} = 27.5$ are necessary which gives an estimate $3\overline{N}_{sweep} = 82.5 \ll N_{sub} = 1024$ (see Section 3.1), with a potential speed-up factor bigger than 10. Taking into account the cost of SPH calculations, the total run time of the simulation for $\phi = 58.9\%$ using the splitting scheme is ∼8 times faster than the one using the purely explicit scheme, as shown in Table 2. In addition, for a qualitative result we may use $\epsilon = 10^{-2}$, leading to $\overline{N}_{sweep} = 1.6$, as shown in Fig. 6(a), which is much superior to the purely explicit scheme for a stable simulation. More importantly, the simulation at $\phi = 68.7\%$ ran stably using the splitting scheme with a practical computational cost, whereas it is unfeasible by using explicit schemes even by choosing $N_{sub} = 1024$.

Being that the pairwise repulsive force $F_{\alpha\beta}^{rep}(s)$ is stiff and rapidly decaying towards the value $0.01|F_0|\tau$ for $s \to 5\tau^{-1}$, it is switched-on only when $s \leq 0.05$. From the history of the number of neighbors per solid particle shown in Fig. 6(c), it can be evinced that active repulsion is indeed a rare event compared to lubrication: because $\overline{N}_{neigh}^{r=2.45} \approx 3 > 1$, updating positions/velocities of a pair interacting via lubrication force *involves* other pairs, which leads to the explicit integration being rather unstable. Nevertheless, this issue is solved iteratively by the pairwise implicit scheme. In contrast: $\overline{N}_{neigh}^{r=2.05} \approx 1$ means that a repulsive pair is isolated from others, and therefore can be handled by the explicit Verlet scheme. Neither does the number of neighbors N_{neigh} per solid particle change for different tolerances ($\epsilon = 10^{-4}, 10^{-2}$) studied, nor for larger systems (i.e. $N = 192$, $\phi = 58.9\%$ in the box [32, 32]), but it depends only on the concentration ϕ, which determines the final number of numerical operations. The time averaged N_{neigh} at the steady state is shown for comparison in Tables 2 and 3 for different system sizes.

Another important issue concerns the dependence of the iteration convergence on the system size. Indeed, the implicit scheme being based on a pairwise velocities update performed over all the solid particles in the system, it is *a priori* not clear how the number of sweeps changes with different system size. Therefore, we

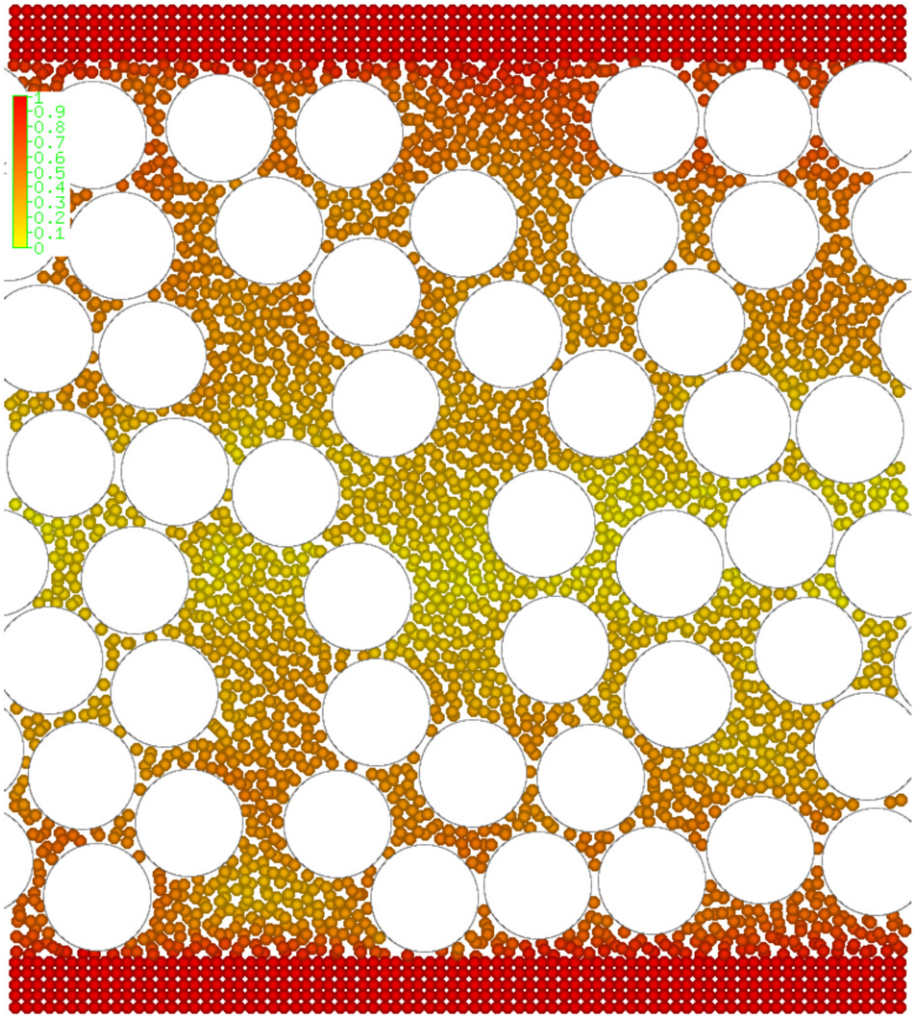

Fig. 5. Snapshot of a particulate suspension confined by parallel walls: size of computational box is [16, 16], $a = 1$, $dx = 0.2$, $N = 48$, and $\phi = 58.9\%$; two walls move with $|v_0| = 0.846$ in opposite directions, $\dot{\gamma} = 0.10575$ and $\mathrm{Re}_p = 0.0125$; solid particles are represented by circles; fluid particles are marked with color indicating magnitude of the velocity field normalized by $|v_0|$, being generally higher near the wall and lower in the center.

Table 3
Computation box [32, 32], implicit tolerance $\epsilon = 10^{-3}$.

N	ϕ	Implicit $\overline{N}_{sweep}$	$\overline{N}_{neigh}^{r=2.45}$
32	9.8%	1.00	
64	19.6%	1.00	
96	29.5%	1.00	
128	39.3%	1.05	1.72
160	49.1%	3.40	2.53
192	58.9%	10.71	3.33
224	68.7%	31.60	4.10

perform the simulations again with $\epsilon = 10^{-3}$ in a bigger computational box $[L_x, L_y] = [32, 32]$ for each concentration, corresponding to a number of simulated solid particles in the range $N \in [32 - 224]$. A positive outcome is that $\overline{N}_{sweep}$ for a fixed ϕ does not increase from system [16, 16] to [32, 32], as shown in Tables 2 and 3.

To summarize the results of this section: the pairwise implicit scheme performs better than the explicit scheme, specifically for large concentrations ϕ. The number of implicit sweeps N_{sweep} does not increase with system size, which makes the algorithm straightforwardly applicable to big systems of solid particles.

4.2.2. Viscosity and microstructure

Having demonstrated the superior computational performance of the splitting scheme over the explicit one in the previous section, we proceed here by comparing the physical results extracted in the two cases. Effective viscosities for different concentrations are calculated for both purely explicit integration scheme and splitting integration scheme. The purely explicit scheme is able to simulate up to $\phi = 58.9\%$, but it fails to run $\phi = 68.7\%$ stably with a practical cost. Results of SPH simulations using different integration schemes are compared in Fig. 7, where the empirical Krieger–Dougherty formula [48]

$$\frac{\eta_s}{\eta} = \left(1 - \frac{\phi}{\phi_{\max}}\right)^{-[\eta]\phi_{\max}} \tag{16}$$

for the suspension viscosity is also shown. A maximum packing fraction of disks on a square lattice $\phi_{\max} = \pi/4 = 78.5\%$ and the intrinsic viscosity parameter $[\eta] = 2$ in two dimensions are assumed. The SPH results fit Eq. (16) nicely up to $\phi = 58.9\%$ for both the explicit and the splitting schemes in computational box [16, 16], proving the consistency of the results from the two integration schemes. Note that due to effects of limited box size, the viscosity of $\phi = 58.9\%$ and 68.7% converges in the two bigger simulation boxes. At $\phi = 68.7\%$, one may still notice a small discrepancy between SPH results and Eq. (16). However, the disagreement at very high concentration is generally present from different Refs. [42,49,50,6], as the suspension in this case is close to jamming transition and its viscosity is very sensitive to details, such as surface roughness of solid particles, wall slip, and non-hydrodynamic forces in short range.

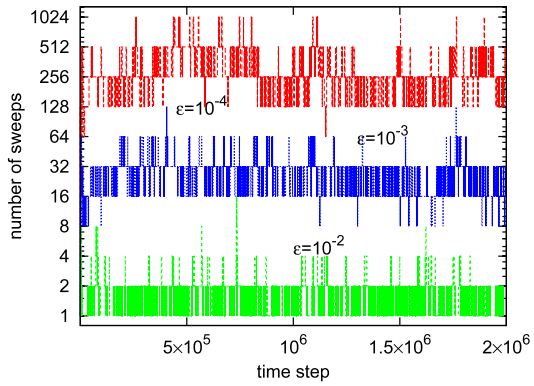

(a) Time history of sweeps for $N = 48$, $\phi = 58.9\%$ with different tolerances ϵ.

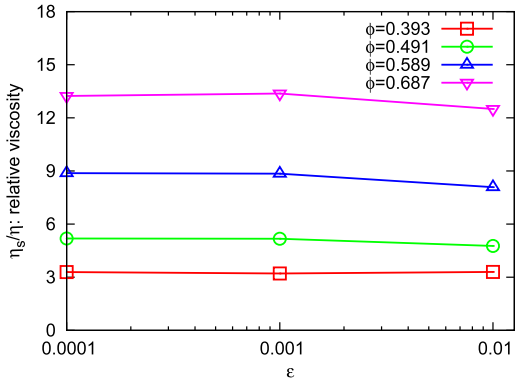

(b) Measured viscosity for different concentrations and tolerances.

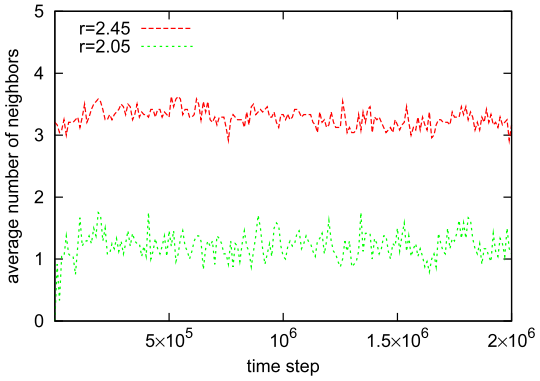

(c) Time history of neighbors N_{neigh} for $N = 48$, $\phi = 58.9\%$, $\epsilon = 10^3$: $r = 2.45$ indicates switched-on of the lubrication correction for $dx = 0.2$; $r = 2.05$ indicates switched-on of the repulsive force ($F^{rep}_{\alpha\beta}(s)$ decays below $0.01|F_0|\tau$ beyond $5\tau^{-1} = 0.05$).

Fig. 6. Numerical performance of the splitting scheme for a computational box [16, 16].

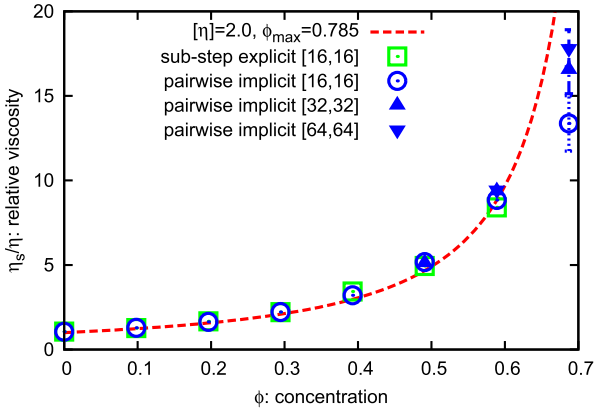

Fig. 7. Viscosity versus solid particles concentration: ⊡: explicit integration with sub-time-step in box [16, 16]; ⊙: splitting integration in box [16, 16]; ▲: splitting integration in box [32, 32]; ▼: splitting integration in box [64, 64]. ⊡ leads to $O(10^3)$ sub-time-steps for $\phi = 58.9\%$ and are unstable for $\phi = 68.7\%$; N and $\overline{N}_{sweep}$ for ⊙ and ▲ are shown in Tables 2 and 3; In box [64, 64], $N = 768$ and 896, $\overline{N}_{sweep} = 3.94$ and 10.56 for $\phi = 58.9\%$ and 68.7% respectively. If error bars on SPH results are smaller than the size of the symbols, they are not shown.

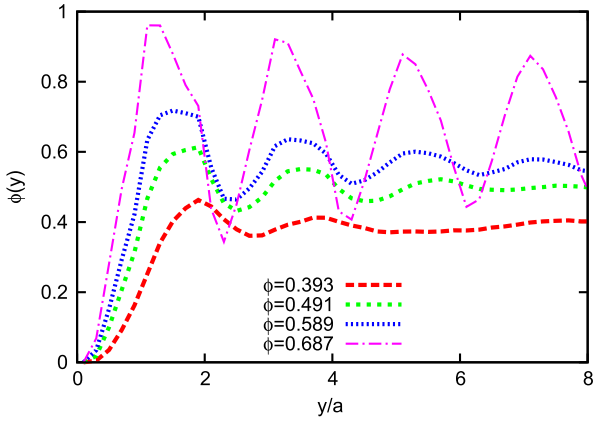

Fig. 8. Concentration profiles of solid particles in box [16, 16]: half of the channel is shown due to symmetry; for higher concentration, layering is more pronounced and the first peak is closer to the wall.

A similar computational work has recently been performed in 3D using the force-coupling method (FCM) [51], where possible wall effects are studied. Taking into account the y position of each portion inside each solid particle, we calculate the ensemble average $\langle\phi(y)\rangle$ of solid concentration along y during the steady state of each simulation. In qualitative agreement with Refs. [51,52], we observe solid particle layering near the wall region, due to strong hydrodynamic interactions between solid particles and wall, as shown in Fig. 8. The layering phenomenon becomes relaxed and relatively flat compared to the averaged concentration when moving away from the wall, except in the case of $\phi = 68.7\%$, where wall effects persist to long distance [51].

Moreover, we investigate qualitatively the microstructure of the suspension and discuss it in relation to results from the literature. For each pair of solid particles located one diameter away from walls (to avoid the first peak of layering in Fig. 8), we

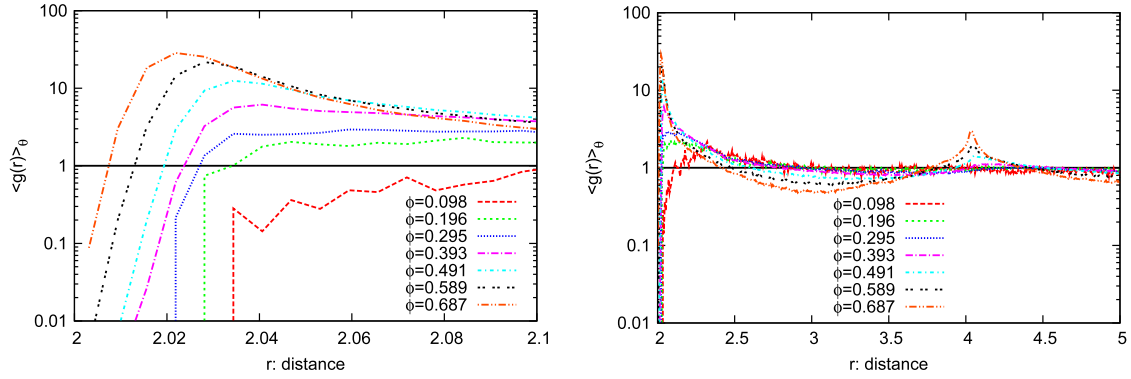

(a) RDF vs. short distance.

(b) RDF vs. long distance.

Fig. 9. Pairwise radial distribution function (RDF) $g(r)$ in box $[16, 16]$ provides information about the suspension microstructure.

calculate the radial distribution function (RDF) averaged over all orientations $\langle g(r)\rangle_\theta$, which represents the time-averaged probability of finding a neighboring solid particle normalized by the number density of the solid particles [42]. Due to short-ranged repulsive force no particles overlap or contact occurs, which is indicated by the decay of the RDF to zero at $r = 2$ as shown in Fig. 9(a). Higher concentrations lead to a shift in the RDF with the first peak occurring at closer distances. Moving away from the first peak distance, the RDF drops significantly for concentrated suspension of $\phi = 49.1\%, 58.9\%$, and 68.7%, before increasing again towards a second maximum at two-diameters distance, as shown in Fig. 9(b). The second peak is an increasing function of concentration [41] and its presence indicates positions of solid particles are still correlated around a distance of two diameters. Nevertheless, $\langle g(r)\rangle_\theta$ goes to unity for all concentrations in sufficiently long distance, indicating uncorrelated solid particles.

Although it is difficult to compare microstructure in details, the SPH results presented here reproduce qualitatively those obtained from simulations of SD [42,41] and FCM [51], proving the validity of the present approach. A detailed analysis on the rheological and microstructural behavior of a concentrated suspension is beyond the scope of this work and will be presented in the future.

5. Conclusion

Within the modeling framework for a confined particulate suspension using smoothed particle hydrodynamics (SPH) [14], we have proposed a splitting integration scheme for describing the interactions between non-Brownian solid particles. In particular, the lubrication force between each pair of solid particles is taken into account implicitly and velocities of solid particles are updated by using a pairwise iterative sweeping. The remaining forces acting on the solid particles are integrated explicitly with a time step Δt given by the common stability criteria in SPH. The splitting scheme is computationally superior to purely explicit schemes, especially in the concentrated regime, where it allows us to run stable simulations with much larger sub-time-steps on a reasonable computing time up to $\phi = 68.7\%$ in two dimensions.

The concept and operations of the splitting scheme offer some advantages over standard approaches. On the one hand, it avoids the performance of a full matrix inversion over all the solid particles as used in "conventional" implicit schemes [4] and, on the other hand it bypasses the definition of solid-particles-clusters adopted in "local" implicit schemes [15]. In contrast to the previous approaches, the novel scheme generates a series of small systems of equations, which are solved analytically rather than numerically. Given a pre-defined solid particle concentration, a suitable tolerance can be adopted leading to convergence in the rheological results. Its specific choice represents a trade-off between desired accuracy and computational costs. Moreover, the fact that the average number of neighboring solid particles and number of sweeps on pairs for a fixed tolerance do not increase with the system size indicates preserved linear scaling of the algorithm with the number of simulated solid particles N.

Accuracy and consistency of the proposed splitting method have been validated against standard SPH results based on explicit integrators and theoretical results. As a final remark we should note that, although the simulations performed here were based on the deterministic SPH method, the proposed splitting integration scheme can be easily generalized to mesoscopic methods, such as dissipative particle dynamics [28] and smoothed dissipative particle dynamics [19,53,54]. The modeling of highly concentrated *Brownian* colloidal suspensions based on the sweeping ideas can be simply generalized by incorporating an extra stochastic force in the lubrication model which is connected to the force (Eq. (7)) via a fluctuation–dissipation theorem. Moreover, the proposed scheme is not limited to particle-based methods describing the fluid, but can be easily applied to other simulation techniques employed for suspensions using short-ranged lubrication forces between pairwise solid particles.

Acknowledgments

The authors appreciate the financial support provided by the DFG (German Research Foundation) via grant EL503/1-2. XB thanks Mr. Sergey Litvinov for useful discussions and acknowledges the support of the TUM-Graduate School's Faculty Graduate Center Mechanical Engineering at the Technische Universität München. Computer resources for this project have been provided by the Leibniz Supercomputing Center under grant pr58ye.

Appendix. Solution to Eq. (12)

With the definition of $A_{\alpha\beta}$ as

$$A_{\alpha\beta} = -\frac{\eta \Delta t_{sweep}}{2m_\alpha}\left\{A_1\left[\left(\frac{2a}{s}\right)^{3/2} - \left(\frac{2a}{s_c}\right)^{3/2}\right] + A_2\left[\left(\frac{2a}{s}\right)^{1/2} - \left(\frac{2a}{s_c}\right)^{1/2}\right]\right\}, \tag{A.1}$$

and using the free algebra software *Maxima* (http://maxima.sourceforge.net), we get

$$\tilde{V}_\alpha(1) = \left\{\left[\underline{e_{\alpha\beta}(1)e_{\alpha\beta}(2)}\left(V'_\beta(2) - V'_\alpha(2)\right) + 2\underline{e_{\alpha\beta}(2)e_{\alpha\beta}(2)} \times V'_\alpha(1) + \underline{e_{\alpha\beta}(1)e_{\alpha\beta}(1)}\left(V'_\beta(1) + V'_\alpha(1)\right)\right]A_{\alpha\beta} - V'_\alpha(1)\right\} \Big/ \left\{\underline{\left[2e_{\alpha\beta}(1)e_{\alpha\beta}(1) + 2e_{\alpha\beta}(2)e_{\alpha\beta}(2)\right]A_{\alpha\beta} - 1}\right\}. \tag{A.2}$$

Table A.4
The summary of operations count.

Equation	Count
(A.1)	27
(A.2)	22
(A.3)	11
(A.4)	11
(A.5)	11
Total	82

Due to symmetry of the two dimensions, by interchanging index (1) with (2) in Eq. (A.2), $\tilde{V}_\alpha(2)$ is obtained as

$$\begin{aligned}\tilde{V}_\alpha(2) = &\left\{\left[e_{\alpha\beta}(1)e_{\alpha\beta}(2)\left(V'_\beta(1)-V'_\alpha(1)\right)+2e_{\alpha\beta}(1)e_{\alpha\beta}(1)V'_\alpha(2)\right.\right.\\&\left.+e_{\alpha\beta}(2)e_{\alpha\beta}(2)\left(V'_\beta(2)+V'_\alpha(2)\right)\right]\\&\times A_{\alpha\beta}-V'_\alpha(2)\Big\}/\Big\{\left[2e_{\alpha\beta}(1)e_{\alpha\beta}(1)\right.\\&\left.+2e_{\alpha\beta}(2)e_{\alpha\beta}(2)\right]A_{\alpha\beta}-1\Big\}. \qquad (A.3)\end{aligned}$$

Due to symmetry of the two particles, by interchanging subscript α with β in Eqs. (A.2) and (A.3), $\tilde{V}_\beta(1)$ and $\tilde{V}_\beta(2)$ are obtained as

$$\begin{aligned}\tilde{V}_\beta(1) = &\left\{\left[e_{\alpha\beta}(1)e_{\alpha\beta}(2)\left(V'_\alpha(2)-V'_\beta(2)\right)+2e_{\alpha\beta}(2)e_{\alpha\beta}(2)\right.\right.\\&\times V'_\beta(1)+e_{\alpha\beta}(1)e_{\alpha\beta}(1)\left(V'_\alpha(1)+V'_\beta(1)\right)\Big]\\&\times A_{\alpha\beta}-V'_\beta(1)\Big\}/\Big\{\left[2e_{\alpha\beta}(1)e_{\alpha\beta}(1)+2e_{\alpha\beta}(2)\right.\\&\left.\times e_{\alpha\beta}(2)\right]A_{\alpha\beta}-1\Big\}. \qquad (A.4)\end{aligned}$$

$$\begin{aligned}\tilde{V}_\beta(2) = &\left\{\left[e_{\alpha\beta}(1)e_{\alpha\beta}(2)\left(V'_\alpha(1)-V'_\beta(1)\right)+2e_{\alpha\beta}(1)e_{\alpha\beta}(1)\right.\right.\\&\times V'_\beta(2)+e_{\alpha\beta}(2)e_{\alpha\beta}(2)\left(V'_\alpha(2)+V'_\beta(2)\right)\Big]\\&\times\ A_{\alpha\beta}-V'_\beta(2)\Big\}/\Big\{\left[2e_{\alpha\beta}(1)e_{\alpha\beta}(1)\right.\\&\left.+2e_{\alpha\beta}(2)e_{\alpha\beta}(2)\right]A_{\alpha\beta}-1\Big\}. \qquad (A.5)\end{aligned}$$

When the number of numerical operations is counted, duplicate expressions are stored and calculated only once, such as the ones underlined in Eq. (A.2). Therefore, the count of actual operations for each equation is listed in Table A.4.

References

[1] R.G. Larson, The Structure and Rheology of Complex Fluids, Oxford University Press, New York, 1999.
[2] J. Mewis, N.J. Wagner, J. Non-Newton. Fluid 157 (2009) 147–150.
[3] N.J. Wagner, J.F. Brady, Phys. Today 62 (2009) 27–32.
[4] G. Bossis, J.F. Brady, J. Chem. Phys. 80 (1984) 5141–5154.
[5] J.F. Brady, G. Bossis, Annu. Rev. Fluid Mech. 20 (1988) 111–157.
[6] A. Sierou, J.F. Brady, J. Fluid Mech. 448 (2001) 115–146.
[7] J.W. Swan, J.F. Brady, Phys. Fluids 19 (2007) 113306.
[8] J.W. Swan, J.F. Brady, Phys. Fluids 22 (2010) 103301.
[9] W.R. Hwang, M.A. Hulsen, H.E.H. Meijer, J. Comput. Phys. 194 (2004) 742–772.
[10] W.R. Hwang, M.A. Hulsen, H.E.H. Meijer, J. Non-Newton. Fluid 121 (2004) 15–33.
[11] A.J.C. Ladd, J. Fluid Mech. 271 (1994) 285–309.
[12] A.J.C. Ladd, J. Fluid Mech. 271 (1994) 311–339.
[13] J.M.V.A. Koelman, P.J. Hoogerbrugge, Europhys. Lett. 21 (1993) 363–368.
[14] X. Bian, S. Litvinov, R. Qian, M. Ellero, N.A. Adams, Phys. Fluids 24 (2012) 012002.
[15] N.Q. Nguyen, A.J.C. Ladd, Phys. Rev. E 66 (2002).
[16] S. Litvinov, M. Ellero, X.Y. Hu, N.A. Adams, J. Comput. Phys. 229 (2010) 5457–5464.
[17] T. Shardlow, SIAM J. Sci. Comput. 24 (2003) 1267–1282.
[18] J.J. Monaghan, Annu. Rev. Astron. Astr. 30 (1992) 543–574.
[19] P. Español, M. Revenga, Phys. Rev. E 67 (2003) 026705.
[20] J.P. Morris, P.J. Fox, Y. Zhu, J. Comput. Phys. 136 (1997) 214–226.
[21] G.R. Liu, M.B. Liu, Smoothed Particle Hydrodynamics a Meshfree Particle Method, World Scientific Publishing Co. Pte. Ltd., Singapore, 2003.
[22] J.J. Monaghan, J. Comput. Phys. 110 (1994) 399–406.
[23] M. Ellero, N.A. Adams, Int. J. Numer. Methods Eng. 86 (2011) 1027–1040.
[24] S. Chen, N. Phan-Thien, B.C. Khoo, X.J. Fan, Phys. Fluids 18 (2006) 103605.
[25] Z. Li, G. Drazer, Phys. Fluids 20 (2008) 103601.
[26] A.J.C. Ladd, R. Verberg, J. Stat. Phys. 104 (2001) 1191–1251.
[27] I.O. Götze, H. Noguchi, G. Gompper, Phys. Rev. E 76 (2007) 046705.
[28] P.J. Hoogerbrugge, J.M.V.A. Koelman, Europhys. Lett. 19 (1992) 155–160.
[29] N.S. Martys, J. Rheol. 49 (2005) 401–424.
[30] S. Jamali, M. Yamanoi, J. Maia, Soft Matter 9 (2013) 1506–1515.
[31] S. Kim, S.J. Karrila, Microhydrodynamics: Principles and Selected Applications, Dover Publications, Incorporated, 1991.
[32] X.F. Yuan, R.C. Ball, J. Chem. Phys. 101 (1994) 9016–9021.
[33] J. Kromkamp, D. van den Ende, D. Kandhai, R. van der Sman, R. Boom, Chem. Eng. Sci. 61 (2006) 858–873.
[34] A.J.C. Ladd, Phys. Fluids 9 (1997) 491–499.
[35] R.C. Ball, J.R. Melrose, Adv. Colloid Interface 59 (1995) 19–30.
[36] J.R. Melrose, R.C. Ball, Europhys. Lett. 32 (1995) 535–540.
[37] A.A. Catherall, J.R. Melrose, R.C. Ball, J. Rheol. 44 (2000) 1–25.
[38] J.R. Melrose, R.C. Ball, J. Rheol. 48 (2004) 937–960.
[39] J.R. Melrose, R.C. Ball, J. Rheol. 48 (2004) 961–978.
[40] D.I. Dratler, W.R. Schowalter, J. Fluid Mech. 325 (1996) 53–77.
[41] A. Sierou, J.F. Brady, J. Rheol. 46 (2002) 1031–1056.
[42] J.F. Brady, G. Bossis, J. Fluid Mech. 155 (1985) 105–129.
[43] R.D. Groot, P.B. Warren, J. Chem. Phys. 107 (1997) 4423–4435.
[44] R. Courant, K. Friedrichs, H. Lewy, Math. Ann. 100 (1928) 32–74.
[45] S. Whitehouse, M. Bate, Mon. Not. R. Astron. Soc. 353 (2004) 1078–1094.
[46] C.L. Darabaner, J.K. Raasch, S.G. Mason, Can. J. Chem. Eng. 45 (1967) 3–12.
[47] G.I. Batchelor, J.T. Green, J. Fluid Mech. 56 (1972) 375–400.
[48] I.M. Krieger, T.J. Dougherty, Trans. Soc. Rheol. 3 (1959) 137–152.
[49] J.C. Van Der Werff, C.G. De Kruif, J. Rheol. 33 (1989) 421–454.
[50] I. Zarraga, D. Hill, D. Leighton, J. Rheol. 44 (2000) 185–220.
[51] K. Yeo, M.R. Maxey, J. Fluid Mech. 649 (2010) 205–231.
[52] C.R. Nugent, K.V. Edmond, H.N. Patel, E.R. Weeks, Phys. Rev. Lett. 99 (2007) 025702.
[53] A. Vázquez-Quesada, M. Ellero, P. Español, J. Chem. Phys. 130 (2009) 034901.
[54] A. Vázquez-Quesada, M. Ellero, P. Español, Microfluid. Nanofluidics 13 (2012) 249–260.

Journal of Non-Newtonian Fluid Mechanics 213 (2014) 39–49

Contents lists available at ScienceDirect

Journal of Non-Newtonian Fluid Mechanics

journal homepage: http://www.elsevier.com/locate/jnnfm

Hydrodynamic shear thickening of particulate suspension under confinement

Xin Bian [a,*], Sergey Litvinov [a], Marco Ellero [a,b], Norman J. Wagner [c]

[a] Lehrstuhl für Aerodynamik und Strömungsmechanik, Technische Universität Müenchen, Boltzmannstraße 15, D-85748 Garching bei München, Germany
[b] Zienkiewicz Centre for Computational Engineering, University of Wales Swansea, Singleton Park SA2 8PP, UK
[c] Department of Chemical and Biomolecular Engineering, University of Delaware, 150 Academy Street, Colburn Laboratory, Newark, DE 19716, USA

ARTICLE INFO

Article history:
Received 6 March 2014
Received in revised form 2 September 2014
Accepted 9 September 2014
Available online 18 September 2014

Keywords:
Continuous/hydrodynamic shear thickening
Wall confinement
Hydrodynamic clusters
SPH simulation

ABSTRACT

We study the rheology of dense suspensions of non-Brownian repulsive particles. The suspensions consist of two-dimensional discoidal particles confined by walls orthogonal to the shear gradient direction and are simulated by the method of smoothed particle hydrodynamics. The strength of hydrodynamic shear thickening is primarily determined by the distribution of hydrodynamic clusters formed during shear flow while confinement plays a geometrical role and indirectly affects viscosity. Under strong confinement a percolating network of clusters develops into a jamming structure at high shear rate and as a result, the viscosity increases substantially. Extrapolating the viscosity to the limit of very weak confinement shows that confinement is essential to observe hydrodynamic shear thickening in these non-Brownian suspensions.

1. Introduction

Suspensions of particles are ubiquitous, with blood, pharmaceuticals, and slurry as some common examples [1,2]. Understanding their transport phenomena and rheology is of industrial interest, medical relevance and scientific importance [3,4]. In particular, the property of shear thickening, where viscosity increases with elevated shear rate, is on the one hand, a challenge to pumping, coating and spraying operations [5], and on the other hand, an opportunity to develop field responsive materials for a range of applications, such as, energy absorber [6].

Although the particles constituting such suspensions have a wide spectrum of sizes, shear thickening seems to be universal, if measured in the appropriate shear rate range [7]. Brady and coworkers developed the method Stokesian dynamics and predicted that it is the presence of hydrodynamic clusters or *hydroclusters* responsible for shear thickening of Brownian suspensions [8]: upon increasing shear rate, compressive hydrodynamic force dominates Brownian force, particles are forced into close proximity and form transient clusters, termed hydroclusters to distinguish them from aggregates due to conservative forces [1]. Within a cluster the particle density is higher and the fluid is under greater stress due to the diverging short-range lubrication force [9], which leads to a higher viscosity for the suspension [10]. Hydroclusters are fluctuations in particle density that only exist under flow and as such are transient. The existence of hydroclusters is confirmed by flow-small angle neutron scattering [11–13] and optical methods including flow dichroism [14,12] and fast confocal microscopy [15] for colloidal suspensions. Simulations generally show mild continuous shear thickening (CST) under periodic shear flow using Lees–Edwards boundary condition [16–19].

In contrast to colloidal dispersions, *ideal*, non-Brownian hard-sphere suspensions are not expected to exhibit shear thickening and should have a viscosity that is independent of shear rate. However, the presence of surface roughness, friction, and finite particle inertia can all lead to a shear-rate dependent microstructure and rheological properties [20,1,21]. In a recent experiment, a confining geometry is shown to have a strong influence on the discontinuous shear thickening (DST) via increased normal stresses [22,23], where the particles phase attempts to dilate and is confined by the walls of the apparatus and the surface tension of the suspending fluid. The DST is associated with additional surface frictional forces rather than purely hydrodynamic interactions (HIs) acting between particles [23,24,21]. Nevertheless, the strength of HIs also depends on the confinement, which leads to an increase of the suspension viscosity at a fixed shear rate due to additional HIs with the walls and enhancements in the HIs between particles [25].

* Corresponding author at: Division of Applied Mathematics, Brown University, 182 George Street, Providence, RI 02912, USA.
E-mail address: xin_bian@brown.edu (X. Bian).

http://dx.doi.org/10.1016/j.jnnfm.2014.09.003
0377-0257/

Confinement effects on shear thickening have not been studied in depth and the interplay between confinement and hydrocluster formation is still poorly understood. In this work, we study the effects of confinement on continuous shear thickening by simulating a mono-disperse suspension of discoidal particles confined between two walls. To resolve the HIs in a confined suspension, we use a meshfree method called smoothed particle hydrodynamics (SPH) [26], which allows for straightforward modeling of moving boundaries. In addition, model parameters of SPH can be chosen carefully to avoid unnecessary inertial and compressible effects [27,28]. Long- and intermediate-range HIs are computed explicitly by the SPH method and pairwise lubrication forces [29] are introduced between particles to reproduce correctly the short range lubrication interactions, which are below SPH resolution. In this work we consider shear thickening in a non-colloidal suspension where Brownian forces are negligible. To prevent particle overlap a short range repulsive force is added between suspension particles [30,31,18].

This manuscript is organized as follows. In Section 2 the SPH-based model of solid particle suspension is briefly reviewed. Numerical results along with discussions are shown in Section 3. In this work we focus on an area fraction of 0.589, which is well above that reported to be necessary to observe significant hydrocluster formation in 2D suspensions [32]. Characteristic confinement dimensions range from a low of 8 to a maximum of 256 particle radii, which spans the typical box sizes in previous simulations and extends the simulation work to strong confinement as observed in experiments [15]. The flow kinematics, microstructure and rheological response are reported for steady state flow and analyzed as functions of shear rate and confinement with the goal of understanding confinement effects on shear thickening of non-Brownian suspensions. We summarize our results and discussions in Section 4.

2. The SPH-based suspension model

In this section we review a SPH-based suspension model, which is Galilean-invariant and conserves both linear and angular momenta. Both solid walls and solid particles are modeled by SPH boundary particles.

2.1. SPH discretization of Navier–Stokes equations

We employ a SPH formulation to discretize the Navier–Stokes equations on the fluid domain. SPH is a Lagrangian meshless method in which the hydrodynamic equations are solved on a set of numerical particles[1] advected with the local flow velocity [26]. For a comprehensive description of SPH, we refer the reader to some monographs [33–35] and recent review articles [26,36,37].

The continuity equation can be implemented in SPH by a discrete summation form [38]

$$d_i = \frac{1}{\mathcal{V}_i} = \frac{\rho_i}{m_i} = \sum_j W_{ij}, \quad \dot{\mathbf{r}}_i = \mathbf{v}_i, \tag{1}$$

where $d_i, \mathcal{V}_i, m_i, \rho_i, \mathbf{r}_i$ and $\mathbf{v}_i$ are number density, volume, mass, mass density, position, and velocity of SPH particle i, respectively; each SPH particle has a constant mass m_0; $W_{ij} = W(r_{ij})$ is a bell shaped kernel function, which depends on the inter-particle distance r_{ij} and vanishes beyond a cutoff radius r_c, that is, $W_{ij} = 0$ for $r_{ij} \geqslant r_c$.

[1] Note that a numerical particle in SPH should be distinguished from a suspended solid particle: the former simply represents a Lagrangian discretization element; the latter is a physical solid grain whose model is described in Section 2.2. When we say a particle, it always means a solid particle. We always use "SPH particle" to denote the numerical particle.

In this work we use a quintic spline kernel [39,40], which is piecewise and consists of three polynomial functions. This sets the cutoff radius to be $r_c = 3h$, where h is the smoothing length corresponding to the case if a Gaussian kernel were used [37]. Provided that the total number of SPH particles remains constant, total mass is exactly conserved and Eq. (1) provides an operative way to calculate the density.

For the discretization of the momentum equation in the case of viscous incompressible flow, we adopt the following formulation [40]

$$m_i \dot{\mathbf{v}}_i = -\sum_j \left(\frac{p_i}{d_i^2} + \frac{p_j}{d_j^2}\right) \frac{\partial W}{\partial r_{ij}} \mathbf{e}_{ij} + \sum_j 4\eta \left(\frac{1}{d_i^2} + \frac{1}{d_j^2}\right) \frac{\partial W}{\partial r_{ij}} \times \frac{\mathbf{e}_{ij} \cdot \mathbf{v}_{ij}}{r_{ij}} \mathbf{e}_{ij}. \tag{2}$$

The first part on the rhs is the sum of pairwise conservative pressure force $\mathbf{F}_{ij}^C$. An equation of state relating density ρ to pressure p may be written as

$$p = p_0 \left[\left(\frac{\rho}{\rho_r}\right)^7 - 1 \right], \tag{3}$$

where p_0 (related to sound speed c_s) and ρ_r are parameters chosen based on a scale analysis [41,39], to have sufficiently small density variations. The second part on the rhs of Eq. (2) is the sum of pairwise dissipative viscous force $\mathbf{F}_{ij}^D$, which resists the relative velocity $\mathbf{v}_{ij} = \mathbf{v}_i - \mathbf{v}_j$. Dynamic viscosity η is taken to be constant for each SPH particle. We set $h = 1.5dx$, where dx is the initial distance between neighboring SPH particles, as this choice allows for obtaining the Stokes drag acting on a solid particle within 1% accuracy according to its geometrical radius [42].

By interchanging particle indices, $\mathbf{F}_{ij}^C = -\mathbf{F}_{ji}^C$ and $\mathbf{F}_{ij}^D = -\mathbf{F}_{ji}^D$, Newton's third law is satisfied and linear momentum is conserved exactly. Furthermore, both $\mathbf{F}_{ij}^C$ and $\mathbf{F}_{ij}^D$ act along the unit vector $\mathbf{e}_{ij} = \mathbf{r}_{ij}/r_{ij} = (\mathbf{r}_i - \mathbf{r}_j)/|\mathbf{r}_{ij}|$ pointing from particle j to particle i, therefore angular momentum is also conserved strictly, which is crucial for recovering the correct rotation of a solid particle under shear flow [40].

The density and force calculations are based on pairwise interactions between neighboring SPH particles, therefore the algorithm can be readily implemented by a slight modification on any existing software of particle methods (e.g., [43,44]).

2.2. Suspended solid particle and bounding wall

Any solid particle suspended in a fluid or any solid wall can be modeled by collecting a group of SPH particles as boundary particles within the solid domain. The SPH particles at boundary interact with SPH fluid particles by means of suitable forces which enforce no-slip boundary condition at the fluid–solid interface [40]. Initially, all SPH fluid particles are placed on a square grid inside the fluid domain and a new set of SPH boundary particles is created parallel to the surface inside each solid object, as shown in Fig. 1. The distance between neighboring layers is dx as well as the distance between two neighboring SPH particles in the same layer. This choice ensures to have an approximately constant number of interpolating points near the fluid–solid interface.

During the pairwise viscous force calculation $\mathbf{F}_{bf}^D$, velocity $\mathbf{v}_b$ of any SPH boundary particle b inside a solid object α is extrapolated from its interacting SPH fluid particle f by requiring no-slip condition on the solid geometrical surface. Afterward, the total force and torque exerted by the surrounding fluid on α are computed by collecting forces and torques on each b as follows,

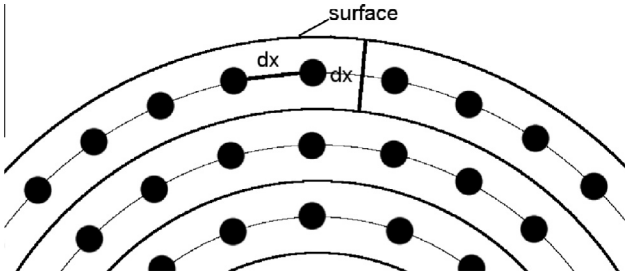

Fig. 1. Representation of a spherical solid particle (similar for a plane wall): SPH boundary particles are placed parallel to the surface with the same neighboring distance *dx*. During the motion of the solid object, SPH boundary particles do not have relative movement to each other and the rigid motion of the solid object is guaranteed.

$$\mathbf{F}_{\alpha}^{SPH} = \sum_{b}\sum_{f}(\mathbf{F}_{bf}^{C} + \mathbf{F}_{bf}^{D}), \tag{4}$$

$$\mathbf{T}_{\alpha}^{SPH} = \sum_{b}\sum_{f}(\mathbf{r}_{b} - \mathbf{R}_{\alpha}) \times (\mathbf{F}_{bf}^{C} + \mathbf{F}_{bf}^{D}), \tag{5}$$

where $\mathbf{r}_b$ is position of b and $\mathbf{R}_\alpha$ is center position of α. In this way, the long- and intermediate-range hydrodynamics are captured correctly. Note that $\mathbf{v}_b$ is employed to satisfy the no-slip boundary condition and the actual motion of b is due to the rigid motion of α.

2.3. Lubrication force correction and short-range repulsive force

When two solid particles are in near contact, the flow of the fluid in the gap cannot be captured accurately due to the finite discretization of the fluid, therefore the lubrication forces acting on them are poorly represented. One possible strategy is to increase the resolution locally within the gap until the flow is fully resolved [45]. However, this choice is computationally impractical, especially in the case of a concentrated suspension where many nearly-touching pairs of solid particles can be present at once. To remedy this problem, an analytical form for the pairwise lubrication force at short distance between solid particles was applied [29,46]. A 2*D* squeezing lubrication force for two equal-sized discoidal particles is given as in Ref. [46]

$$\mathbf{F}_{\alpha\beta}^{lub}(s) = -\frac{\eta}{2}\mathbf{V}_{\alpha\beta}\cdot\mathbf{e}_{\alpha\beta}\left[A_1\left(\frac{2a}{s}\right)^{3/2} + A_2\left(\frac{2a}{s}\right)^{1/2}\right]\mathbf{e}_{\alpha\beta}, \tag{6}$$

where $A_1 = \frac{3}{4}\pi\sqrt{2} = 3.3322$, $A_2 = \frac{231}{80}\pi\sqrt{2} = 12.829$; each solid particle has the same radius a and s is the separation distance between the surfaces of solid particle α and β; $\mathbf{V}_{\alpha\beta}\cdot\mathbf{e}_{\alpha\beta}$ is the component of velocity difference along center-to-center line. In the case of SPH, we have introduced a pairwise correction for lubrication force, $\mathbf{F}_{\alpha\beta}^{lub\_cor}(s)$, between solid particles.

$$\mathbf{F}_{\alpha\beta}^{lub\_cor}(s) = \begin{cases} \mathbf{F}_{\alpha\beta}^{lub}(s) - \mathbf{F}_{\alpha\beta}^{lub}(s_c), & s < s_c; \\ 0, & s \geqslant s_c, \end{cases} \tag{7}$$

where $s_c = 1.5h$. Below this resolution length, the lubrication force generated by SPH method is nearly constant such that this value can be subtracted off from that calculated analytically in Eq. (6), to yield an accurate lubrication force between the particles [47]. For the typical SPH resolution $h = 0.3a$ considered in this work, $s_c = 0.45a$. With this correction, the open and close trajectories of two spherical particles under shear flow are reproduced accurately by comparing with analytical results [47].

It has been pointed out that an ideal non-Brownian concentrated particulate suspension under shear flow is a singular problem [30,48,31,49]: that is, the distance between neighboring solid particles becomes indefinitely smaller along the compression axis for some instantaneous configurations and there is no steady state under shear flow. Therefore, in numerical simulations a very short-range repulsive force is usually introduced to stabilize an ideal non-Brownian suspension and prevent particle overlap for a finite time step. The specific form of the repulsive force is not crucial as long as it is stiff [31]. In this work we adopt a commonly used repulsive force law which reads [16,31,18],

$$\mathbf{F}_{\alpha\beta}^{rep}(s) = F_0\frac{\tau e^{-\tau s}}{1 - e^{-\tau s}}\mathbf{e}_{\alpha\beta}, \tag{8}$$

where $\tau^{-1} = 0.01a$ sets the active range and $|F_0|$ sets the magnitude. The repulsive force decays below $1\%|F_0|$ beyond $0.05a$.

We note that $\mathbf{F}_{\alpha\beta}^{lub\_cor} = -\mathbf{F}_{\beta\alpha}^{lub\_cor}$ and $\mathbf{F}_{\alpha\beta}^{rep} = -\mathbf{F}_{\beta\alpha}^{rep}$, and they both act along $\mathbf{e}_{\alpha\beta}$, therefore both linear and angular momenta are always conserved. The same repulsion is also applied between the solid particles and the upper and lower bounding walls.

2.4. Time integration

To update positions and velocities of SPH fluid particles, a modified explicit velocity Verlet algorithm is utilized [50]. To maintain the numerical stability of the explicit time-integrator, the time-step size Δt must be restricted by three conditions [39]:

1. $\Delta t \leqslant 0.125h^2/\nu$: viscous constraint;
2. $\Delta t \leqslant 0.25h/c_s$: Courant–Friedrichs–Lewy condition;
3. $\Delta t \leqslant 0.25\min\sqrt{(h/f_s)}$: maximum SPH particle acceleration,

where the kinematic viscosity $\nu = \eta/\rho$; c_s is the speed of sound in fluid; f_s is acceleration acting on any SPH particle.

For each solid particle α, the total force and torque acting on it are summarized as follows

$$\mathbf{F}_{\alpha} = \mathbf{F}_{\alpha}^{SPH} + \sum_{\beta\neq\alpha}\mathbf{F}_{\alpha\beta}^{lub\_cor} + \sum_{\beta\neq\alpha}\mathbf{F}_{\alpha\beta}^{rep},$$
$$\mathbf{T}_{\alpha} = \mathbf{T}_{\alpha}^{SPH}. \tag{9}$$

To integrate the previous set of ordinary differential equations explicit schemes (e.g., Euler or velocity Verlet) are limited by extremely small time steps, especially in the case of dense suspension at high shear stress, where particles form clusters and move collectively (see Section 3.2). We have recently proposed a *splitting* integration scheme to stabilize and accelerate simulations in such scenarios [47]. The key idea is summarized as follows. The intermediate- and long-range multi-body hydrodynamic forces on particles, which are computed by the SPH method, are taken into account using the *explicit* velocity Verlet integration; the short-range lubrication correction force in Eq. (7), which is introduced to resolve the flow of very thin film between nearby particles, is active in parallel to the SPH forces. These lubrication forces depend on both relative position and velocity of two particles, and are generally very stiff. Furthermore, relative motion of one pair causes relative motions of all nearby pairs and the overall particles' behavior is rather collective than purely pairwise (see definition of hydrocluster in Section 3.2). Both the stiffness of lubrication force and the collective behavior of particles lead any explicit integration to be extremely unstable. The particular behavior of concentrated suspension motivates us to integrate the lubrication forces *implicitly* by sweeping over all the neighboring pairs iteratively, until convergence in the solution of velocities is obtained; the repulsive force between solid particles is also integrated using the *explicit* velocity Verlet scheme.

The concept and operations of the splitting scheme offer some advantages over standard approaches. On the one hand, it avoids the performance of a full matrix inversion over all the solid particles as used in "conventional" implicit schemes [51]; on the other

hand it bypasses the "local" implicit schemes performed on clusters [52], which depends on the dynamics. In contrast to the previous approaches, the novel scheme generates a series of small systems of equations for the lubrication contribution, which are solved analytically rather than numerically. For further details on accuracy and efficiency, we refer to Ref. [47].

3. Results and discussions

A randomly dispersed suspension is created within a simulation box, as depicted in Fig. 2. All simulation parameters are non-dimensional and the relevant physics are determined by the Reynolds number, non-dimensional shear rate and non-dimensional shear stress, which will be defined later. Solvent dynamic viscosity $\eta = 8.46$ and density $\rho = 1.0$ are input parameters of SPH method. Particles are neutrally buoyant with radius $a = 1$. Channel gap L_y is varied within 8, 16, 32, 64, 128, and 256. Particle Reynolds number is defined as $Re = \rho a^2 \dot{\gamma}^{in}/\eta$, where input shear rate $\dot{\gamma}^{in} = 2|v_w|/L_y = 0.10575$ with v_w being the wall velocity. To rule out effects of finite particle inertia [53], $Re = 0.0125$ is kept constant in all simulations and $|v_w|$ has a value within 0.423, 0.846, 1.692, 3.384, 6.768, and 13.536 for each L_y respectively. L_x is always selected sufficiently large to minimize effects of periodic images. Artificial sound speed $c_s = 30$ is universally adopted to have a weakly compressible fluid. The ratio between the areas of particles and the simulation box defines a 2*D* solid concentration ϕ. Previous literature relates this areal fraction of the 2*D* suspension to be equivalent to 2/3 of the volume fraction of a 3*D* suspension [54]. To study the effects of confinement L_y, different total numbers of particles N_p are used in different domain sizes, e.g., $N_p = 48 - 1536$ for $\phi = 0.589$.

3.1. Viscosity

3.1.1. Newtonian regime

As layers of particles [55,46,47] form in the near wall regions, suspensions show wall slip under shear flow, as shown in Fig. 3. We note that velocity slip is present between suspension and wall while a no slip interface is always preserved between fluid and solid [40]. We further note that increasing L_y, decreasing ϕ, or reducing $\dot{\gamma}^{in}$ alleviates suspension slip near the wall. An effective shear rate $\dot{\gamma}$ is obtained by linearly fitting the time averaged velocity profile excluding the regions near the two walls. Note that

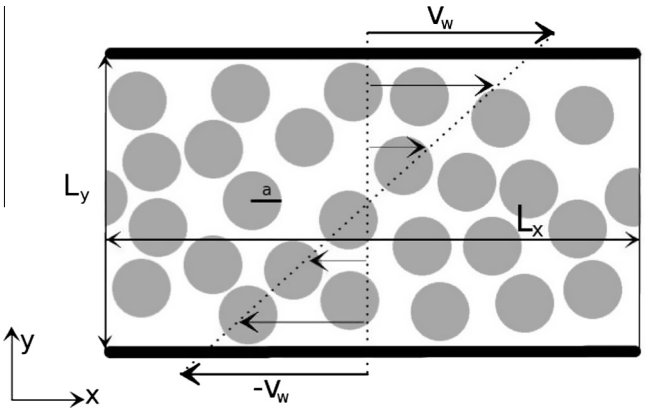

Fig. 2. Schematic of a 2*D* suspension under Couette flow: multiple solid particles with radius a are suspended in a Newtonian solvent; periodic boundaries are applied in x direction; two parallel walls modeled by SPH boundary particles are placed in y direction and move with velocity $|v_w|$ in opposite directions, creating a clockwise shear flow with shear rate $\dot{\gamma}^{in}$.

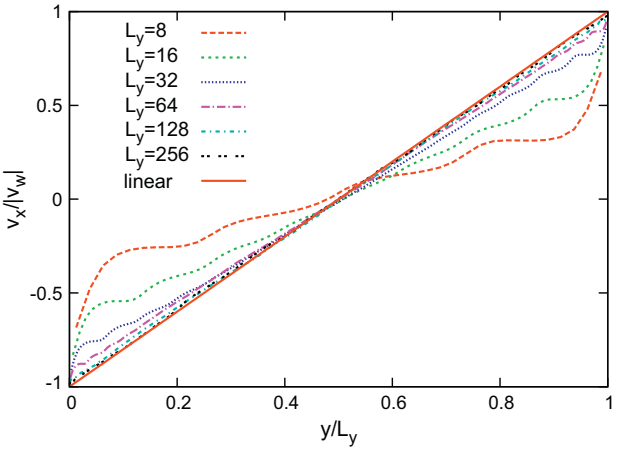

Fig. 3. Time averaged velocity profiles for $\phi = 0.589$, $\dot{\gamma}^{in} = 0.10575$, and $F_0^{rep} = 89.4645$ at Newtonian regime: the linear profile is generated by SPH simulation of pure fluid, which agrees well with input shear rate $\dot{\gamma}^{in}$. Beyond the slip regions near walls, the profiles are always linear in the middle. Increasing the height of the channel L_y reduces slip significantly.

particle Reynolds number would be even smaller if it is based on $\dot{\gamma}$ instead of $\dot{\gamma}^{in}$, assuring an inertia-less regime.

Shear stress σ_{xy} of a suspension is directly obtained from the shear force F_x acting on SPH walls as F_x/L_x. Thus, this stress includes the hydrodynamic stress as well as any stress arising due to the short-range repulsion acting between particles. With the effective shear rate $\dot{\gamma}$, viscosity of the suspension is calculated as

$$\eta^{sus} = \frac{\sigma_{xy}}{\dot{\gamma}} = \frac{F_x}{L_x \dot{\gamma}}. \tag{10}$$

For dilute particle suspensions, the relative viscosity has been shown analytically as

$$\eta^{sus}/\eta = 1 + [\eta]\phi, \tag{11}$$

where $[\eta]$ is the intrinsic viscosity. $[\eta] = 2.5$ for three dimensional spheres recovering the Einstein's result and $[\eta] = 2$ for two dimensional discs [56]. For dense suspensions, various phenomenological models have been proposed [57]. In particular, the Krieger & Dougherty model based on semi-analytical solution reads as

$$\eta^{sus}/\eta = (1 - \phi/\phi_{max})^{-[\eta]\phi_{max}}, \tag{12}$$

where ϕ_{max} is the maximum possible concentration and $[\eta] = 2$ [58]. Furthermore, the Quemada model based on optimized dissipation energy reads as

$$\eta^{sus}/\eta = (1 - \phi/\phi_{max})^{-2}, \tag{13}$$

which is a particular case of Eq. (12) with exponent $[\eta]\phi_{max} = 2$ [59] previously used for both two and three dimensions. For an infinite box in two dimensional Euclidean space, it was shown by Joseph Louis Lagrange in 1773 that the maximum packing density of discs takes place when discs are placed in a hexagonal lattice and in contact with six neighbors. In such arrangement, $\phi_{max} = \pi/2\sqrt{3} \approx 0.907$. Another useful limit is that of random close packing, which has been determined to be 0.82 in 2*D* by Berryman [60]. We run simulations of ϕ up to 0.589 in the Newtonian regime and compare the viscosities with Eqs. (11)–(13) in Fig. 4. Results of simulations agree well with the analytical solution at dilute concentrations and start to deviate when $\phi > 0.19$. We note that at each ϕ, increasing confinement leads to a larger suspension viscosity and this effect increases with increasing particle concentration. This can be explained in part if one takes a perspective of geometrical

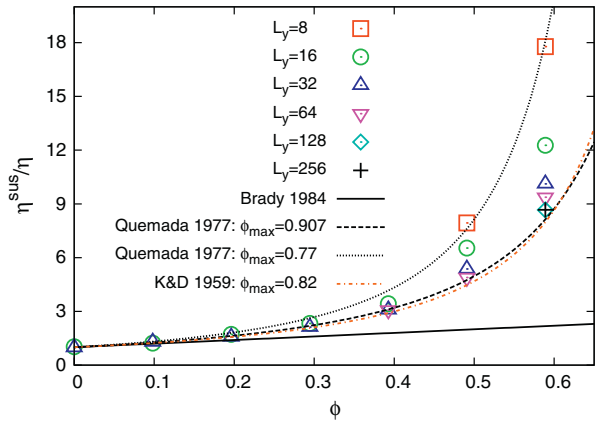

Fig. 4. Relative viscosity versus concentration for $\dot{\gamma}^{in} = 0.10575$, and $F_0^{rep} = 89.4645$ at Newtonian regime: η^{sus} is always calculated based on the effective shear rate $\dot{\gamma}$; should it be based on $\dot{\gamma}^{in}$, η^{sus} would have a smaller value as shown in Ref. [47].

Table 1
Detailed results for two representative confinements $L_y = 16$ and 64: input shear rate $\dot{\gamma}^{in} \equiv 0.10575$ is universally used and repulsive force magnitude $F_0^{rep} = 8.94645 \times f_0^{rep}$; effective shear rate $\dot{\gamma}$ is always measured to obtain suspension viscosity; non-dimensional shear stress σ^* is defined in Eq. (14); case A–I represent individual magnitudes of repulsive force, therefore different σ^*. We note that within each case $\dot{\gamma}$ is generally not the same for each confinement, although $\dot{\gamma}^{in}$ and F_0^{rep} are the same. Statistical error of viscosity: $\leqslant 2\%$ for Newtonian regime; $\leqslant 4\%$ for shear-thickening regime; $\leqslant 7\%$ for jamming regime (G, H, and I at $L_y = 16$.)

Case		$L_y = 16$			$L_y = 64$		
	f_0^{rep}	$100\dot{\gamma}$	σ^*	η^{sus}/η	$100\dot{\gamma}$	σ^*	η^{sus}/η
A	10^3	7.33	8.36E−4	12.07	9.91	8.60E−4	9.17
B	10^2	7.13	8.38E−3	12.26	9.89	8.63E−3	9.24
C	10	7.20	8.35E−2	12.27	9.92	8.68E−2	9.25
D	1	6.83	8.42E−1	13.03	9.93	8.75E−1	9.31
E	10^{-1}	6.53	8.84	14.32	9.89	9.45	10.09
F	10^{-2}	5.64	9.92E	18.60	9.86	1.01E2	10.87
G	10^{-3}	3.95	1.05E3	28.16	9.77	1.06E3	11.48
H	10^{-4}	2.51	1.11E4	46.94	9.67	1.12E4	12.20
I	10^{-5}	1.33	1.25E5	99.57	9.27	1.14E5	13.01

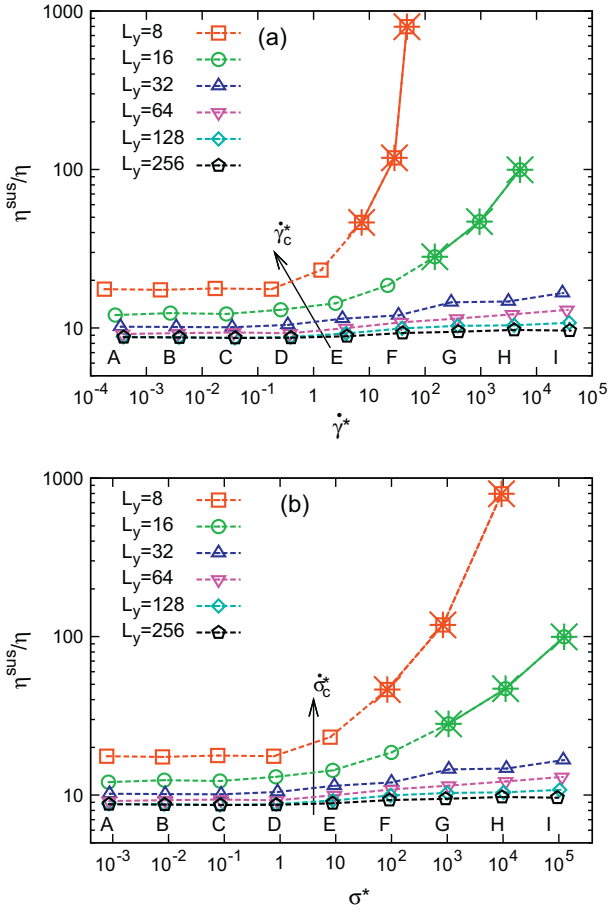

Fig. 5. Shear thickening for $\phi = 0.589$: $A - I$ correspond to $F_0^{rep} = 8.94645 \times 10^3 - 8.94645 \times 10^{-5}$ and are also shown in Table 1. (a) Relative viscosity versus $\dot{\gamma}^*$. (b) Relative viscosity versus σ^*. $\dot{\gamma}_c^*$ and σ_c^* represent critical values at onset of shear thickening. Viscosity is higher under stronger confinement, especially the strongest confinements, where jamming structures are observed (marked by *). Errors are within the symbol size.

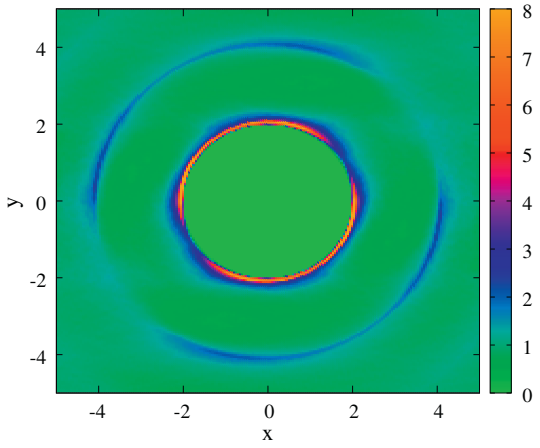

Fig. 6. Radial distribution function (RDF) for $\phi = 0.589$ in system [64, 64] at shear stress C according to Table 1: time-averaged quantity at steady state (shear rate is clockwise). Color indicates the normalized probability. (For interpretation of the references to colour in this figure legend, the reader is referred to the web version of this article.)

packing of particles [61]: for a more confined system the maximum possible concentration ϕ_{max} is smaller and an effective packing ratio, that is, $\phi_{eff} = \phi/\phi_{max}$, is consequently larger, leading to a higher viscosity. With an increasing ϕ, ϕ_{eff} also increases *faster* for the more confined system, so does the suspension viscosity. Moreover, the presence of the confining walls fundamentally changes the HIs between particles, as recently demonstrated by Swan and Brady [25], where more confined system has stronger HIs.

The saturated viscosity at each ϕ, corresponding to the weakest confinement, follows the Quemada model with $\phi_{max} = 0.907$ and Krieger & Dougherty model with $\phi_{max} = 0.82$ (more relevant for this disordered system). The other confined viscosities are bounded from above by the Quemada model with $\phi_{max} = 0.77$, at which viscosity diverges, corresponding to the most confined system with $L_y = 8$.

3.1.2. Non-Newtonian regime

According to previous work on non-Brownian suspensions [16,31,18], a non-dimensional shear rate $\dot{\gamma}^* = 4\eta a\dot{\gamma}/F_0^{rep}$ is defined, which represents the ratio of hydrodynamic and repulsive forces between particles. The value of $\dot{\gamma}^*$ determines the degree to which the shear flow competes with the short-range repulsive forces and therefore is important in determining the suspension microstructure under flow, just as the Péclet number does for a Brownian suspension [8,62]. Dratler and Schowalter [31] studied the consequences and necessity of including this short-range repulsive force

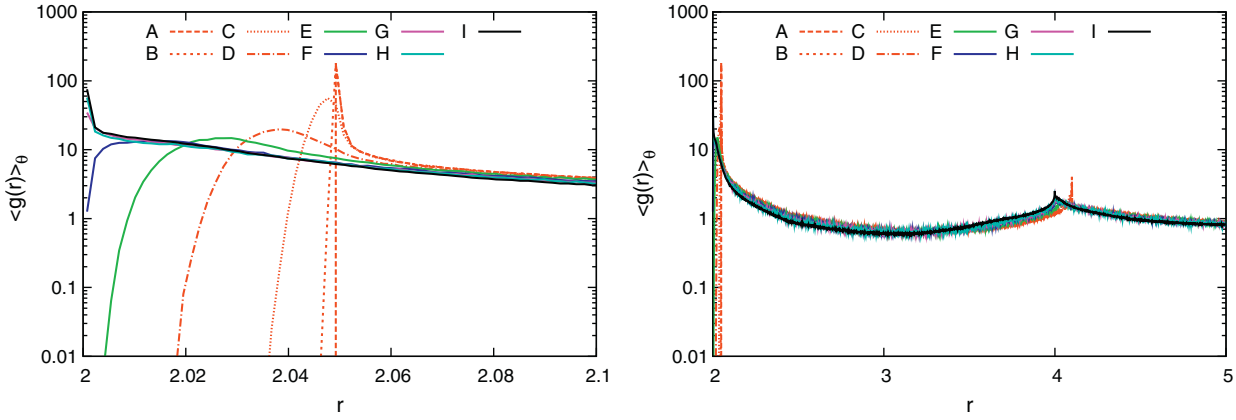

Fig. 7. Radial distribution function (RDF) averaged over all angles for $\phi = 0.589$ in system $[64, 64]$ at different shear stresses: time-averaged quantity at steady state. Left: short distance; right: long distance. *A*–*I* are corresponding to different σ^* in Table 1.

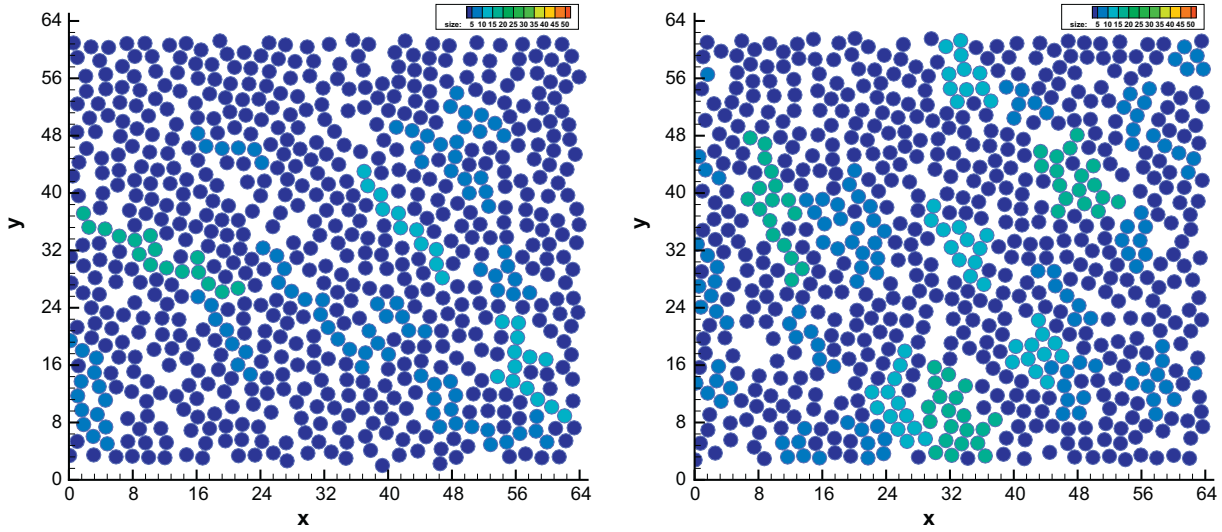

(a) shear stress C (b) shear stress E

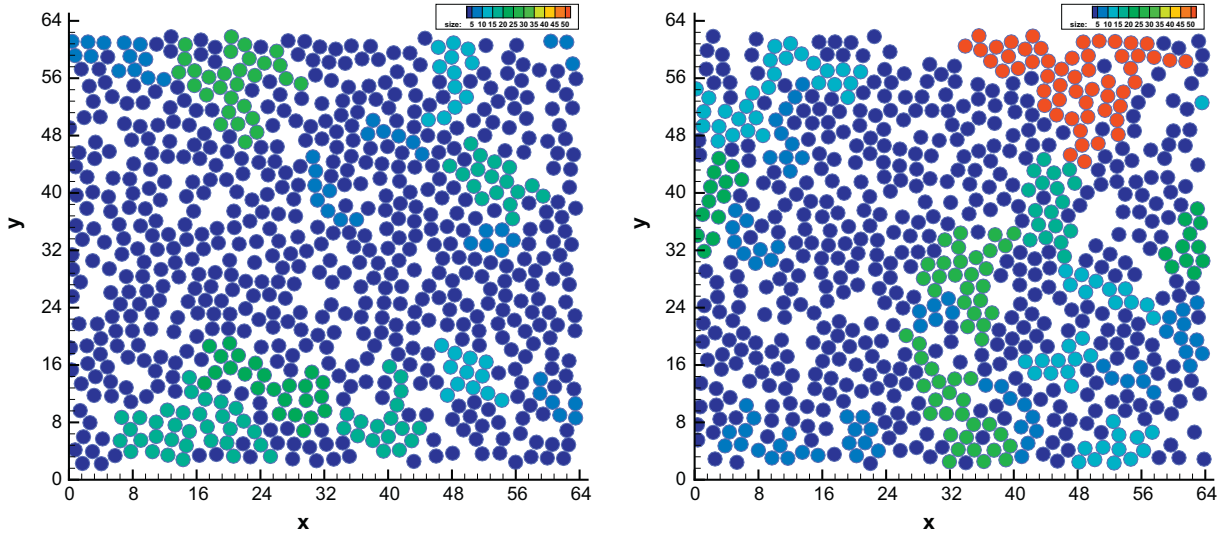

(c) shear stress G (d) shear stress I

Fig. 8. Configurations of hydroclusters for $\phi = 0.589$ in system $[64, 64]$ at shear stress C, E, G, and I according to Table 1: an arbitrary snapshot at strain $\dot{\gamma}t \approx 42$ is selected and color indicates the size of the cluster. Definition of hydrocluster is explained in the text. Note that two layers of particles adjacent to both walls are removed. SPH fluid and boundary particles are removed for clarity. (For interpretation of the references to colour in this figure legend, the reader is referred to the web version of this article.)

on the rheology of 2*D* suspensions using Stokesian dynamics. Inclusion of such a force is necessary to prevent particle overlaps and divergence of the hydrodynamic lubrication forces when particles approach each other. We vary F_0^{rep} to have different $\dot{\gamma}^*$.[2] By examining different concentration $\phi = 0.393, 0.491$, and 0.589, our model of non-aggregating particles always shows reversible shear thickening [12], that is, by slowly ramping up and down shear rate no obvious hysteresis is observed. The following results are shown for $\phi = 0.589$ and other concentrations have qualitatively similar behaviors.

Shear thickening takes place for each confinement L_y studied as shown in Fig. 5(a). At low shear rates, a Newtonian plateau in the effective viscosity is present; upon increasing $\dot{\gamma}^*$, the viscosity becomes non-Newtonian and starts to increase at a critical shear rate $\dot{\gamma}_c^*$, which depends on confinement, namely, a more confined system tends to have a smaller value of $\dot{\gamma}_c^*$ [63,22]. A better estimation of the onset of shear thickening can be obtained by introducing a non-dimensional shear stress σ^* defined as

$$\sigma^* = \frac{\sigma_{xy}}{F_0^{rep}/a} = \eta^{sus} a\dot{\gamma}/F_0^{rep}, \tag{14}$$

where the unit of stress in 2D is force per unit length. If viscosity curves are plotted according to σ^* in Fig. 5(b), shear thickening emerges at the same critical shear stress σ_c^* *for each confinement*, which is reminiscent of the results reported for different concentrations [12]. For future reference, details of two representative confinements ($L_y = 16$ and 64) are presented in Table 1. At each shear stress σ^* (case E–I) in shear thickened regime, stronger confinement also leads to higher viscosity, partially due to similar reasons as in the Newtonian case. Shear thickened regime, however, has its own distinct microstructure from that of Newtonian regime, which has significance on viscosity and will be explained in the next.

3.2. Microstructure

We examine further the microscopic arrangement of the particles and identify microstructure changes corresponding to the viscosity variation for each level of confinement. Similarly to previous works [64,18] we observe an anisotropic particle radial distribution function (RDF), indicating uneven probability for particle arrangements. As an example, for shear stress of $L_y = 64$ at *C* (in Newtonian regime) corresponding to Fig. 5 and Table 1, we present the RDF averaged over steady state in Fig. 6. The high probability of two particles' relative position is along top-left to bottom-right (compression axis) and this preference extends even to the second-neighbor distance. The broken symmetry is a direct consequence of short-range repulsive force, which slows down approaching and accelerates departing of any two nearby particles. This fore-and-aft asymmetry resembles Parsi & Gadala-Maria's experimental measurements on a concentrated suspension of solid spheres [64]. The RDFs for other shear stresses have the same anisotropy, but more compact structure is observed for higher shear stress. This is also indicated by the angle-averaged RDF values at short distance as shown in Fig. 7 (left), where the first peak shifts to closer distance at higher shear stress, indicating a thinner lubrication layer. At low shear stresses A and B, two particles cannot overcome the repulsive barrier at distance $0.05a$. Moving away from the first peak distance, the RDF drops significantly, before increasing again towards a second maximum at two-diameter distance, as shown in Fig. 7 (right). The second peak indicates positions of particles are still correlated around a distance of two diameters. Nevertheless, $\langle g(r)\rangle_\theta$ goes to unity in a sufficiently long distance, indicating uncorrelated particle positions.

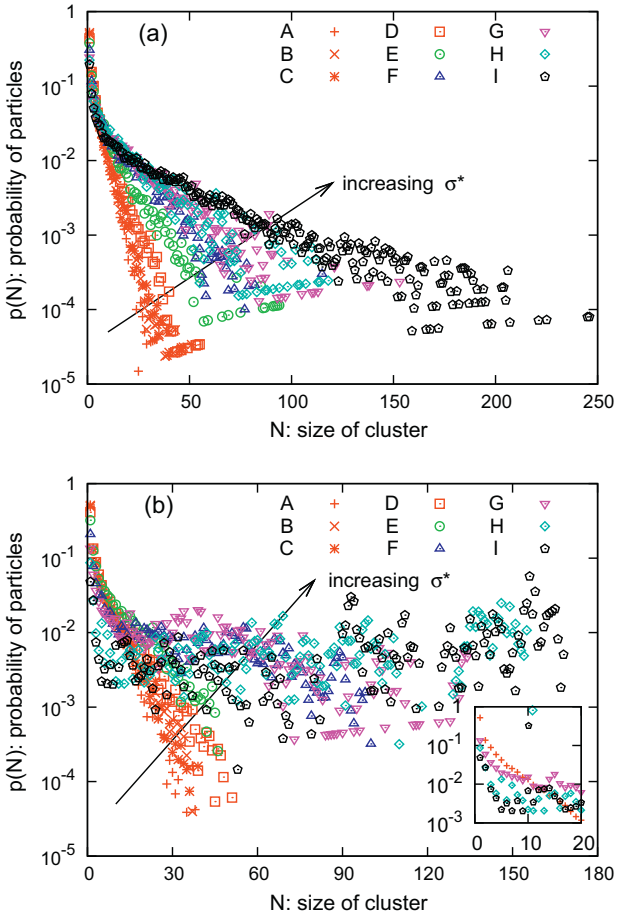

Fig. 9. Probability distribution of particles for $\phi = 0.589$: (a) $[L_x, L_y] = [64, 64]$, $N_p \approx 740$ and (b) $[L_x, L_y] = [64, 16]$, $N_p \approx 160$, inset shows more rapid decay of $p(N)$ for small sized clusters at *G*, *H*, and *I*. *A–I* are corresponding to different σ^* in Fig. 5 and Table 1.

The calculation of RDF is based on a pairwise fashion and its peak location is completely determined by the balance of shearing and repulsive forces. At high shear stress, however, the balance of the two forces does not present in an isolated pairwise fashion but is coupled to many other pairs, that is, besides the pairwise structure mentioned above, we observe also collective behavior of particles in a scale larger than the size of two particles. In particular, we find increasing shear stress changes a well dispersed suspension to one with clustering particles, as directly visualized in Fig. 8.

To further quantify the rheological change, we take distance $0.05a$ as a threshold (repulsive force range), below which two particles are considered within the same cluster. Probability distribution of cluster size $p(N)$ are shown for a typical system of $[L_x, L_y] = [64, 64]$ in Fig. 9(a). At low shear stress (A–D corresponding to Fig. 5 and Table 1), $p(N)$ collapses on a single master curve and accordingly the viscosity is constant. At shear stress $\sigma^* > \sigma_c^*$ (point *E*), the tail of $p(N)$ starts to increase, leading to a significant probability for larger clusters, which corresponds to an increase in viscosity [15]. The same correspondence between $p(N)$ and viscosity is confirmed by points *F–I* in the figure. These clusters are transient and change location and size dynamically.

[2] Varying repulsive force with a fixed shear rate is essentially equivalent to varying shear rate with a fixed repulsive force. It is the ratio of the two (non-dimensional shear rate) that determines the dynamics. We have explicitly checked this equivalence for the non-dimensional shear rates spanning four orders of magnitudes using the two different methodologies. However, the methodology of varying shear rate while keeping low-Reynolds number becomes extremely expensive for the nine orders of magnitudes of non-dimensional shear rates considered in this work. Therefore, varying repulsive force is preferred.

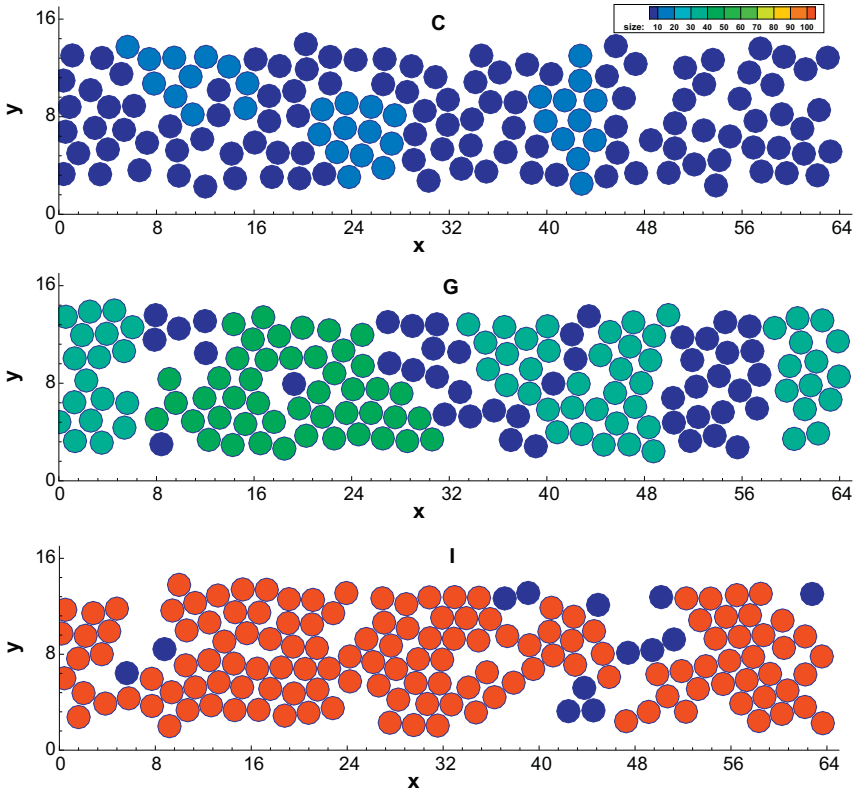

Fig. 10. Configurations of hydroclusters for $\phi = 0.589$ in system $[64, 16]$ at shear stress C, G, and I according to Table 1: an arbitrary snapshot at strain $\dot{\gamma}t \approx 56$ is selected and color indicates the size of the cluster. For shear stress I, there is a clear cut at $x \approx 48$, therefore there is no numerical artifact of clusters spanning across the periodic boundary condition. Note that two layers of particles adjacent to both walls are removed. SPH fluid and boundary particles are removed for clarity. (For interpretation of the references to colour in this figure legend, the reader is referred to the web version of this article.)

In a system with stronger confinement, e.g., $[L_x, L_y] = [64, 16]$, upon increasing σ^* hydroclusters emerge similarly as in system $[64, 64]$, as shown in Fig. 9(b). At larger σ^*, however, a clear distinction is visible at points G, H, and I. Here $p(N)$ shows a more rapid decay at small sized clusters (inset of Fig. 9(b)). Moreover, $p(N)$ does not have a monotonic decrease but saturates with N and appears to flatten out such that sample-spanning clusters exist under flow (see the points H and I). Configurations of hydroclusters at different shear stresses are shown in Fig. 10, where strong clustering of particles takes place at the high shear stresses. Direct visualizations of simulations show that for system in G, H, and I configurations particles do not hop on and off different clusters dynamically but are trapped within the same cluster for more than **10** strain units. In practice only few hydroclusters are observed and particles within each of them move coherently. Under these conditions where the hydroclusters percolate the distance between walls, we consider the suspension in the jamming state and the corresponding value of η^{sus} becomes significantly larger (see Fig. 5).

3.3. Normal stress

Similarly to previous work in three dimension [20,18,65], we observe negative first normal stress difference in our two dimensional system of non-Brownian particles. In particular, in contrast to the DST of frictional particles under confinement [22,23], we do not observe an increase of normal stress or dilatancy accompanying CST. For the nearly incompressible fluid considered here, it is the gradient of the fluid pressure p, but not p itself, that affects fluid motion. Therefore, the normal stress σ_{yy} for the suspension is determined only up to an additive fluid pressure [2]. We show σ_{yy} normalized by the value at shear stress A of Newtonian regime in Fig. 11(a), where normal stress decreases at the onset of CST. The decreasing normal stress on the wall can be explained by the layering effects of particles near the wall: due to the spatial restriction of the wall in the normal direction and strong HIs between particles and wall, particles form layers near the wall [55,66]. With increasing shear stress, the formation of particle clusters reduces the concentration peak at the first layer, as shown in Fig. 11(b). This softens the HIs in the normal direction between the suspension and the wall. As a consequence, the normal stress measured on the wall becomes smaller.

3.4. Strength of shear thickening and its relation with hydrocluster and confinement

To quantify the strength of shear thickening we define a non-dimensional relative excess viscosity as

$$\eta^{sus}_{exc} = (\eta^{sus} - \eta^{sus}_A)/\eta^{sus}_A, \tag{15}$$

where η^{sus}_A is the Newtonian plateau viscosity at shear stress A. Results of η^{sus}_{exc} are shown in Fig. 12(a), where a more confined system shows stronger shear thickening. Values of η^{sus}_{exc} corresponding to jamming structures (marked with $*$) are much larger than those where small dynamic hydroclusters are present. Note that due to statistical errors η^{sus}_{exc} can be very small negative values at Newtonian regime. We fix such small values to be 1%, which allows for logarithmic–logarithmic scale plot.

Furthermore, we analyze the connection between cluster distribution and strength of shear thickening. We examine $p(N)$ for the same value of η^{sus}_{exc} at different L_y. In the Newtonian regime ($\eta^{sus}_{exc} \leq 1\%$), for example, we compare $p(N)$ at shear stress A under confinement $L_y = 16, 64$, and 128. $p(N)$ agrees with each other up

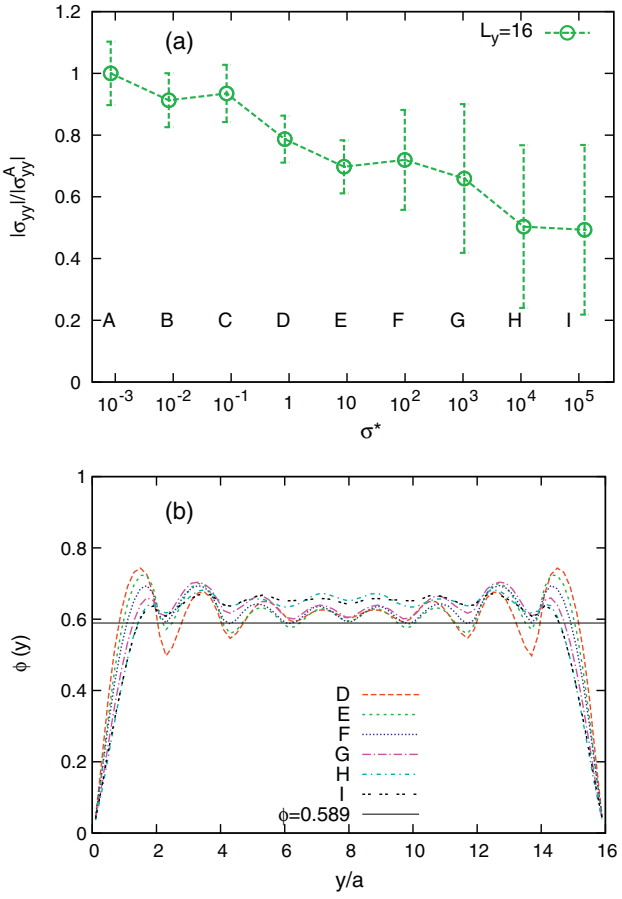

Fig. 11. Normal stress and local concentration profile for $\phi = 0.589$ and $L_y = 16$: layering effects are reduced by particle clusters formation and as a consequence, normal stress decreases with shear stress.

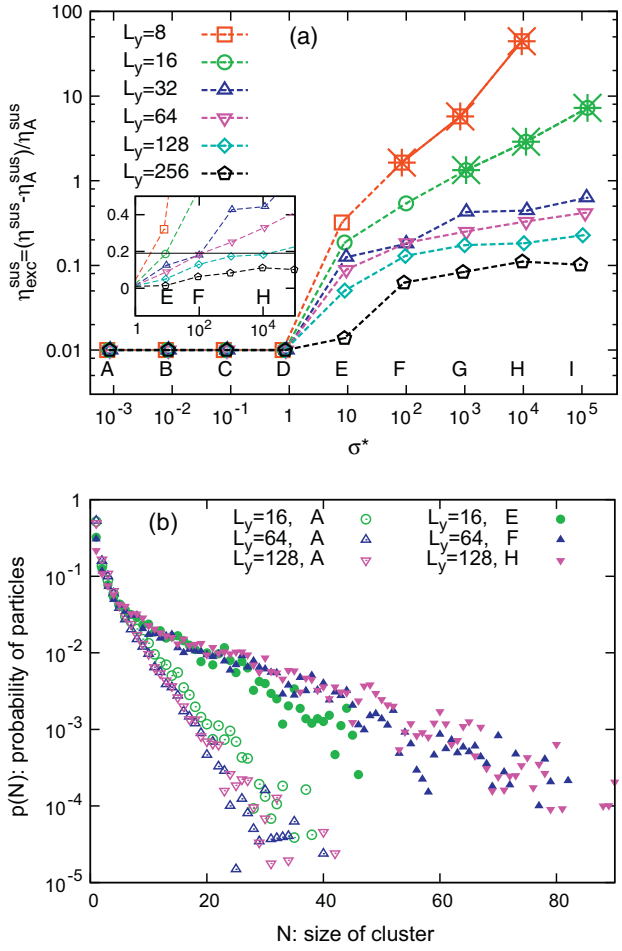

Fig. 12. Relationship between strength of shear thickening and microstructure for $\phi = 0.589$: (a) relative excess viscosity versus shear stress: η^{sus}_A is the viscosity at shear stress A. The horizontal line in the inset indicates an example of the same value of η^{sus}_{exc} at shear thickened state: E at $L_y = 16$, F at $L_y = 64$ and H at $L_y = 128$. (b) identity of $p(N)$ for the same η^{sus}_{exc}: value of η^{sus}_{exc} is uniquely determined by $p(N)$ in both Newtonian and shear thickened regimes.

to $N \approx 20$ among these confinements, as shown in Fig. 12(b). Obvious deviation takes place only when $p(N) < 10^{-3}$; in the shear thickened regime, for example, we consider a case of relative excess viscosity $\eta^{sus}_{exc} = 0.2$. $p(N)$ is found to be independent of L_y up to $N \approx 30$, as shown in Fig. 12(b). Clear discrepancies show up only when $p(N) < 5 \times 10^{-3}$.

All other available equal values of η^{sus}_{exc} confirm the similarity of $p(N)$ at both Newtonian and shear thickened regimes. This observation suggests the unique connection between cluster distribution and strength of shear thickening: regardless of the amount of confinement (L_y), whenever a certain relative excess viscosity η^{sus}_{exc} is achieved, the microstructure is the same. Note that confinement with less free space [61] provides an enhancing mechanism for cluster formation at the same $p(N)$, namely, $\sigma^*(L_y = 16) < \sigma^*(L_y = 64) < \sigma^*(L_y = 128)$.

To examine the relation of shear thickening with different confinements, we take data samples of η^{sus}_{exc} at different σ^*. As $\dot{\gamma}$ is obtained via linear fitting of velocity profile, σ^* is not perfectly aligned for different L_y at each shear stress A–I in Fig. 12(a). Therefore, for a particular value of σ^*, η^{sus}_{exc} is taken as a linear interpolation of the two nearest available data and these sampled data are always on the point-line curves in Fig. 12(a). We plot each sample of η^{sus}_{exc} versus a/L_y in Fig. 13. The value of a/L_y defines the strength of geometrical confinement in the shear gradient direction. It is clearly shown that η^{sus}_{exc} monotonically increases with a/L_y and has a stronger dependence on a/L_y at stronger confinement, but is not so sensitive to a/L_y at weaker confinement. This is illustrated by the fact that sampled data spans wider to the right side on the figure. By extrapolating values of η^{sus}_{exc} towards an infinite channel

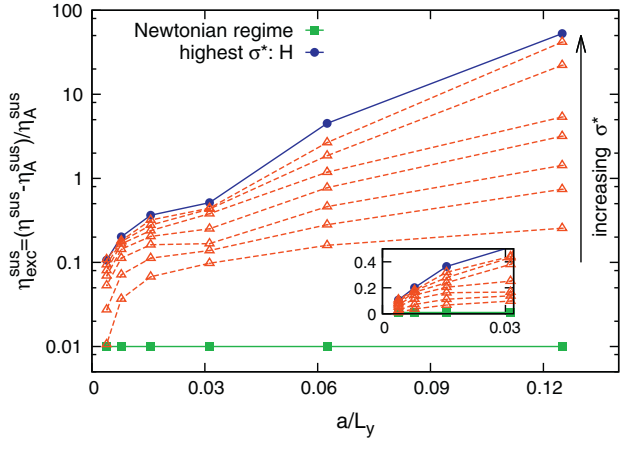

Fig. 13. Relative excess viscosity versus a/L_y: stronger shear thickening under enhanced confinement for $\phi = 0.589$. Inset: excess viscosity at weak confinement in linear–linear scale and its extrapolation to y axis suggests negligible shear thickening at bulk.

height ($L_y \to \infty$), the intercept with y axis in linear–linear scale (Inset of Fig. 13) would define the bulk behavior. Extrapolating our data, however, suggests in this limit that shear thickening is

significantly reduced below the threshold accuracy of the method ($< 3\%$). This can also explain why CST obtained via previous simulations using Lees–Edwards boundary condition is mild.

4. Conclusion

We present a suspension model based on smoothed particle hydrodynamics (SPH) method. With the Lagrangian meshfree feature of SPH, moving boundaries of rigid particles and walls are readily simulated. We apply the model to study the non-Newtonian rheology of non-Brownian repulsive particles in suspension. In particular, the suspension is confined between two parallel walls and undergoes simple shear flow. The flow is generated by constant velocities of two walls in opposite directions, which defines an input shear rate $\dot{\gamma}^{in}$. As concentrated suspensions always show velocity slip near wall regions, we measure the effective shear rates $\dot{\gamma}$ to obtain the suspension viscosity. Newtonian plateau and thickened viscosities are universally observed at all confinements studied.

Without an extra repulsive force between particles, the pairwise microstructure (RDF) of particles would remain symmetric under shear flow. It is the repulsion that breaks the symmetry of low-Reynolds number regime, as shown in Section 3.2. Thereafter, the detailed balance of shearing and repulsive forces determines the degree of anisotropy in the microstructure and the strength of the resulted shear thickening behavior. At higher shear stress, however, the configuration of particles shows structure beyond the pairwise fashion. In fact, as shown in Figs. 8 and 10, particles form networks termed as hydroclusters. Within one hydrocluster, relative motion of one pair is coupled to other pairs and as a result, the particles show collective behavior for a certain time window. It is worth emphasizing that gaps between particles within one cluster are so small that viscous force due to lubrication layers are large. This directly explains the increased viscosity at high shear stress. The correlation of hydroclusters and the onset of shear thickening is witnessed at all confinements studied. To quantify the correlations, especially at each confinement, we further examine the probability distribution of particles in the clusters against the strength of shear thickening. Our simulations show that (i) higher probability of large clusters leads to higher viscosity; (ii) strength of shear thickening (defined as the excess viscosity rather than the viscosity itself) is enhanced due to confinement, but is uniquely determined by the hydroclusters distribution (see Fig. 12); (iii) hydroclusters percolate and develop into a jamming structure under strong confinement, resulting in a significant shear thickening.

We identify that wall confinement plays a geometrical role with two consequences: (1) increasing effective packing fraction, reducing free space and facilitating cluster formation, and (2) enhancing HIs [25]. As a result of both (1) and (2), at the same shear stress stronger shear thickening takes place in a more confined system. We further observe: (iv) extrapolating viscosity data in the limit of weak confinement suggests a negligible shear thickening at bulk for the shear stress range considered here.

We note that the strong, but continuous shear thickening under confinement does not require the addition of surface friction [21], yet can arise from HIs when particles have a finite surface roughness represented by short-range repulsive forces. These results in 2*D* suspensions provide a possible explanation of non-Newtonian effects often observed in experimental suspension rheology such as microstructure without fore-aft symmetry and shear thickening.

Acknowledgments

The authors thank the DFG (German Research Foundation) for financial support via Grant EL503/1-2. X.B. acknowledges the financial support of the TUM-Graduate School's Faculty Graduate Center Mechanical Engineering for visiting the group of Prof. Wagner. Computer resources for this project have been provided by the Leibniz Supercomputing Center under the grant < pr58ye >. The authors also benefit from the comments of two anonymous reviewers and wish to express gratitude for their efforts.

References

[1] J. Mewis, N.J. Wagner, Colloidal Suspension Rheology, Cambridge University Press, Cambridge, 2012.
[2] R.G. Larson, The Structure and Rheology of Complex Fluids, Oxford University Press, New York, 1999.
[3] D.A. Fedosov, W. Pan, G. Gompper, G.E. Karniadakis, Predicting human blood viscosity in silico, Proc. Natl. Acad. Sci. USA 108 (2011) 11772–11777.
[4] J. Mewis, N.J. Wagner, Current trends in suspension rheology, J. Non-Newton. Fluid 157 (2009) 147–150.
[5] N.J. Wagner, J.F. Brady, Shear thickening in colloidal dispersions, Phys. Today 62 (10) (2009) 27–32.
[6] Y. Lee, E. Wetzel, N. Wagner, The ballistic impact characteristics of Kevlar woven fabrics impregnated with a colloidal shear thickening fluid, J. Mater. Sci. 38 (13) (2003) 2825–2833.
[7] H.A. Barnes, Shear-thickening ("dilatancy") in suspensions of nonaggregating solid particles dispersed in Newtonian liquids, J. Rheol. 33 (2) (1989) 329–366.
[8] G. Bossis, J.F. Brady, The rheology of Brownian suspension, J. Chem. Phys. 91 (3) (1989) 1866–1874.
[9] G.I. Batchelor, J.T. Green, The hydrodynamic interaction of two small freely-moving spheres in a linear flow field, J. Fluid Mech. 56 (1972) 375–400.
[10] C.D. Cwalina, N.J. Wagner, Material properties of the shear-thickened state in concentrated near hard-sphere colloidal dispersions, J. Rheol. (1978-present) 58 (4) (2014) 949–967.
[11] H.M. Laun, R. Bung, S. Hess, W. Loose, O. Hess, K. Hahn, E. Hädicke, R. Hingmann, F. Schimidt, P. Lindner, Rheological and small angle neutron scattering investigation of shear-induced particle structures of concentrated polymer dispersions submitted to plane Poiseuille and Couette flow, J. Rheol. 36 (4) (1992) 743–787.
[12] J. Bender, N.J. Wagner, Reversible shear thickening in monodisperse and bidisperse colloidal dispersions, J. Rheol. 40 (5) (1996) 899–916.
[13] B.J. Maranzano, N.J. Wagner, Flow-small angle neutron scattering measurements of colloidal dispersion microstructure evolution through the shear thickening transition, J. Chem. Phys. 117 (22) (2002) 10291–10302.
[14] J. Bender, N.J. Wagner, Optical measurement of contributions of colloidal forces to the rheology of concentrated suspensions, J. Colloid Interface Sci. 172 (1995) 171–184.
[15] X. Cheng, J.H. McCoy, J.N. Israelachvili, I. Cohen, Imaging the microscopic structure of shear thinning and thickening colloidal suspensions, Science 333 (6047) (2011) 1276–1279.
[16] J.F. Brady, G. Bossis, The rheology of concentrated suspensions of spheres in simple shear flow by numerical simulation, J. Fluid Mech. 155 (1985) 105–129.
[17] D.R. Foss, J.F. Brady, Structure, diffusion and rheology of Brownian suspensions by Stokesian dynamics simulation, J. Fluid Mech. 407 (2000) 167–2000.
[18] A. Sierou, J.F. Brady, Rheology and microstructure in concentrated noncolloidal suspensions, J. Rheol. 46 (5) (2002) 1031–1056.
[19] A.J. Banchio, J.F. Brady, Accelerated Stokesian dynamics: Brownian motion, J. Chem. Phys. 118 (22) (2003) 10323–10332.
[20] I. Zarraga, D. Hill, D. Leighton, The characterization of the total stress of concentrated suspensions of noncolloidal spheres in Newtonian fluids, J. Rheol. 44 (2) (2000) 185–220.
[21] R. Seto, R. Mari, J.F. Morris, M.M. Denn, Discontinuous shear thickening of frictional hard-sphere suspensions, Phys. Rev. Lett. 111 (2013) 218301.
[22] A. Fall, N. Huang, F. Bertrand, G. Ovarlez, D. Bonn, Shear thickening of cornstarch suspensions as a reentrant jamming transition, Phys. Rev. Lett. 100 (2008) 018301.
[23] E. Brown, H.M. Jaeger, The role of dilation and confining stresses in shear thickening of dense suspensions, J. Rheol. 56 (2012) 875–923.
[24] E. Brown, H.M. Jaeger, Through thick and thin, Science 333 (2011) 1230–1231.
[25] J.W. Swan, J.F. Brady, Hydrodynamics of confined dispersions, J. Fluid Mech. 687 (2011) 254–299.
[26] J.J. Monaghan, Smoothed particle hydrodynamics, Rep. Prog. Phys. 68 (8) (2005) 1703–1759.
[27] T. Zhao, X. Wang, L. Jiang, R.G. Larson, Assessment of mesoscopic particle-based methods in microfluidic geometries, J. Chem. Phys. 138 (2013) 084109.
[28] D. Pan, N. Phan-Thien, N. Mai-Duy, B.C. Khoo, Numerical investigations on compressibility of a DPD fluid, J. Comput. Phys. 242 (2013) 196–210.
[29] A.J.C. Ladd, R. Verberg, Lattice-Boltzmann simulations of particle–fluid suspensions, J. Stat. Phys. 104 (5–6) (2001) 1191–1251.
[30] R.C. Ball, J.R. Melrose, Lubrication breakdown in hydrodynamic simulations of concentrated colloids, Adv. Colloid Interface Sci. 59 (1995) 19–30.
[31] D.I. Dratler, W.R. Schowalter, Dynamic simulation of suspensions of non-Brownian hard spheres, J. Fluid Mech. 325 (1996) 53–77.
[32] J.F. Brady, G. Bossis, Stokesian dynamics, Ann. Rev. Fluid Mech. 20 (1988) 111–157.

[33] G.R. Liu, M.B. Liu, Smoothed Particle Hydrodynamics a Meshfree Particle Method, World Scientific Publishing Co. Pte. Ltd, Singapore, 2003.
[34] W.G. Hoover, Smoothed Particle Applied Mechanics: The State of the Art, World Scientific Publishing Co. Pte. Ltd, Singapore, 2006.
[35] S. Li, W.K. Liu, Meshfree Particle Methods, Springer Verlag, Berlin, 2007.
[36] V. Springel, Smoothed particle hydrodynamics in astrophysics, Annu. Rev. Astron. Astrophys. 48 (2010) 391–430.
[37] D.J. Price, Smoothed particle hydrodynamics and magnetohydrodynamics, J. Comput. Phys. 231 (2012) 759–794.
[38] P. Español, M. Revenga, Smoothed dissipative particle dynamics, Phys. Rev. E 67 (2) (2003) 026705.
[39] J.P. Morris, P.J. Fox, Y. Zhu, Modeling low Reynolds number incompressible flows using SPH, J. Comput. Phys. 136 (1) (1997) 214–226.
[40] X. Bian, S. Litvinov, R. Qian, M. Ellero, N.A. Adams, Multiscale modeling of particle in suspension with smoothed dissipative particle dynamics, Phys. Fluids 24 (2012) 012002.
[41] J.J. Monaghan, Simulating free surface flows with SPH, J. Comput. Phys. 110 (1994) 399–406.
[42] M. Ellero, N.A. Adams, SPH simulations of flow around a periodic array of cylinders confined in a channel, Int. J. Numer. Meth. Eng. 86 (8) (2011) 1027–1040.
[43] S. Plimpton, Fast parallel algorithms for short-range molecular dynamics, J. Comput. Phys. 117 (1) (1995) 1–19.
[44] I.F. Sbalzarini, J.H. Walther, M. Bergdorf, S.E. Hieber, E.M. Kotsalis, P. Koumoutsakos, PPM – a highly efficient parallel particle-mesh library for the simulation of continuum systems, J. Comput. Phys. 215 (2006) 566–588.
[45] W.R. Hwang, M.A. Hulsen, H.E.H. Meijer, Direct simulation of particle suspensions in sliding bi-periodic frames, J. Comput. Phys. 194 (2004) 742–772.
[46] J. Kromkamp, D. van den Ende, D. Kandhai, R. van der Sman, R. Boom, Lattice Boltzmann simulation of 2D and 3D non-Brownian suspensions in Couette flow, Chem. Eng. Sci. 61 (2006) 858–873.
[47] X. Bian, M. Ellero, A splitting integration scheme for the {SPH} simulation of concentrated particle suspensions, Comput. Phys. Commun. 185 (1) (2014) 53–62.
[48] J.R. Melrose, R.C. Ball, The pathological behavior of sheared hard spheres with hydrodynamic interactions, Europhys. Lett. 32 (6) (1995) 535–540.
[49] J.F. Brady, J.F. Morris, Microstructure of strongly sheared suspensions and its impact on rheology and diffusion, J. Fluid Mech. 348 (1997) 103–139.
[50] R.D. Groot, P.B. Warren, Dissipative particle dynamics: bridging the gap between atomistic and mesoscopic simulation, J. Chem. Phys. 107 (11) (1997) 4423–4435.
[51] G. Bossis, J.F. Brady, Dynamic simulation of sheared suspensions. I. General method, J. Chem. Phys. 80 (10) (1984) 5141–5154.
[52] N.Q. Nguyen, A.J.C. Ladd, Lubrication corrections for lattice-Boltzmann simulations of particle suspensions, Phys. Rev. E 66 (046708) (2002).
[53] P.M. Kulkarni, J.F. Morris, Suspension properties at finite Reynolds number from simulated shear flow, Phys. Fluids 20 (2008) 040602.
[54] T.N. Phung, J.F. Brady, G. Bossis, Stokesian dynamics simulation of Brownian suspensions, J. Fluid Mech. 313 (1996) 181–207.
[55] C.R. Nugent, K.V. Edmond, H.N. Patel, E.R. Weeks, Colloidal glass transition observed in confinement, Phys. Rev. Lett. 99 (2007) 025702.
[56] J.F. Brady, The Einstein viscosity correction in n dimensions, Int. J. Multiphase Flow 10 (1) (1984) 113–114.
[57] I.M. Krieger, Rheology of monodisperse latices, Adv. Colloid Interface Sci. 3 (1972) 111–136.
[58] I.M. Krieger, T.J. Dougherty, A mechanism for non-Newtonian flow in suspensions of rigid spheres, Trans. Soc. Rheol. 3 (1959) 137–152.
[59] D. Quemada, Rheology of concentrated disperse systems and minimum energy dissipation principle, Rheol. Acta 16 (1) (1977) 82–94.
[60] J.G. Berryman, Random close packing of hard spheres and disks, Phys. Rev. A 27 (1983) 1053–1061.
[61] K.W. Desmond, E.R. Weeks, Random close packing of disks and spheres in confined geometries, Phys. Rev. E 80 (2009) 051305.
[62] J.R. Melrose, R.C. Ball, Continuous shear thickening transitions in model concentrated colloids – the role of interparticle forces, J. Rheol. 48 (5) (2004) 937–960.
[63] M.K. Chow, C.F. Zukoski, Gap size and shear history dependencies in shear thickening of a suspension ordered at rest, J. Rheol. (1978-present) 39 (1) (1995) 15–32.
[64] F. Parsi, F. Gadala Maria, Fore and aft asymmetry in a concentrated suspension of solid spheres, J. Rheol. (1978-present) 31 (8) (1987) 725–732.
[65] A. Singh, P. Nott, Experimental measurements of the normal stresses in sheared Stokesian suspensions, J. Fluid Mech. 490 (2003) 293–320.
[66] F. Blanc, A. Lemaître, A. Meunier, F. Peters, Microstructure in sheared non-Brownian concentrated suspensions, J. Rheol. 57 (2013) 273–292.